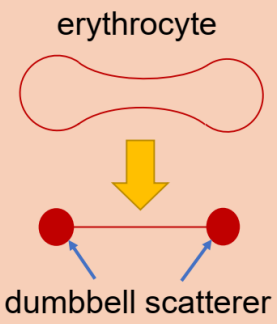
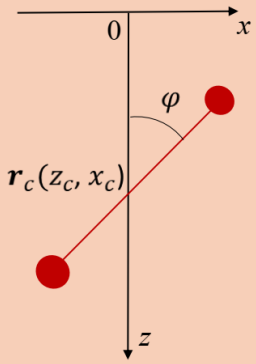
Volume 7, Issue 1, 2021

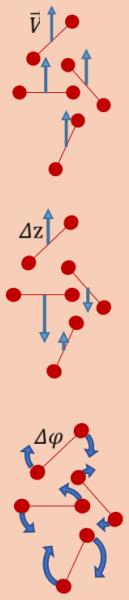
Journal of Biomedical Photonics & Engineering

Special Issue

"Laser and optical technologies in biomedicine and ecology"







Special Issue Editors:
Ivan A. Bratchenko and Aleksandra M. Mayorova

© 2021 J-BPE

 doi: 10.18287/JBPE21.07.010001

Journal of Biomedical Photonics & Engineering

by Samara National Research University

Volume 7, Issue 1 (March 2021)

Special Issue

“Laser and optical technologies in biomedicine and ecology”

Special Issue Editors

Ivan A. Bratchenko
Samara National Research University

Aleksandra M. Mayorova
Samara Branch of P.N. Lebedev Physical Institute of Russian Academy of Sciences

Editor-In-Chief

Valery V. Tuchin - Saratov National Research State University, Russian Federation;
Institute of Precision Mechanics and Control RAS, Russian Federation; a corr.-member of RAS

Deputy Editor-In-Chief

Valery P. Zakharov - Samara National Research University, Russian Federation

Postal address:
39B Lukacheva st., room #301
Samara 443086, Russian Federation

Used Figure from this issue on the Cover

Alexey A. Zykov et al. Flexible Computationally Efficient Platform for Simulating Scan Formation in Optical Coherence Tomography with Accounting for Arbitrary Motions of Scatterers, 010304, Fig. 5 (adapted).

 © 2021 J-BPE

Contents

Introduction

Foreword to the Special Issue on Laser and optical technologies in biomedicine and ecology 010101

Articles

Applying of Chitosan-TiO2 Nanocomposites for Photocatalytic Degradation of Anthracene and Pyrene 010301
Danila A. Tatarinov, Sofia R. Sokolnikova, and Natalia A. Myslitskaya

Study into Dynamics of Structural Changes Occurring in Blood Plasma under Laser Radiation 010302
Anna V. Neupokoeva, Dmitry A. Gavrilov, and Andrey S. Yakutin

Measurement of Silicon Nanoparticles Temperature by Raman Spectroscopy 010303
Alida F. Alykova, Maria S. Grigoryeva, Irina N. Zavestovskaya, and Victor Yu. Timoshenko

Flexible Computationally Efficient Platform for Simulating Scan Formation in Optical Coherence Tomography with Accounting for Arbitrary Motions of Scatterers 010304
Alexey A. Zykov, Alexander L. Matveyev, Lev A. Matveev, Alexander A. Sovetsky, and Vladimir Y. Zaitsev

Changes in the Structure of the Benzylpenicillin Sodium Salt Molecule under the Pulsed Magnetic Field 010305
Natalia A. Rodenko, Valentina A. Zhukova, Tatyana I. Vasilieva, Vladimir A. Glushchenkov, and Irina A. Belyaeva

Research into Silicon Nanoparticles as Agents for UHF Hyperthermia *In Vitro* 010306
Angelina V. Kosheleva and Egor A. Bobkov

 © 2021 J-BPE

 doi: 10.18287/JBPE21.07.010101

Foreword to the Special Issue on Laser and optical technologies in biomedicine and ecology

Dear Colleagues,

For the sixth time, it is our pleasure to present you the Special Issue of the Journal of Biomedical Photonics & Engineering (J-BPE) with selected papers of the Biophotonics Workshop of the XVIII All-Russian Youth Conference-Contest on Optics and Laser Physics (Samara, November 10-14, 2020). The conference-contest was organized by P.N. Lebedev Physical Institute (Samara Branch) and Samara National Research University and supported by Administration of Samara Region and Samara SPIE Student Chapter.

The Biophotonics Workshop 2020 was held online, and its program included competitive oral and poster reports of young scientists from technical and medical universities and academician scientific organizations of Moscow, Nizhny Novgorod, Saratov, Orel, Irkutsk, Kaliningrad, St. Petersburg, Samara and Astrakhan, invited reports and brilliant lectures by leading scientists. A wide range of questions including optical applications in medicine, biology, and ecology was discussed at the Workshop. The lectures of Academician of the RAS **Yu. N. Kulchin** (Institute of Automation and Control Processes FEB of RAS, Vladivostok), **Prof. E.A. Genina** (Saratov State University), **Prof. I. N. Zavestovskaya** (National Research Nuclear University MEPhI, Moscow) and **Prof. V. E. Pozhar** (Scientific and Technological Center of Unique Instrumentation of RAS, Moscow) aroused great interest.

The winner of the Biophotonics section in the Oral Presentations nomination became **A. Sovetsky** (Institute of Applied Physics of RAS, Nizhny Novgorod) whom paper with co-authors **A. Zykov** et al. is presented in the Special Issue of J-BPE. Their study as other papers presented in the Special Issue cover a wide range of laser and optics modalities for biomedical and ecological applications.

Alexey Zykov *et al.* (Institute of Applied Physics of RAS, Nizhny Novgorod) proposed a computationally efficient and fairly realistic model of OCT-scan formation in spectral-domain optical coherence tomography. The model is based on the approximation of discrete scatterers and ballistic character of scattering. An important feature of the model is its ability to easily account for arbitrary scatterer motions and computationally efficiently generate large sequences of OCT scans for gradually varying configurations of scatterers. This makes the proposed simulation platform very convenient for studies related to the development of angiographic processing of OCT scans for visualization of microcirculation of blood, as well as for studies of decorrelation of speckle patterns in OCT scans due to random motions of scatterers. Examples demonstrating utilization of the proposed model for generation OCT scans imitating perfused vessels in biological tissues, as well as evolution of speckles in OCT scans due to random translational and rotational motions of localized scatterers are demonstrated.

 doi: 10.18287/JBPE21.07.010101

Alida Alykova *et al.* from National Research Nuclear University MEPhI (Moscow Engineering Physics Institute) demonstrated the temperature measurements of silicon nanoparticles. The temperature was determined under laser photo-induced heating from the ratio of the intensities of the Stokes and anti-Stokes components of the Raman scattering. The obtained results of the dependence of nanoparticles temperature on the laser radiation intensity and the temperature dependence of the Raman line position may be used to determine the optimal regimes of photo-hyperthermia enhanced by silicon nanoparticles for cancer therapy.

Anastasia Kosheleva *et al.* from National Research Nuclear University "Moscow Engineering Physics Institute" shows the results of nanoparticles selectively heated by external action as agents for hyperthermia of some types of tumors. In their study the selective heating of suspensions of silicon nanoparticles using a device for electromagnetic high-frequency therapy is performed.

Anna Neupokoeva *et al.* (Irkutsk State Medical University) describes the studying the impact of laser irradiation (λ = 532 nm) on human blood plasma. The structural changes in plasma were controlled by the crystallographic method with the mean crystallogram segment size as a numerical evaluation. In addition, the structural changes were explored by processing the speckle patterns obtained during laser radiation passes through plasma. Exposure to laser radiation for 20 min resulted in the 30% reduction of the crystallogram characteristic size with the dynamics of the structural changes coinciding with the dynamics discovered by speckle patterns processing. The crystallographic method revealed that laser induced structural changes in plasma remain for 24–36 h after exposure.

Natalia Rodenko *et al.* from Samara National Research University studied the Fourier spectra of the antibiotic exposed to a high-intensity pulsed magnetic field. The action was carried out at a frequency f = 40 kHz, with a number of pulses n = 1, at intensities of the pulsed magnetic field $H = 0.09 * 10^6$ A/m, $H = 0.50 * 10^6$ A/m, $H = 0.82 * 10^6$ A/m. It was assumed that under the conditions of the pulsed magnetic field there may be a change in the structure of the drug molecule. The authors noted that an increase in the pulsed magnetic field power leads first to a decrease in the intensity of the band in the Fourier spectrum, and then – to its increase.

Danila Tatarinov *et al.* (Kaliningrad State Technical University) highlights a chitosan-TiO_2 nanocomposites (NCs CS-TiO_2) were development for the photocatalytic degradation of representatives of polycyclic aromatic hydrocarbons (PAHs). TiO_2 nanoparticles were synthesized by laser ablation method and their sizes were determined by dynamic laser light scattering. Anthracene and pyrene in micellar solution were used as representatives of PAHs. The effect of TiO_2 in the composition of prepared nanocomposites on the photodegradation of PAHs in model environments under UV irradiation was studied. The method of solid-phase luminescence was used to estimate the decrease in PAHs concentrations. The efficiency of using the nanocomposites for the photocatalytic degradation of anthracene and pyrene was demonstrated.

The papers collected in the Special Issue highlights the potential of optical and laser technologies in modern medical, biological and ecological applications.

 doi: 10.18287/JBPE21.07.010101

Special Issue Editors:

Ivan A. Bratchenko
Samara National Research University
E-mail: iabratchenko@gmail.com

Aleksandra M. Mayorova
Samara Branch of P.N. Lebedev Physical Institute of Russian Academy of Sciences
E-mail: mayorovaal@gmail.com

Applying of Chitosan-TiO_2 Nanocomposites for Photocatalytic Degradation of Anthracene and Pyrene

Danila A. Tatarinov*, Sofia R. Sokolnikova, and Natalia A. Myslitskaya
Department of Physics, Kaliningrad State Technical University, 1 Sovetsky prospect, Kaliningrad 236022, Russia

*** e-mail:** dan.tatarinov@mail.ru

Abstract. In this work, chitosan-TiO_2 nanocomposites (NCs CS-TiO_2) were developed for the photocatalytic degradation of some representatives of polycyclic aromatic hydrocarbons (PAHs). TiO_2 nanoparticles (NPs) were synthesized by laser ablation method and their sizes were determined by dynamic laser light scattering (DLLS). Anthracene and pyrene in micellar solution were used as representatives of PAHs. The effect of TiO_2 in the composition of prepared nanocomposites on the photodegradation of PAHs in model environments under UV irradiation was studied. The method of solid-phase luminescence (SPL) was used to estimate the decrease in PAHs concentrations. Based on the results of the studies carried out, pseudo-first order photodegradation kinetics were plotted. The efficiency of using the nanocomposites for the photocatalytic degradation of anthracene and pyrene was proved. © 2021 Journal of Biomedical Photonics & Engineering.

Keywords: titanium dioxide nanoparticles; TiO_2; photocatalyst; polycyclic aromatic hydrocarbons; PAH; pyrene; anthracene; chitosan; UV irradiation.

Paper #3401 received 15 Jan 2021; revised manuscript received 5 Feb 2021; accepted for publication 16 Feb 2020; published online 21 Mar 2021. doi: 10.18287/JBPE21.07.010301.

1 Introduction

PAHs are compounds containing two or more fused benzene rings in the molecule. Compounds of this group are found everywhere in the environment. PAHs are dangerous pollutants and are classified as compounds with significant risk to human health [1]. PAHs are dangerous even in small amounts due to their bioaccumulative properties. It was found that the content of PAH group substances in the environment is exceeded, the risk of developing cancer increases many times [2]. In this regard, it is actually to study the methods of degradation of PAHs, in particular with photocatalytic reactions [3].

In this work, TiO_2 was used as a photocatalyst, which has high photoactivity and demonstrates potential advantages in the oxidation of ecotoxicants, including PAHs, SO_2, NO_2, etc. [3, 4]. It is known that materials with the addition of TiO_2 can significantly improve the state of the environment. For example, in the construction industry, research is being conducted to develop an innovative building material containing the TiO_2 photocatalyst. Photocatalysis technologies make possible the production of construction materials with advanced functions such as self-cleaning, air purifying and surface self-sterilization [5]. For example, concrete pavements with TiO_2 to decompose airborne pollutants and antibacterial ceramic tiles were developed [6]. Moreover, the application of photocatalytic materials for barrier structures, road surfaces and tunnels can be useful in reducing the level of environmental pollution [7].

TiO_2 is also used in the field of water treatment. When TiO_2 is used to purify aqueous media, hydroxyl radicals are generated during photocatalysis, which act as an oxidizing agent. In this regard, toxic contaminants contained in the purified water decompose to inorganic components without the formation of secondary waste [8].

This article focuses on the possibility of developing and applying biopolymer nanocomposites using TiO_2 for the photocatalytic degradation of PAHs in aqueous media. Pyrene (PYRE) and anthracene (ANTR) were chosen as representative compounds of PAHs. The process of photodegradation was studied under various experimental parameters.

2 Backgrounds

In the nature, TiO_2 has three different types of crystal structure: anatase, rutile and brookite. It is known that

TiO_2 NPs in the anatase phase with a band gap of 3.2 eV exhibit good photocatalytic activity. In case of absorption of a photon with an energy equal to or exceeding the band gap in TiO_2, an electron transition from the valence band to the conduction band can occur. After this, the formation of electron-hole pairs occurs due to the formed free vacancies in the valence band. The created electron-hole pair has a sufficient lifetime in the nanosecond range to transfer charge to adsorbed particles on the semiconductor surface [9]. Then, excited electrons in the conduction band and holes in the valence band recombine, followed by dissipation of energy in the form of heat. If suitable absorbers are available for trapping an electron or a hole, redox reactions can occur [10]. The scheme of the described photocatalytic processes is shown in Fig. 1.

Photodegradation of PAHs in aqueous media with the addition of TiO_2 has been actively studied recently. The authors of Ref. [11] have noted that TiO_2 can effectively photocatalyze the oxidation of PAHs, such as anthracene, fluorene, and naphthalene, when irradiated with artificial light or sunlight. In Ref. [12], the photocatalytic degradation of a mixture of 16 PAHs in aqueous TiO_2 suspensions with a large surface area illuminated by UV light was studied. The authors of Ref. [13] have proved that the reaction of photocatalysis for pyrene with the addition of TiO_2 occurs with the producing of some intermediate products (4-oxapyrene-5-one, 1,6- or 1,8-pyrenediones, 4,5-phenanthrenedialdehyde, cyclopenta[def]phenanthrene). As a result, pyrene can finally be mineralized to CO_2, which is not a potential pollutant for the environment.

To increase the efficiency rate of TiO_2, the authors of Ref. [14] proposed the photocatalytic degradation of naphthalene in water using TiO_2 on Raschig glass rings. In the study [15], the photocatalytic degradation of aqueous solutions of naphthalene and anthracene in a thin layer of TiO_2 particles on glass substrates was studied. The authors of Ref. [16] have observed that the use of TiO_2 in high concentrations for the photocatalytic degradation of PAHs becomes ineffective and the rate of photodegradation decreases with increasing TiO_2 concentration. This decrease could be connected with the fact that the titanium particles caused the diffusion of UV light and that reduces the absorption of light in the reaction media. In this regard, it can be efficient to use low TiO_2 concentrations for the photocatalytic degradation of PAHs.

In recent years, research into the practical use of polymers for the treatment of aqueous media has become actual. On their basis, ecological materials with various properties have been created, such as sorbents, films and filters, membranes for nano- and ultrafiltration, and functional composite materials [17]. Some biopolymer materials with nanodispersed TiO_2 are used to improve the functional properties of nanocomposites and increase the photocatalytic activity of TiO_2. One of the prospective biopolymers for solving such tasks is chitosan (CS) the product of chitin deacetylation [18].

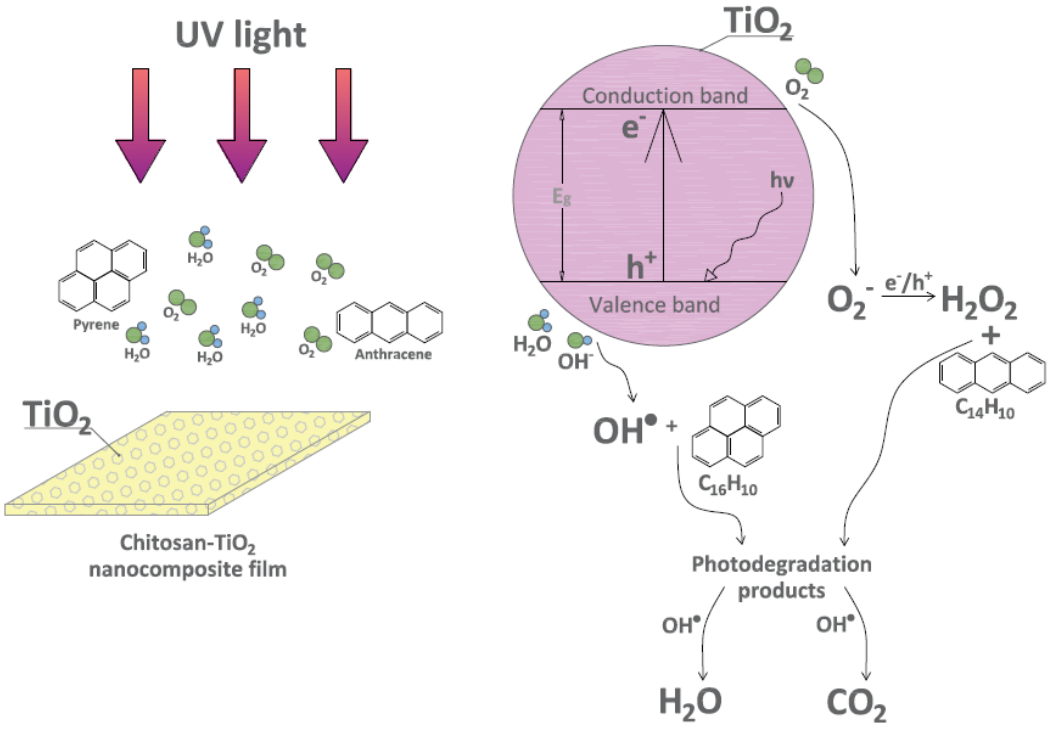


Fig. 1 Scheme of PAHs photodegradation on nanocomposites chitosan-TiO_2.

CS matrices show a high sorption capacity [19–20] and are effective sorbents of such compounds as heavy metal ions, dyes, PAHs, etc. CS has a high ability to chemical modification due to the presence of reactive amino and hydroxyl groups. This allows one to select the different characteristics of polymeric sorbent according to the tasks [21].

3 Materials and methods

In this work, the processes of degradation of ecotoxicants of the PAH group were studied in aqueous media. Nanocomposites with the addition of TiO_2 based on CS matrices have been developed. In Ref. [22], the authors modified the CS matrices to improve the mechanical and sorption properties. The high sorption capacity of the produced matrices was proved, which is of interest for studying the processes of photocatalytic degradation of some PAHs.

In the study, CS (Diaham LLC, degree of deacetylation 95%, M = 1526.45 g/mol) was used as a basis for solid matrices. Also, the composition of the matrices includes polyvinyl alcohol and cetyltrimethylammonium bromide. The matrices were prepared as described in Ref. [22]. However, during the formation of the matrices, TiO_2 nanoparticles (TiO_2 NPs) with mass fraction ω_{TiO2} = 0.15, 0.5, and 1 wt. % of CS were added.

TiO_2 NPs were synthesized by laser ablation using a methodology similar to Refs. [23, 24]. A schematic of the installation for producing TiO_2 NPs is shown in Fig. 2. For preparing a colloidal solution of TiO_2 NPs, a pulsed YAG: Nd^{3+} laser was used (radiation wavelength λ = 532 nm, pulse duration τ = 11 ns, and pulse repetition rate ν = 10 Hz). A sample of thin plate Ti (99.9% pure) was immersed in distilled water and irradiated with a laser for t = 60 min. The output laser energy was 170 mJ. During irradiation, the cuvette was constantly moved to avoid crater formation in the titanium plate as a result of ablation.

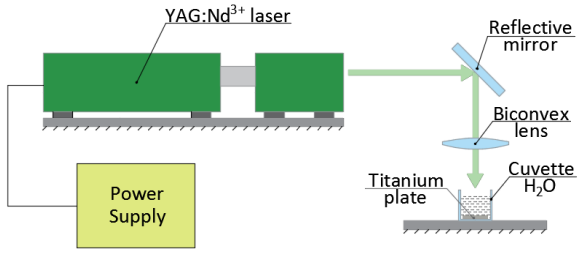


Fig. 2 Schematic of the installation for producing TiO_2 nanoparticles.

The obtained TiO_2 NPs were studied by dynamic laser light scattering (DLLS) (Fig. 3). The irradiation source was a helium-neon laser (W = 25 mW; λ = 632.8 nm; ray cross-sectional diameter 100 μm). The prepared samples were placed in a thermostat (t = 25 ± 0.1°C). The laser irradiation was scattered by TiO_2 NPs participating in the Brownian motion. The scattered light was recorded by a photomultiplier tube with a photon counting system. The correlation function of the scattered light intensity was calculated using a 32-bit 282-channel Photocor-FC correlator connected to a computer. The hydrodynamic radius of TiO_2 NPs was calculated from the results of measuring the particle sizes using DLLS and processing the results with the DynaLS program. At the critical level of significance p = 0.05, the average size of TiO_2 NPs was R = 270 ± 46 nm.

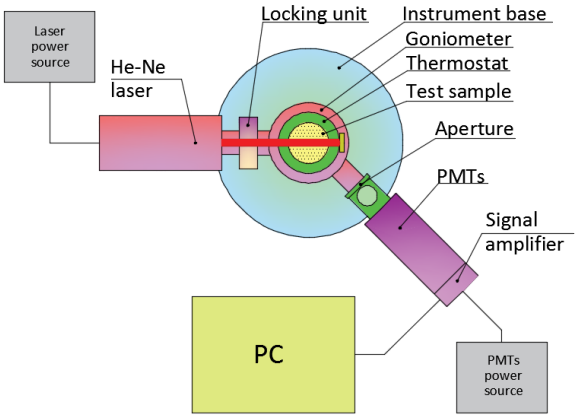


Fig. 3 Schematic of the installation for determining the size of TiO_2 nanoparticles by DLLS.

In the study, PYRE and ANTR (Fluka, Germany) were used as model PAHs. PYRE has a characteristic fluorescence spectrum, which is represented by five well-resolved main vibronic bands [25]. ANTR has a fluorescence spectrum similar to pyrene, but represented by four vibronic bands [26]. These representatives of PAHs are not highly toxic, which makes their use in laboratory studies relatively safe [25].

For solubilization of PYRE and ANTR an aqueous solution (distilled H_2O, pH = 7) of sodium dioctyl sulfosuccinate was used at a concentration of 10^{-2} M. The concentration of selected PAHs representatives in the prepared solutions was 10^{-6} M. The pH values were controlled on a pH meter (F20-Standard, Mettler Toledo, USA).

In the experiment, NCs CS-TiO_2 and control matrices from CS without TiO_2 NPs were manufactured. Samples with a size of 2 × 2 cm were prepared from the films. Shimadzu UV-3600 Plus spectrophotometer and Shimadzu UV probe data processing program were used for the recording and calculation of UV-visible absorption spectra of NCs CS-TiO_2 and control samples.

After that, static sorption of the samples was done in PAH solutions for 60 minutes under UV irradiation (UV lamp, power P = 26 W, wavelength range λ = 365–395 nm).

The solid-phase luminescence (SPL) method was used to evaluate the kinetics of PYRE and ANTR degradation on NCs CS-TiO_2. In this case, PAHs are determined on a solid matrix in the sorbent phase, providing sufficient detection sensitivity [22].

HORIBA Fluorolog-3 TCSPC modular system was used for luminescence analysis. Error of measured parameters consists of luminescence intensity measurement and emission monochromator errors. The error of monochromator emission ±0.5 nm was stated by the HORIBA manufacturer [27].

Statistical processing of the experimental results was made according to the IUPAC method [28]. For a sample with size of n = 7, the standard deviation was calculated. Then the confidence interval was determined at the mean with a critical level of significance p = 0.05 and the standard error. Thus, for the values of photodegradation efficiency, the absolute error was 0.02–0.04.

4 Results and discussion

The results of UV-visible spectrophotometry of the CS-TiO_2 samples are shown in Fig. 4. The obtained samples were studied: colloidal solution of TiO_2 NPs, control samples of solid matrices of CS and NCs CS-TiO_2.

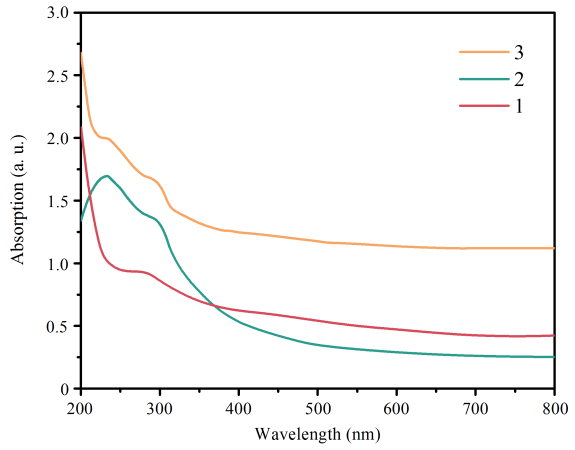


Fig. 4 Absorption spectra: 1 – solid chitosan matrix; 2 – TiO_2 nanoparticles; 3 – nanocomposites chitosan-TiO_2.

The absorption spectrum TiO_2 NPs (Fig. 4, Curve 2) consists of two bands: one about 230 nm, the second about 300 nm. According to the literature data [29], the absorption bands at these wavelengths are characteristic of the anatase phase of TiO_2. The presented spectrum confirms the presence of the anatase phase and indicates a high degree of photocatalytic activity of prepared TiO_2 NPs.

In Fig. 4, Curve 1 shows the absorption spectrum of the control matrix of CS. It is known that in the wavelength range of 250–300 nm, absorption maxima are characteristic of chitosan molecules. This is explained by the presence of a chromophore carbonyl group C=O formed during the deacetylation of chitin [30]. In Fig. 4, Curve 3 shows the absorption spectrum of the NCs CS-TiO_2. In this case, the absorption band at a wavelength of 230 nm appears, which is characteristic of TiO_2 NPs. This confirms the presence of TiO_2 NPs in the prepared nanocomposites.

A luminescent analysis of the manufactured samples was performed to study the processes of photocatalytic degradation of ANTR and PYRE using NCs CS-TiO_2. The fluorescence spectra of ANTR (λ_{ex} = 340 nm) and PYRE (λ_{ex} = 320 nm) on NCs CS-TiO_2 and control samples of CS after UV irradiation (t = 60 min) are shown in Figs. 5 and 6.

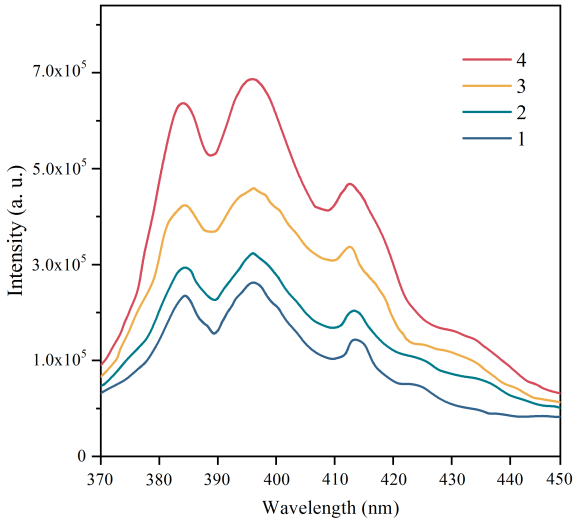


Fig. 5 The fluorescence spectra of anthracene on nanocomposites chitosan-TiO_2: 1 – ω_{TiO2}=1 wt. %; 2 – ω_{TiO2} = 0.5 wt. %; 3 – ω_{TiO2} = 0.15 wt. %; 4 – anthracene on control chitosan matrix.

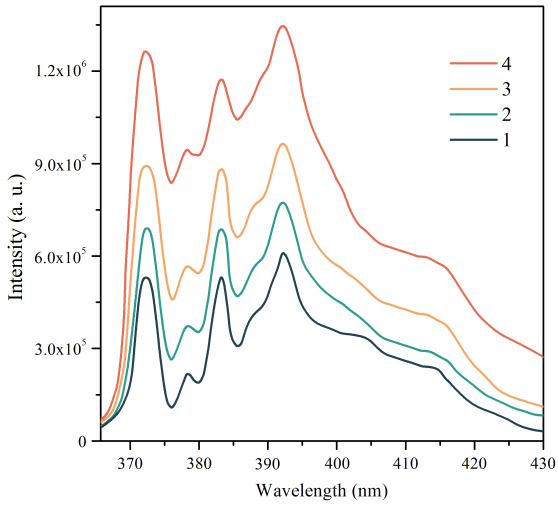


Fig. 6 The fluorescence spectra of pyrene on nanocomposites chitosan-TiO_2: 1 – ω_{TiO2} = 1 wt. %; 2 – ω_{TiO2} = 0.5 wt. %; 3 – ω_{TiO2} = 0.15 wt. %; 4 – pyrene on control chitosan matrix.

According to the results of luminescence analysis, it can be concluded that the intensity of fluorescence after static sorption on NCs CS-TiO_2 under UV irradiation is less than the intensity of PAHs after static sorption on control matrices under UV irradiation. The obtained results can be explained by the fact that the TiO_2 NPs in the composition of the manufactured nanocomposites

photocatalyze the oxidation of PAHs. The graphs also show that the efficiency of using NCs CS-TiO_2 for photodegradation of ANTR and PYRE depends on the amount of TiO_2. The highest degree of PAHs photodegradation is observed in samples with TiO_2 content $\omega_{TiO2} = 1$ wt. % at t = 60 min under UV irradiation.

PAH concentrations for the study of the degradation of ANTR and PYRE during photocatalytic reactions on NCs CS-TiO_2 ($\omega_{TiO2} = 1\%$ wt.) were determined by luminescence analysis. For example, in the study [31], the PYRE concentration on solid matrices was determined using a calibration graph. The authors found that the dependence of the SPL intensity on the PAHs concentration on the solid matrix is linear up to $C_{PAHs} = 2 \times 10^{-8}$ g/l. Similarly, the study [32] describes a technique for evaluating the concentration of ANTR using luminescence analysis. In this paper, the concentrations of ANTR and PYRE were determined using similar methods to study the photodegradation kinetics on NCs CS-TiO_2.

The photodegradation graphs of ANTR and PYRE are shown in Fig. 7. This shows the ratio of C_t/C_0 concentrations on the time t. In this case, C_t is the concentration of PAHs due to UV irradiation t. Similarly, C_0 is the initial concentration of PAHs before UV irradiation ($t_0 = 0$ min). Graphs are presented for NCs CS-TiO_2 (Fig. 7, Curves 2, 4) and respective solutions after static sorption onto NCs CS-TiO_2 (Fig. 7, Curves 1, 3). The graphs show that the efficiency of photodegradation of ANTR and PYRE on NCs CS-TiO_2 reaches 70 and 56%, respectively, after t = 60 min under UV irradiation.

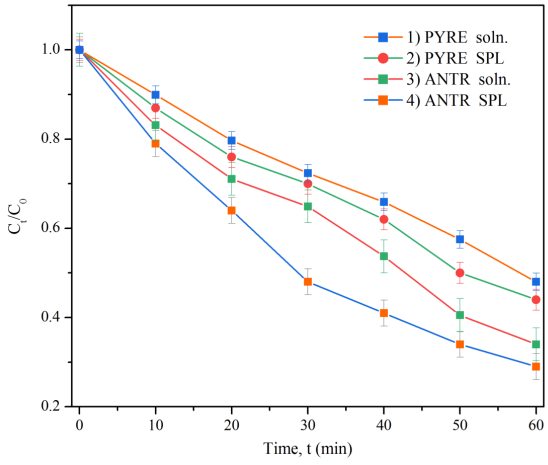


Fig. 7 Photodegradation graphs: 1 – pyrene solution; 2 – pyrene on nanocomposites chitosan-TiO2; 3 – anthracene solution; 4 – anthracene on nanocomposites chitosan-TiO_2.

Based on the literature data [33–34], the pseudo-first-order kinetics for the photocatalytic degradation of PAHs is described by Eq. (1):

$$-\frac{dC}{dt} = kC. \quad (1)$$

Then the degradation rate constant k and the half-life $t_{1/2}$ during PAH degradation were calculated using the following equations:

$$ln\frac{C_t}{C_0} = -kt; \quad (2)$$

$$t_{1/2} = \frac{ln(2)}{k}. \quad (3)$$

According to Eq. (2), pseudo-first-order kinetics graphs were plotted for the degradation of ANTR and PYRE under UV irradiation (Fig. 8). This shows the dependence of $ln(C_t/C_0)$ on the time of UV irradiation t. The kinetic parameters of the photocatalytic degradation of ANTR and PYRE were calculated. The calculation results are presented in Table 1.

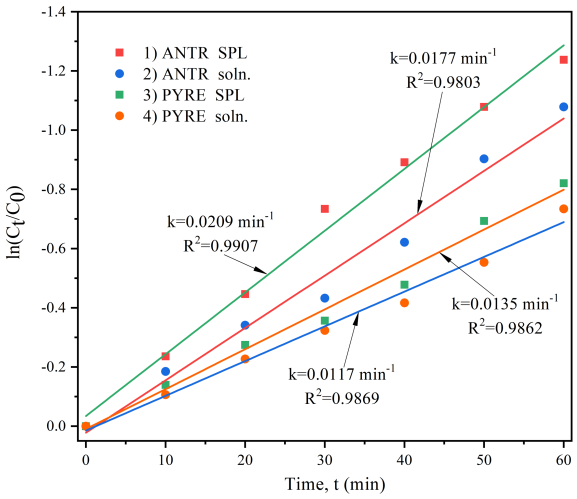


Fig. 8 Graphs of pseudo-first-order kinetics for PAHs degradation under UV irradiation: 1 – anthracene on nanocomposites chitosan-TiO_2; 2 – anthracene solution; 3 – pyrene on nanocomposites chitosan-TiO_2; 4 – pyrene solution.

Table 1 Kinetic parameters of photocatalytic degradation of ANTR and PYRE under UV irradiation.

PAHs	Sample type	k (min^{-1})	$t_{1/2}$ (min)	R^2
PYRE	Nanocomposite	0.0209	33.165	0.9907
	Solution	0.0177	39.161	0.9803
ANTR	Nanocomposite	0.0135	51.344	0.9862
	Solution	0.0117	59.243	0.9869

The experimentally obtained values of the coefficient of determination R^2 for photodegradation of ANTR and

PYRE on NCs CS-TiO_2 are 0.9907 and 0.9862 respectively. This proved that the photocatalytic degradation of ANTR and PYRE with a sufficient degree of accuracy ($R^2 > 0.95$) corresponded to pseudo-first-order kinetics.

In general, the results of kinetic studies confirm that NCs CS-TiO_2 are effective for degradation of ANTR and PYRE. For example, in Ref. [34], the photodegradation efficiency of PYRE ($C_{PYRE} = 0.5 \times 10^{-6}$ M) in a solution of TiO_2 NPs made according to the method [35] is 35% after 60 min under UV irradiation. Also, the authors of Ref. [36] obtained a value of the photodegradation efficiency of PYRE ($C_{PYRE} = 0.5 \times 10^{-6}$ M) of 46% in a solution of pure TiO_2 NPs with similar experimental conditions (power of UV lamp P = 150 W). Photodegradation of ANTR was investigated [37] under different conditions of the experiment with an initial concentration $C_{ANTR} = 1 \times 10^{-6}$ M. The authors obtained the values of the photodegradation efficiency ANTR 60% after 60 min under UV irradiation.

As a result, in this work, it was possible to achieve better photodegradation of ANTR and PYRE due to application of the developed NCs CS-TiO_2. This can be explained by the fact that modified CS solid matrices were used as the basis for them [22]. Previously, the authors proved their high sorption capacity, which is confirmed by the obtained value of the polarity index of the microenvironment of PYRE molecules. The polarity index is expressed as the ratio of the intensities of the first and third maxima of the fluorescence spectrum $I_1/I_3 = 1.08$. Also, a study [38] confirm the high adsorption capacity of TiO_2, in this case the PYRE polarity index was $I_1/I_3 = 0.98$. This is explained by the fact that PAHs molecules are actively adsorbed on the hydrophobic surface of TiO_2 during the whole photocatalytic reaction process due to their low solubility in water.

5 Conclusion

A series of experiments demonstrates the efficiency of the degradation of ANTR and PYRE in aqueous media. This is connected to the photocatalytic properties of TiO_2 under UV irradiation in the composition of modified CS matrices. In 60 min, 70% of ANTR and 56% of PYRE were photodegraded under UV irradiation on NCs CS-TiO_2. Such an effect is achieved due to the high adsorption capacity of the developed NCs CS-TiO_2.

Also, based on the results of the experiment, graphs of the pseudo-first order photodegradation kinetics were plotted. In the case of NCs CS-TiO_2, the degradation rate constants $k = 0.0209$ min^{-1} for ANTR and $k = 0.0135$ min^{-1} for PYRE were calculated. The half-life values were $t_{1/2} = 33.165$ min for ANTR and $t_{1/2} = 51.344$ min for PYRE.

The developed NCs CS-TiO_2 are prospective photocatalytic materials for the degradation of PAHs in aqueous media. They can be used for photodegradation of other dangerous PAHs, for example, benz(a)anthracene, benzo(k)fluoranthene, benz(a)pyrene, dibenzanthracene, etc. The method of manufacturing the developed nanocomposites does not require expensive equipment, and they are also convenient to use for photocatalytic reactions. After use, thin-film nanocomposites can be easily recycled without severe environmental pollution.

Disclosures

All authors declare that there is no conflict of interests in this paper.

References

1. D. F. Kalf, T. Crommentuijn, and E. J. Plassche, "Environmental quality objectives for 10 polycyclic aromatic hydrocarbons (PAHs)," Ecotoxicology and Environmental Safety 36(1), 89–97 (1997).
2. K. H. Kim, S. A. Jahan, E. Kabir, and R. J. Brown, "A review of airborne polycyclic aromatic hydrocarbons (PAHs) and their human health effects," Environment International 60, 71–80 (2013).
3. L. Zhang, P. Li, Z. Gong, and X. Li, "Photocatalytic degradation of polycyclic aromatic hydrocarbons on soil surfaces using TiO2 under UV light," Journal of Hazardous Materials 158(2–3), 478–484 (2008).
4. S. N. Habisreutinger, L. Schmidt-Mende, and J. K. Stolarczyk, "Photocatalytic reduction of CO2 on TiO2 and other semiconductors," Angewandte Chemie International Edition 52(29), 7372–7408 (2013).
5. W. Zhu, P. J. M. Bartos, and A. Porro, "Application of nanotechnology in construction," Materials and Structures 37(9), 649–658 (2004).
6. T. Watanabe, "Fabrication of TiO2 photocatalytic tile and practical applications," Fourth Euro Ceramics 11, 175–180 (1995).
7. A. H. Hamdany, "Photocatalytic cementitious material for self-cleaning and anti-microbial application," Doctoral thesis, Nanyang Technological University, Singapore (2019).
8. V. Ya. Kofman, "New oxidative technologies of water and wastewater treatment (part 1)," Water Supply and Sanitary Engineering 10, 68–78 (2013).
9. A. L. Linsebigler, G. Lu, and J. T. Yates, "Photocatalysis on TiO2 Surfaces: Principles, Mechanisms, and Selected Results," Chemical Reviews 95(3), 735–758 (1995).
10. M. R. Hoffmann, S. T. Martin, W. Choi, and D. W. Bahnemann, "Environmental Applications of Semiconductor Photocatalysis," Chemical Reviews 95(1), 69–96 (1995).

11. S. Dass, M. Muneer, and K. Gopidas, "Photocatalytic degradation of wastewater pollutants. Titanium-dioxide-mediated oxidation of polynuclear aromatic hydrocarbons," Journal of Photochemistry and Photobiology A: Chemistry 77(1), 83–88 (1994).
12. J. C. Ireland, B. Dávila, H. Moreno, S. K. Fink, and S. Tassos, "Heterogeneous photocatalytic degradation of polyaromatic hydrocarbons over titanium dioxide," Chemosphere 30(5), 965–984 (1995).
13. S. Wen, J. Zhao, G. Sheng, and J. Fu, "Photocatalytic reactions of pyrene at TiO2/water interfaces," Chemosphere 50(1), 111–119 (2003).
14. M. J. Garcia-Martinez, L. Canoira, G. Blázquez, I. Da Riva, R. Alcántara, and J. F. Llamas, "Continuous photodegradation of naphthalene in water catalyzed by TiO2 supported on glass Raschig rings," Chemical Engineering Journal 110(1–3), 123–128 (2005).
15. B. Pal, M. Sharon, "Photodegradation of polyaromatic hydrocarbons over thin film of TiO2 nanoparticles; a study of intermediate photoproducts," Journal of Molecular Catalysis A: Chemical 160(2), 453–460 (2000).
16. N. K. Salihoglu, G. Karaca, G. Salihoglu, and Y. Tasdemir, "Removal of polycyclic aromatic hydrocarbons from municipal sludge using UV light," Desalination and Water Treatment 44(1–3), 324–333 (2012).
17. A. V. Tkachenko, O. A. Djachuk, "The luminescence of polycyclic aromatic hydrocarbons on modified by surface-active agent cellulose," Proceedings of SPIE 6791, 67910P (2008).
18. U. Siripatrawan, P. Kaewklin, "Fabrication and characterization of chitosan-titanium dioxide nanocomposite film as ethylene scavenging and antimicrobial active food packaging," Food Hydrocolloids 84, 125–134 (2018).
19. M. Rinaudo, "Chitin and chitosan: properties and applications," Progress in Polymer Science 31(7), 603–632 (2006).
20. M. Jabli, M. H. V. Baouab, M. S. Roudesli, and A. Bartegi, "Adsorption of acid dyes from aqueous solution on a chitosan-cotton composite material prepared by a new pad-dry process," Journal of Engineered Fibers and Fabrics 6(3), 1–12 (2011).
21. C. Gerente, V. K. C. Lee, P. L. Cloirec, and G. McKay, "Application of chitosan for the removal of metals from wastewaters by adsorption—mechanisms and models," Critical Reviews in Environmental Science and Technology 37, 41–127 (2007).
22. D. Tatarinov, S. Sokolnikova, and N. Myslitskaya, "Solid-phase luminescence of pyrene in chitosan adsorbents," Journal of Biomedical Photonics & Engineering 6(1), 010305 (2020).
23. S. C. Singh, R. K. Swarnkar, and R. Gopal, "Synthesis of Titanium Dioxide Nanomaterial by Pulsed Laser Ablation in Water," Journal of Nanoscience and Nanotechnology 9(9), 5367–5371 (2009).
24. A. M. Ivanov, N. A. Myslickaya, and M. S. Kapelevich, "Nanoparticles producing by means of laser ablation and optic methods of their features study," KSTU News 23, 18–24 (2011) [in Russian].
25. K. H. Kim, S. A. Jahan, E. Kabir, and R. J. Brown, "A review of airborne polycyclic aromatic hydrocarbons (PAHs) and their human health effects," Environment International 60, 71–80 (2013).
26. K. Datta, A. K. Mukherjee, "Study of quenching of anthracene fluorescence by [60]fullerene," Spectrochimica Acta Part A: Molecular and Biomolecular Spectroscopy 65(2), 261–264 (2006).
27. Fluorolog-3 Operation Manual rev. G, HORIBA Instruments Incorporated, USA (2014).
28. L. A. Currie, G. Svehla, "Nomenclature for the presentation of results of chemical analysis," Pure and applied chemistry 66(3), 595–608 (1994).
29. K. Karthikeyan, A. Nithya, and K. Jothivenkatachalam, "Photocatalytic and antimicrobial activities of chitosan-TiO2 nanocomposite," International Journal of Biological Macromolecules 104, 1762–1773 (2017).
30. K. V. Reut, N. V. Dolgopyatova, V. Yu. Novikov, N. M. Putintsev, I. N. Konovalova, and Yu. A. Kuchina, "Optical activity and spectrophotometric characteristics of chitosan solutions obtained from the Kamchatka crab and the Arctic shrimp," Vestnik of MSTU 16 (3), 580–585 (2013) [in Russian].
31. S. M. Rogacheva, E. V. Volkova, M. I. Otradnova, T. I. Gubina, and A. B. Shipovskaya, "Solvent Effect on the Solid-Surface Fluorescence of Pyrene on Cellulose Diacetate Matrices," International Journal of Optics 2018, 1–6 (2018).
32. G. L. Green, T. C. O'haver, "Derivative luminescence spectrometry," Analytical Chemistry 46(14), 2191–2196 (1974).
33. Z. H. Luo, C. L. Wei, N. N. He, Z. G. Sun, H. X. Li, and D. Chen, "Correlation between the Photocatalytic Degradability of PAHs over Pt/TiO2-SiO2 in Water and Their Quantitative Molecular Structure," Journal of Nanomaterials 2015, 1–11 (2015).
34. H. Soni, N. Kumar, K. Patel, and R. N. Kumar, "Investigation on the Heterogeneous Photocatalytic Remediation of Pyrene and Phenanthrene in Solutions Using Nanometer TiO2 under UV Irradiation," Polycyclic Aromatic Compounds 40(2), 257–267 (2017).
35. H. Soni, J. N. Kumar, K. Patel, and R. N. Kumar, "Photocatalytic Decoloration of Three Commercial Dyes in Aqueous Phaseand Industrial Effluents Using TiO2 Nanoparticles," Desalination and Water Treatment 57, 6355–6364 (2016).
36. M. K. Saloot, S. M. Borghei, and R. H. S. M. Shirazi, "Evaluation of the photo-catalytic degradation of pyrene using Fe-doped TiO2 in presence of UV," Desalination And Water Treatment 169, 232–240 (2019).
37. F. F. Karam, F. H. Hussein, S. J. Baqir, A. F. Halbus, R. Dillert, and D. Bahnemann, "Photocatalytic Degradation of Anthracene in Closed System Reactor," International Journal of Photoenergy 2014, 1–6 (2014).

38. X. Jin, Y. Kusumoto, "Spectroscopic studies of pyrene adsorbed to titanium dioxide," Chemical Physics Letters 378(1–2), 192–194 (2003).

Study into Dynamics of Structural Changes Occurring in Blood Plasma under Laser Radiation

Anna V. Neupokoeva*, Dmitry A. Gavrilov, and Andrey S. Yakutin
Department of Medical and Biological Physics, Irkutsk State Medical University, 1 Krasnogo Vosstaniya str., Irkutsk 664009, Russian Federation

*** e-mail:** annett_2005@inbox.ru

Abstract. This paper focuses on studying the impact of laser irradiation (λ = 532 nm, power 15 mW) on human blood plasma. The structural changes in plasma were controlled by the crystallographic method with the mean crystallogram segment size as a numerical evaluation. In addition, the structural changes were explored by processing the speckle patterns obtained during laser radiation passes through plasma. Exposure to laser radiation of λ = 532 nm for 20 min resulted in the 30% reduced the crystallogram characteristic size with the dynamics of the structural changes coinciding with the dynamics discovered by speckle patterns processing. The crystallographic method revealed that laser induced structural changes in plasma remain for 24–36 h after exposure. © 2021 Journal of Biomedical Photonics & Engineering.

Keywords: laser biostimulation; blood plasma; crystallogram; wavelet analysis; correlation image processing; speckle pattern.

Paper #3404 received 20 Jan 2021; revised manuscript received 3 Mar 2021; accepted for publication 20 Mar 2021; published online 30 Mar 2021. doi: 10.18287/JBPE21.07.010302.

1 Introduction

Laser irradiation is widely used in medical practice. Depending on the radiation properties, e. g. wavelength, intensity, it can have both adverse (tissue destruction, burns) and beneficial effects on the body (reparative process stimulation, reduced tissue swelling and inflammation, improved tissue metabolism) [1].

However, little research has been conducted on the mechanism of laser impact both locally and systemically. Recently there have been a number of studies suggesting that laser radiation interacts with blood proteins changing their structure and functional activity [2, 3, 4]. According to this hypothesis, laser radiation is able to interact with the proteins within blood cell elements (erythrocytes, leukocytes, etc.) as well as plasma proteins. However, the effect of laser radiation on the cell-free biological media has not been adequately researched. Its possible effect on the human blood plasma structure can be beneficial and find practical use in transfusion therapy.

Nevertheless, the question of the stability level of structure changes remains open. It means that after some time the proteins partially restore the supramolecular structures when the relaxation process takes place. Studying the temporal characteristics of this process would make it possible to improve the frequency of laser procedures when treating patients.

On the other hand, the advent of new methods of examining structural changes in fluids [5, 6] has opened opportunities for a more detail research into the changes occurring during laser radiation in fluids. For this reason, the aim of this paper is to study the dynamics of structural changes occurring in blood plasma undergoing laser radiation as well as investigation of the stability margin of these changes over time.

2 Experimental study

2.1 Materials and methods

Human plasma was provided by *Irkutsk Region Blood Transfusion Station* (this organization holds the license of the Ministry of Healthcare of the Russian Federation for banking, storage and managing blood and its components as well as for operations in transfusiology). Human blood plasma was provided frozen. Before the experiments, plasma was allowed to thaw at room temperature. The source of laser radiation was a *303 LXi* diode-pumped solid-state laser (made in China) with a 532 nm wavelength. The source power was reduced by

means of a neutral light filter to 15 mW with the intensity of 50 mW/cm^2. The threshold intensity for intravenous blood laser radiation is 1–1.5 mW/cm^2, whereas the maximum intensity for biostimulation is about 100 mW/cm^2. The latter correlates with the sunlight intensity on a clear day [4]. Therefore, the mean intensity was chosen for the experiment. We also took into account the fact that plasma absorption is lower than that of whole blood. The choice of the wavelength for laser irradiation was determined by the following: most methodologies of laser irradiation make use of the red and infrared range. Even though the last ten years have seen the advent of specialized medical devices using the 532 nm wavelength [7] that is well absorbed by haemoglobin, the effect of the laser radiation within the green range remains underinvestigated [4].

Interaction of laser radiation with protein macromolecules can involve several processes: destabilization of the macromolecule hydration shell, change in the secondary and tertiary protein structure, change in the mobility of macromolecule subunits and their density, as well as dissolution of multi-molecule clusters into smaller formations. Most of these processes should result in the change of the inhomogeneity characteristic size in a solution.

When the solution dries up, the first to fasten on the substrate are large macromolecule clusters (having a lower random velocity as a unit) that also act as nuclei (or crystallization centres) for crystal growing in the film. After that, epitaxial growth is taking place for low-molecular fractions that later crystallize the surface of the dendrite-like backbone. Thus, a beam structure is built of the lamellas with epitaxial recrystallization on the beam section that acts as a substrate for the drying solution. Reduced lamellar beam thickness after laser irradiation demonstrates that in the irradiated solution the cluster sizes are reducing considerably, which results in nuclei size reduction during film drying [8].

The experimental study consisted of two stages: the first stage was investigating structural changes in blood plasma depending on laser exposure time; the second stage was investigating the stability of structural changes depending on the time after laser irradiation stopped.

At each stage, four sets of experiments were conducted. First, each set of experiments involved selecting blood plasma samples that had not been subjected to radiation. Then the plasma was placed into a cuvette and subjected to laser radiation. After 1, 2, 5, 10 and 20 min a 1 ml blood plasma sample was taken from the cuvette. The sample was poured on the slide. After drying, the sample was examined under a microscope at low magnification (10×) to record the obtained segments for each sample. Later on, calculations were made to define the statistical significance of the changes in a number of segments after exposure.

At the second stage, the radiated plasma in the cuvette was placed into a thermostat (at the temperature of 37 °C) to simulate physiological conditions. Further, the contents were poured on the substrate again 24, 36 and 48 h after laser exposure.

Along with sample collection, to obtain crystallograms at temporal control points, recordings were made of the speckle pattern obtained during laser radiation passing through the plasma cuvette. The installation diagram is shown in Fig. 1: laser radiation when passing through the cuvette with the test fluid scattered forming a speckle pattern on the recorder (CCD camera – Genius iLook 320). As is well-known, the speckle size on the speckle pattern is inversely related to the characteristic inhomogeneity size in the exposed medium. That is why changes in the speckle characteristic size reflect the changes in the inhomogeneity size in the test fluid.

To assess the speckle size, the wavelet analysis method was used. A section of 400 × 400 pixels was cut out of the speckle pattern, then a diagonal data line was selected on this section for wavelet transform. As the mother wavelet, the Morlet wavelet was used [9, 10].

Wavelet analysis makes it possible to determine the signal hidden periodicity. If a signal is a dependence of some parameter on time, the wavelet transform is able to determine not just the frequency but the characteristic change period of this process (a so-called time scale) as well as localization of this scale over time. If the test signal is the amplitude dependence on the spatial coordinates (as with our case), the wavelet analysis demonstrates the characteristic spatial period, i.e. the spot size of the speckle pattern. The results of the wavelet transform are presented as a skeleton: along the x-axis are the pixels of the original speckle pattern, along the y-axis is the spatial scale, i.e. a characteristic speckle size (also in pixels), the amplitude is marked in colour (black is zero, white is one).

A true advantage of wavelet processing of speckle patterns is its speed and visual clarity. A limitation of this method is that it is able to process only one line of the whole speckle pattern, which can result in the loss or distortion of the information contained in the whole speckle field. The success of the wavelet analysis is also considerably dependent on the choice of the mother function – the more it is symbatic to the intensity distribution in the speckle spot the better is the result.

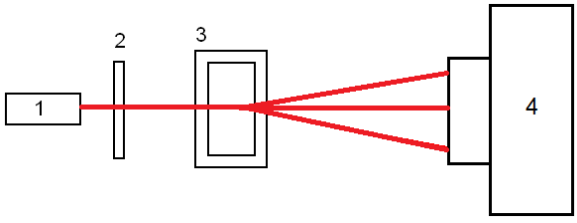


Fig. 1 Scheme of obtaining speckle patterns: laser radiation from source 1 is passing through light filter 2 and gets to fluid cuvette 3 where it interacts with structure inhomogeneities and forms a speckle pattern which is recorded by CCD camera 4.

An alternative to the wavelet analysis method is calculating the coefficient of correlation between the test image and a regular structure of the chessboard type with a variable size of squares. The result of calculating the

correlation field is the array of the correlation coefficients that can be presented graphically as a surface with a number of peaks. The bigger the coefficient of auto-correlation the higher is the peak [5, 6, 11].

It is worth mentioning that if the square size and the speckle characteristic size coincide, the correlation peaks of regular conical shape are alternating at regular intervals. If the chessboard square size and the speckle size do not coincide, the correlation peaks will deform and become double-humped or concatenate [6, 11].

2.2 Experimental data

Crystallographic method of evaluating the inhomogeneity size has revealed that under laser radiation an oscillation behaviour took place. Drastic decrease in the segment size at short exposure times with further increase in the segment size (till the fifth minute) and then a smoother decrease (Fig. 2 demonstrates the averaged graph of changes for all sets). Statistical processing of the results of all 4 sets has demonstrated that these changes are not accidental. The crystallogram segment size decrease reaches 50% whereas the measurement error is 18–35% depending on the particular time point. Moreover, the behaviour (decrease – increase – decrease) was similar for all the sets, even though it had a different absolute value in each set.

The results of wavelet analysis for the diagonal line of the speckle patterns are shown in Fig. 3: along the x-axis are the pixels of the original speckle pattern. Along the y-axis is the spatial scale, i.e. a characteristic speckle size in pixels. The amplitude is marked in colour (black is zero, white is one).

Analysis of Fig. 3 shows that before laser exposure, two series of maximums are observed. For the 20 pixel scale and for the 30 pixel scale, which corresponds to the actual speckle size of 125–190 μm. After 5 min exposure, a clear series of maximums was defined (the speckle size is about 250 μm), however, at the same time the small-scale component of about 10–15 pixels (the presence of 60–90 μm speckles) had comparatively large amplitudes, which indicates a considerable instability of inhomogeneity sizes in the test solution. Further extending the time of laser exposure, increases the contribution of the large-scale components, which reflects the decrease in the inhomogeneity size in plasma. In general, it would be safe to say that the speckle characteristic size increases from 20–30 to 30–40 pixels, which corresponds to the actual change of the speckle size from 125–190 μm to 190–250 μm, i.e. 1.5–2 times.

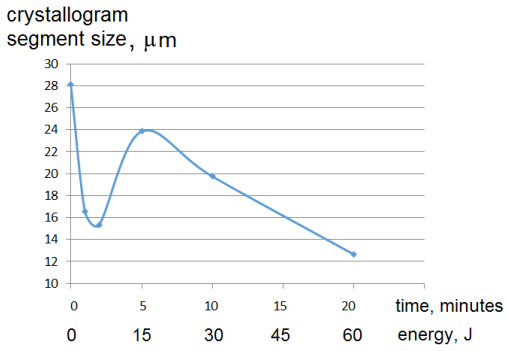


Fig. 2 Changes in the crystallogram segment average size depending on the time of blood plasma laser exposure: along the y-axis is the crystallogram segment size in μm.

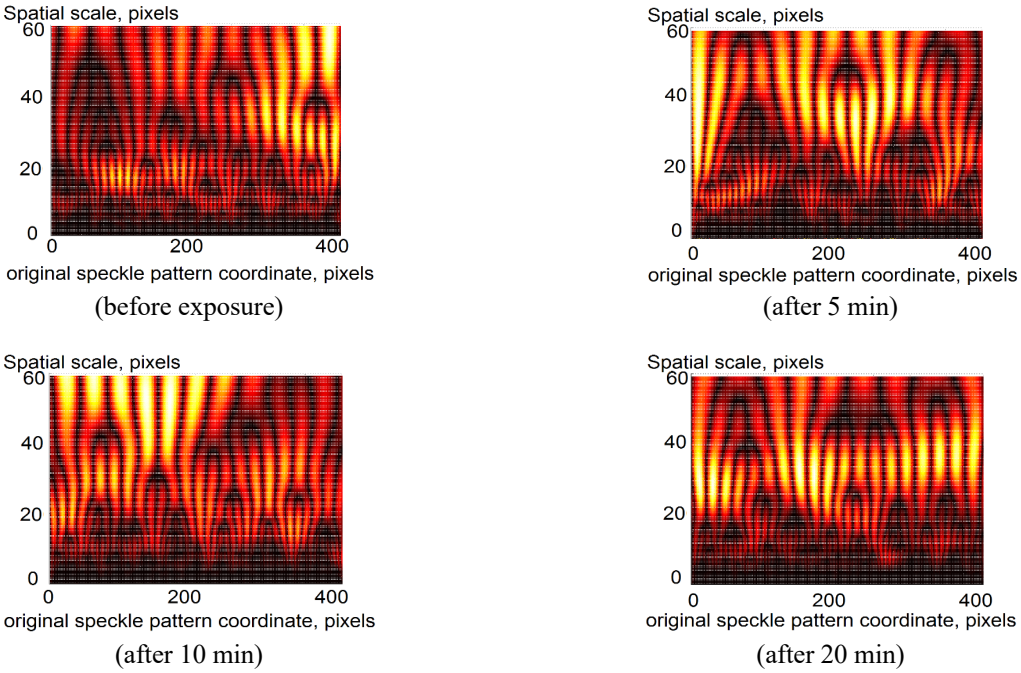


Fig. 3 The results of wavelet analysis of the diagonal line of the speckle pattern depending on the time of blood plasma laser exposure.

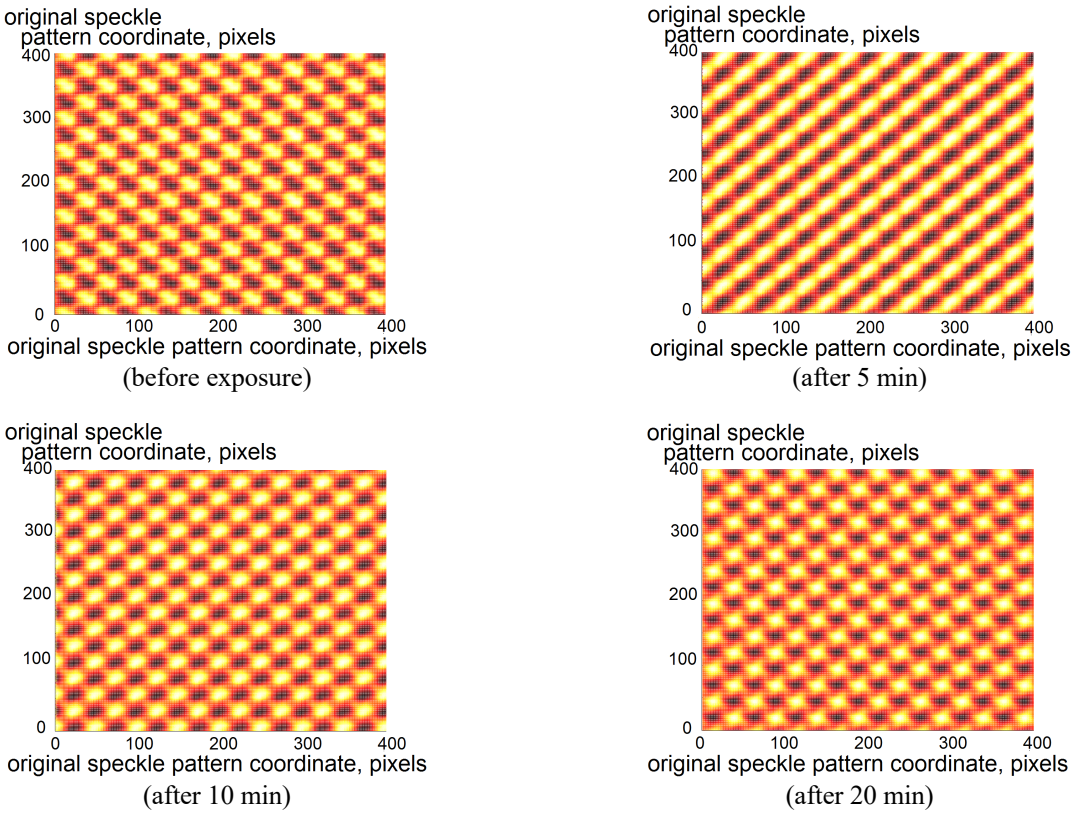


Fig. 4 The results of calculating the correlation coefficient between the speckle pattern and a regular structure of the chessboard type with the square size of 25 × 25 pixels. Along the axes are the pixels of the original speckle pattern, the correlation coefficient amplitude is marked with colour: black is zero, white is one.

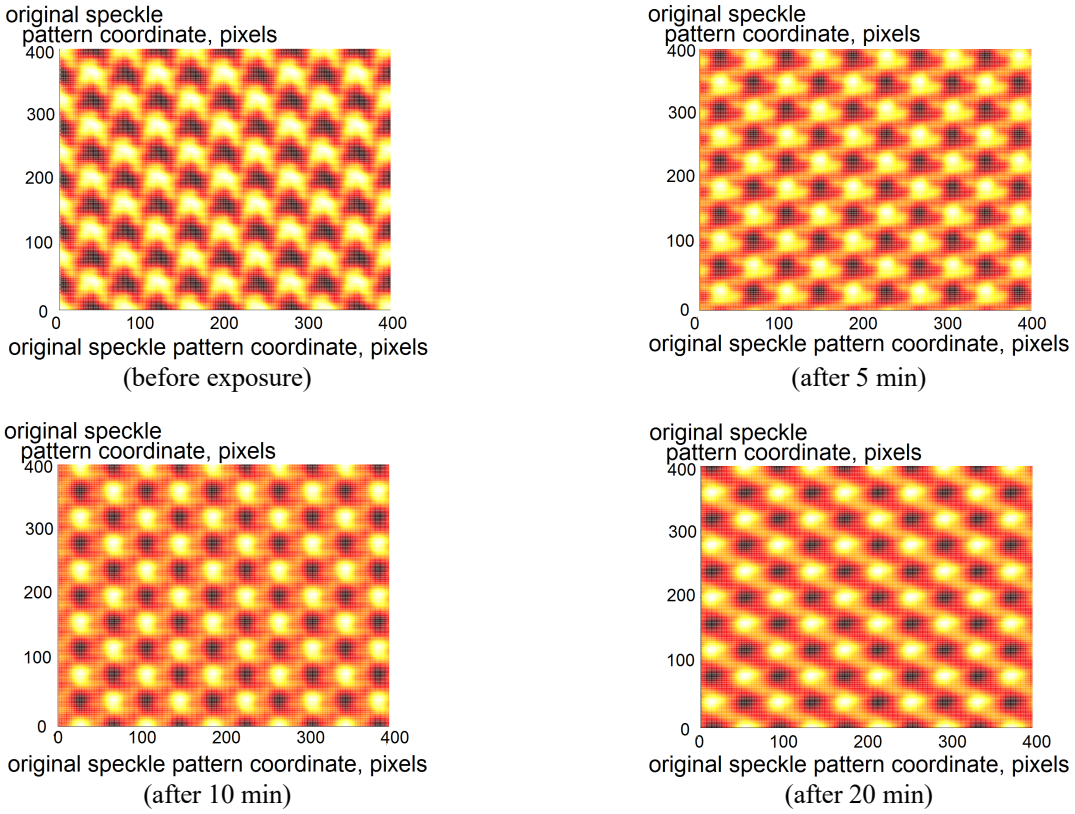


Fig. 5 The results of calculating the correlation coefficient between the speckle pattern and the regular structure of the chessboard type with the square size of 40 × 40 pixels. Along the axes are the pixels of the original speckle pattern, the correlation coefficient amplitude is marked with colour: black is zero, white is one.

The results of calculating the coefficient of correlation between the speckle pattern and a regular structure of the chessboard type are shown in Figs. 4–5. For convolution 2 chessboards were selected: with the square size of 25 × 25 and 40 × 40 pixels. Calculating the correlation field results in the array of the correlation coefficients that can be presented graphically as a surface with a number of peaks. The bigger the coefficient of auto-correlation, the higher is the peak.

Coincidence of the speckle size with the chessboard square size forms a regular conical maximum whose top view is thus a clear round spot. Fig. 4 shows that the correlation field from the reference sample has characteristic twin maximums, which takes place when the speckle size is somewhat smaller than the chessboard square size. From the speckle pattern obtained after 5 min laser exposure, we can observe some joined correlation peaks, which is characteristic in cases where the speckle size is somewhat larger than the chessboard square size. The most pronounced correlation peaks for convolution with the chessboard of 25 × 25 pixels can be observed for the speckle pattern obtained after 10 min laser exposure. For the correlation pattern after 20 min exposure, the maximum is rather diamond-shaped because there is a complex maximum in the form of the central peak with 4 additional maximums at its base. Such picture emerges when the speckle size does not agree with the size of the chessboard square size.

Analysis of the correlation fields shown in Fig. 5 demonstrates that before the exposure and at short (5 min) exposures, the characteristic speckle size is smaller than the chessboard square. This results in considerable deformation of the correlation peaks and emergence of the twin peak. With the increase in the laser exposure time to 10 min, the correlation maximums obtain a regular form indicating the agreement between the characteristic speckle size and the chessboard square size (40 pixels). In the case of the correlation field for the speckle pattern obtained after 20 min plasma irradiation, the maximums concatenate. This reflects further increase in the speckle characteristic size.

Thus, the method of calculating the correlation coefficient between the speckle pattern and the regular chessboard-type structure has shown that the characteristic speckle size is gradually increasing, which reflects the decrease in the inhomogeneity size and is in good agreement with the results obtained by the crystallography method.

The second stage of the experiment was aimed at the investigation of the relaxation processes and determining the time during which the structural changes caused by a single laser exposure remain in blood plasma. Investigating relaxation processes in protein solution [12] has shown that they lead to gradual increase in the protein macromolecule cluster sizes in a solution with the structural changes caused by laser radiation remaining for no longer than 24 h. On the strength of these data we suggested that in blood plasma the relaxation processes should proceed in a similar way. However, taking into account a more diversified composition of protein components in plasma compared to the model solution, we assumed that the processes of restoring the primary plasma structure should proceed slower, therefore the observation time was prolonged to 48 h. The results of investigating the plasma structural changes by the crystallography method are shown in Fig. 6 (the averaged data of 4 sets).

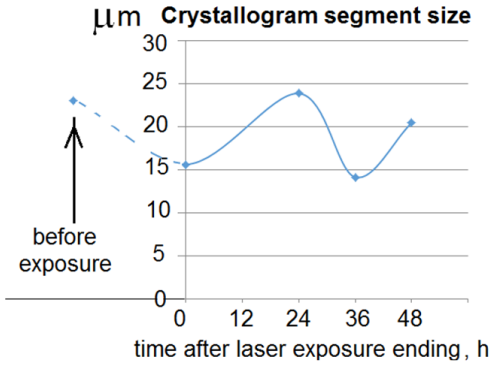


Fig. 6 Changes in the crystallogram segment average size depending on the time after laser exposure to blood plasma: along the y-axis is the crystallogram segment size in μm.

The experiment has revealed that the changes in plasma structure caused by laser exposure have an oscillation character that took place in all the 4 sets of the experiment. The measurement error was 6–17%, which is considerably less than the relative amount of change that was 30–50%. 24 h after the exposure starts, the system returns to the non-irradiated state. However, then the structure characteristic size decreases again and completely resets to the non-irradiated state no earlier than 48 h after the laser exposure ending.

3 Discussion

Since plasma is a cell-free protein solution, it is obvious that the target of laser exposure are proteins. In our opinion, there may be two different scenarios of interaction of laser radiation with protein molecules.

As is well-known, at different levels of protein molecule arrangement there are chemical bonds of different strengths: the primary structure has peptide bonds (covalent bonds, strong); the secondary structure has hydrogen bonds (weak); the tertiary structure has hydrogen hydrophobic interactions (weak), and sometimes disulphide bonds (strong); the quaternary structure (for certain proteins) has ion, hydrogen, hydrophobic interactions (weak). The energy of the laser radiation quantum in the employed range is too small to break the peptide or disulphide bonds (whose energy is hundreds of kJ/mole) but is sufficient to break the hydrogen bonds (whose energy is tens of kJ/mole) or to destabilize the hydrophobic section because in these cases the bond energy is an order of magnitude less than that with covalent interaction [13, 14]. That is why laser radiation is capable of changing the secondary, tertiary and quaternary protein structures without affecting the

primary structure, which results in both dissolved configuration of certain molecules and of larger supramolecular complexes into smaller ones.

The second scenario is related to the presence of the hydration shell around the protein molecule. Consequently, laser radiation capable of energizing a protein molecule, is able to destabilize the hydration shell of the protein molecules making structural changes easier. Moreover, the radiation is capable of disturbing the thermodynamic equilibrium of the protein and breaking the weak bonds inside the molecule at the secondary and/or tertiary organisation level thus causing structural changes [14].

Refs. [2, 15] revealed the influence of laser radiation on the secondary and tertiary structures of blood proteins with blood haemoglobin as the main laser radiation acceptor. It is noted that the changes detected in whole blood are much more pronounced than the changes in plasma. However, our findings demonstrate the presence of structural changes in plasma. Therefore, we believe that the role of plasma proteins in the response of living bodies to laser radiation is no less crucial than the role of blood cell components.

Ref. [16] suggests that pulsed magnetic field can cause conformational changes in the hydration shell of antibiotic molecules, which results in the changes of its activity. We believe that in the interaction between laser radiation and protein water solutions (which includes blood plasma), it is equally important to consider the role of the macromolecule hydration shell as well as the ability of the macromolecules themselves to make associates [17], which affects its functional activity.

Therefore, the interaction of laser radiation with plasma proteins can be described as follows. First, the proteins receive additional energy in the form of laser radiation, which changes the balance of interaction forces between the protein and its hydration shell and enables the proteins to release from it. Without hydration shell they start interacting between themselves and with the charged ions forming large conglomerates. Concurrently, structural changes of protein molecule are taking effect. Due to excess energy, weak bonds are breaking, protein is changing its structure and its activity is altering.

Thus, the oscillation changes in the structure characteristic size in plasma under the laser irradiation and in the relaxation process after laser exposure are connected with two contrary processes. On the one hand, destabilization of the hydration shell, increased mobility of certain parts of macromolecules and their charged groups lead to loosening of associates and possibility to interact with other protein molecules, thus making large associates. On the other hand, macromolecules, when disengaged from the associate and due to extra energy, are able to convolute themselves in such a way that their dipole moment is equal to zero and their further interaction with other macromolecules is reduced to minimum. After the fifth minute, we can observe that the process of building small closely-packed protein formations is dominating over the process of building large associates.

Protein structural changes under laser radiation and may have a beneficial effect, because radiation itself does not typically cause serious damage. Some proteins will restore independently after a while, and, at the same time some proteins can get activated in the living system. For instance, laser radiation, being a stress factor, can facilitate heat-shock protein synthesis – a class of proteins synthesized when structural changes of normal protein molecules are detected and responsible for restoring the regular structure and assembly of other proteins; participating in the immune response [18, 19]. Therefore, changes in the functional activity of some proteins effect the structure and production of others, which, in total, ensures a complex immune response not only in the affected area but in the body as a whole.

4 Conclusion

When affected by laser radiation with 532 nm wavelength, blood plasma structure is changing and these changes have an oscillatory character: with a short exposure time (1–2 min), the characteristic structure size reduces, then begins to grow once more and after that (the exposure time over 10 min) gradually decreases again. Various techniques of recording structural changes, e.g. by means of crystallograms and of processing speckle patterns obtained during laser radiation through plasma, have shown similar results: under laser radiation, blood plasma undergoes a reduction to a factor of 1.5–2 in the characteristic size of inhomogeneities. Oscillation changes of inhomogeneity size are likely explained by two competing processes related to the changes in protein molecules themselves and their hydration shells when blood plasma is exposed to laser radiation.

Examining the plasma structure relaxation processes after laser exposure has also revealed oscillation of the changes, which can call for further studies.

Disclosures

All authors declare that there is no conflict of interests in this paper.

References

1. A. V. Kartelishev, A. G. Rumyancev, A. R. Evstigneev, A. V. Geiniz, and S. V. Usova (Eds.), Lazernaya terapiya i profilaktika, Prakticheskaya meditsina, Moscow, Russia (2012) [in Russian]. ISBN 978-5-98811-219-8.
2. G. A. Zalesskaya, E. G. Sambor, "Interaction of low-intensity laser radiation with blood and its components," Journal of Applied Spectroscopy 72(2), 230–235 (2005) [in Russian].

3. A. N. Malov, A. Yu. Seteikin, A. V. Neupokoeva, E. S. Musatova, I. E. Golub, L. V. Sorokina, V. S. Fetschenko, and A. A. Vaichas, "The laser radiation action on the biological objects," Optik 124(23), 6034–6041 (2013).
4. S. V. Moskvin (Ed.), Osnovy lazernoy terapii. Seriya "Effektivnaya lazernaya terapiya," Triada, Tver, Russia (2016) [in Russian]. ISBN 978-5-94789-738-8.
5. P. V. Pavlov, A. N. Malov, and A. V. Neupokoeva, "Determination of the working fluids technical condition by analysis of digital speckle images parameters," in Proceedings of VII International Conference on Photonics and Information Optics (PhIO), National Research Nuclear University Mephi, Moscow, 490–497 (2018) [in Russian].
6. A. V. Neupokoeva, A. N. Malov, "Comparative analysis of structural changes in fluid media monitoring methods," Izvestiya vyshih uchebnyh zavedeniy. Physica 58(11–3), 164–168 (2015) [in Russian].
7. A. V. Gheinits, S. V. Moskvin, and A. A. Anchilov, Intravenous laser blood irradiation, Triada, Tver, Russia (2012) [in Russian].
8. Y. Y. Tarasevich, "The models and mechanisms of the dehydration self-organization of biological fluids," Physics-Uspekhi 47(7), 717–728 (2004).
9. I. M. Dremin, O. V. Ivanov, and V. A. Nechitailo, "Wavelts and their uses," Physics-Uspekhi 44(5), 447–478 (2001).
10. N. M. Astaf'eva, "Wavelet analysis: basic theory and someapplications," Physics-Uspekhi 39(11), 1085–1108 (1996).
11. A. N. Malov, A. V. Neupokoeva, "A chessboard method for the speckle images analysis," in Collection of works of the 10th International Conference "GoloExpo 2013", Moscow, 257–264 (2013) [in Russian].
12. K. V. Rogova, E. R. Gerok, and A. V. Neupokoeva, "Investigation of the protein solution structure relaxation processes after laser exposure," in Proceedings of the XVIII All-Russian Youth Samara Competition-Conference of Scientific Papers on Optics and Laser Physics, P. N. Lebedev Physical Institute of the Russian Academy of Sciences, Moscow, 326–332 (2020) [in Russian].
13. N. L. Glinka, General chemistry, Integral-Press, Moscow, Russia (2003) [in Russian].
14. A. V. Finkelshtein, O. B. Ptitsyn (Eds.), Fizika belka, KDU, Moscow, Russia (2012) [in Russian].
15. G. A. Zalesskaya, I. I. Kalosha, "Effect of in vivo irradiation of blood by low-intensity emission from a He-Ne laser on the molecular components of blood," Journal of Applied Spectroscopy 76(5), 720–726 (2009).
16. V. A. Glushchenkov, T. I. Vasilyeva, I. A. Belyaeva, N. A. Rodenko, A. K. Madyarova, and R. J. Jusupov, "Changes in the antibacterial activity of benzylpenicillin exposed to a pulsed high-intensity magnetic field," Biophysics 64(2), 214–223 (2019).
17. V. D. Lakhno (Ed.), Klastery v fizike, khimii, biologii, Regulyarnaya i khaoticheskaya dinamika, Izhevsk, Russia (2001) [in Russian]. ISBN 5-93972-060-9.
18. M. Nishikawa, S. Takemoto, and Y. Takakura, "Heat shock protein derivatives for delivery of antigens to antigen presenting cells," International Journal of Pharmaceutics 354 (1–2), 23–27 (2008).
19. S. Walter, J. Buchner, "Molecular chaperones – cellular machines for protein folding," Angewandte Chemie International Edition 41(7), 1098–1113 (2002).

Measurement of Silicon Nanoparticles Temperature by Raman Spectroscopy

Alida F. Alykova[1,2*], Maria S. Grigoryeva[1,3], Irina N. Zavestovskaya[1,3], and Victor Yu. Timoshenko[1,3,4]

[1] National Research Nuclear University MEPhI (Moscow Engineering Physics Institute), 31 Kashirskoe shosse, Moscow 115409, Russian Federation

[2] Prokhorov General Physics Institute of RAS, 38 Vavilova str., Moscow 119991, Russian Federation

[3] P. N. Lebedev Physical Institute of the Russian Academy of Sciences, 53 Leninskiy Prospekt, Moscow 199991, Russian Federation

[4] Lomonosov Moscow State University, GSP-1 Leninskie Gory, Moscow 119991, Russian Federation

*** e-mail:** afalykova@mephi.ru

Abstract. The temperature of silicon nanoparticles under laser photo-induced heating is determined from the ratio of the intensities of the Stokes and anti-Stokes components of the Raman scattering. The obtained results of the dependence of nanoparticles temperature on the laser radiation intensity and the temperature dependence of the Raman line position may be used to determine the optimal regimes of photo-hyperthermia enhanced by silicon nanoparticles for cancer therapy. © 2021 Journal of Biomedical Photonics & Engineering.

Keywords: Raman scattering; nanoparticles; nanocrystalline silicon; porous silicon; hyperthermia.

Paper #3397 received 22 Dec 2020; revised manuscript received 24 Mar 2021; accepted for publication 24 Mar 2021; published online 30 Mar 2021. doi: 10.18287/JBPE21.07.010303.

1 Introduction

Silicon nanoparticles (Si NPs), including NPs of crystalline and porous silicon, are widely researched for biomedicine applications, in particular, as active elements of biosensors and as part of new drugs for theranostics (simultaneous diagnosis and therapy) of oncological and other socially significant diseases [1–6]. If the size of crystalline NPs is less than 10 nm, they exhibit photoluminescence in the biological transparency window (650–850 nm), which can be used for their visualization in cells and tissues [7–11]. The large Si nanoparticles (more than 10 nm) are in turn capable of providing nonlinear biovisualization mechanisms, such as two-photon luminescence and second harmonic generation, the combination of which makes it possible to effectively track both individual silicon NPs and their aggregation in different parts of the cell, while the resolution of such approach is sufficient to obtain 3D-images [12].

The simultaneous use of the diagnostic functionality of silicon nanoparticles and their therapeutic properties predicts the development of new methods of theranostics, in particular, the theranostics of cancer [13]. One of the fast growing areas of nanobiomedicine is the use of NPs as sensitizers of various therapies. In particular, silicon NPs are used in photohyperthermia techniques as a promising nanomaterial with biocompatible and biodegradable properties [14, 15].

The development of hyperthermia techniques raises the problem of heating temperature determining. There are two main techniques to measure temperature – contact and non-contact. Contact techniques are based on achieving a thermal equilibrium state of the measuring temperature transmitter (temperature sensors) with the studied object during their direct contact. The disadvantages of the contact technique are the distortion of the measured object temperature under introducing a thermometer into it; the temperature of the converter always differs from the actual temperature of the measured object; the temperature measurement range is limited by the properties of the temperature sensors materials. In addition, the problem of temperature measuring the in Si NPs cannot be solved by contact technique. Non-contact temperature measurements are carried out by pyrometers and thermal imagers. Existing non-contact thermal imaging thermometers are based on

measuring the infrared radiation intensity in a non-transparent region for living organisms [15, 16].

In the present work, we selected the Raman scattering spectroscopy method to Si NPs temperature monitor. As is known, the intensity of the Stokes and anti-Stokes lines depends on the temperature as a consequence of the Bose-Einstein statistics for the phonon [17]. Furthermore, the Raman scattering lines frequency changes with temperature due to the anharmonicity of lattice oscillations. In particular, this is realized at sufficiently intense photoexcitation causing the sample to heat up [18, 19]. We studied samples of nanocrystalline silicon (nc-Si) NPs as well as nanocrystalline mesoporous silicon (mPSi) films. The temperature change of the samples was achieved by changing the exciting laser radiation intensity. The experimental data obtained with nc-Si NPs and mPSi films confirmed the theoretical model developed in Ref. [19].

2 Experimental technique

Powders of nc-Si were prepared by plasma-chemical synthesis using a plasmatron and pure (99.9 %) microcrystalline Si [1]. Aqueous suspensions were obtained by adding nc-Si to deionized water to achieve a concentration of 1 g/L. In the experiment, 50 µl drop planted on a metal substrate and dried was used. Silicon NPs have a spherical shape and a wide size distribution in the range from 10 to 150 nm. The size distribution has major maxima at 50–120 nm [4]. An argon laser with λ_{ex} = 514.5 nm and a maximum power of 0.2 W was used as an exciting radiation source. The laser beam was focused on nc-Si sample with 3 µm diameter.

MPSi samples were formed by electrochemical etching substrates of c-Si in an ethanol solution of hydrofluoric acid. The method consists in the formation of mesoporous silicon films with a thickness of 50 to 100 µm, a porosity of 50 to 80%, and a pore size of 2 to 5 nm on the surface of c-Si substrates p-type conductivity with a resistivity of 10 to 50 mOm × cm. The source of exciting radiation for the mPSi heating was a semiconductor laser with a wavelength λ_{ex} = 633 nm and a maximum power of 70 mW.

The Raman spectra of nc-Si samples were taken on the DFS-52 spectrometer in 90-degree scattering geometry. The receiver served working in the photon counting mode a cooled photomultiplier tube PMT–79. The diffraction grating of the spectrometer was 1800 g/mm. The spectral resolution was 0.1 cm^{-1}. The mPSi samples were investigated on a Confotec MR–350 setup equipped with an optical microscope, which allowed us to obtain the micro-Raman spectra with a spatial resolution of the order of 1 µm and a spectral resolution of 1 cm^{-1}.

3 Results and discussion

The Stokes and anti-Stokes Raman spectra of nc-Si samples at different powers are shown in Fig. 1. With the increase of the excitation power level, a shift in the spectra to lower frequencies region is observed, which is caused by the increase of sample temperature during photoinduced heating [19]. Simultaneously with the increase of the excitation power, a change in the ratio between the Stokes and anti-Stokes scattering components intensities is observed.

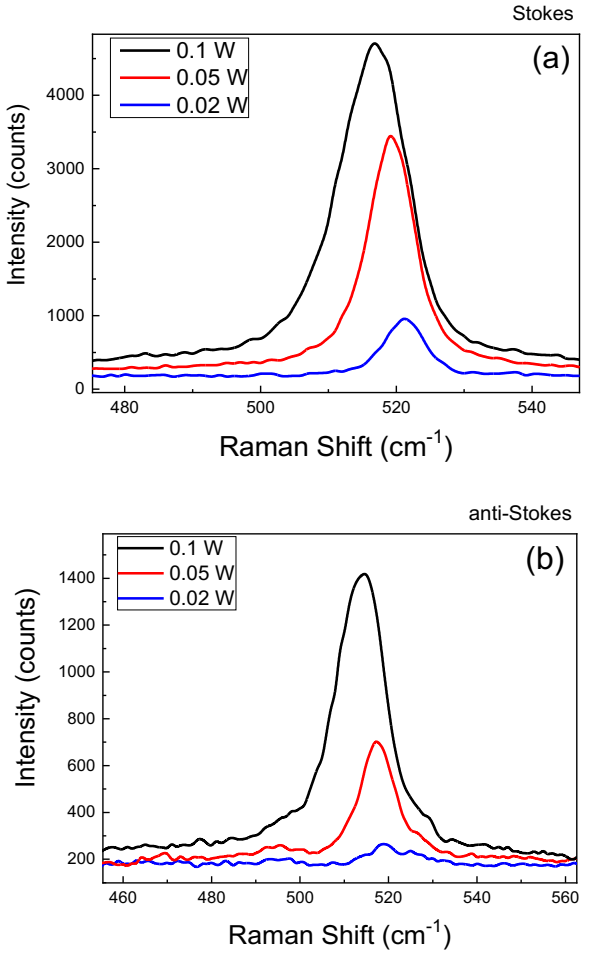


Fig. 1 Raman spectra of nc-Si samples in Stokes (a) and anti-Stokes (b) scattering at λ_{ex} = 514.5 nm.

From the ratio of the Stokes and anti-Stokes components intensities, the NPs temperature can be estimated using the following formula [17, 20]:

$$\frac{I_S}{I_A} \approx exp\left(\frac{\hbar\omega}{kT}\right), \quad (1)$$

where I_S и I_A are Stokes and anti-Stokes lines intensities, ω is phonon frequency, $k = 1.38 \times 10^{-23}$ J/K, $\hbar = 1.05 \times 10^{-34}$ J×s. Eq. (1) follows from the Bose-Einstein statistics for phonons, neglecting the difference in the absolute values of frequencies and absorption coefficients of the Raman components [17].

Fig. 2 shows the dependence of the I_S / I_A value on the laser radiation intensity, which is almost linear. The decrease of the I_S / I_A value with the increase of the excitation intensity is explained by the photoinduced heating of nc-Si. From Eq. (1), the nc-Si temperature in the excitation region can be estimated by the formula:

$$T = \frac{\hbar\omega}{k\,ln\left(\frac{I_S}{I_A}\right)}. \quad (2)$$

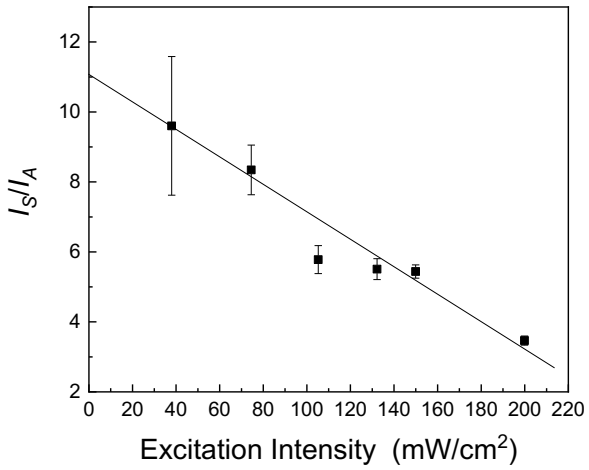


Fig. 2 Dependence of the ratio of the Stokes and anti-Stokes components intensities on the laser radiation intensity with λ_{ex} = 514.5 nm.

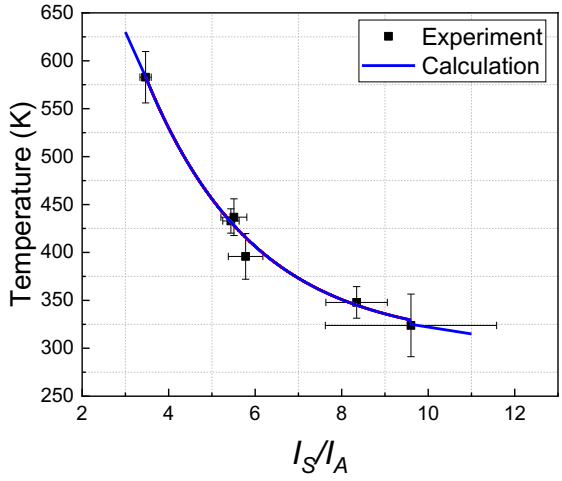


Fig. 3 Temperature dependence of the nc-Si sample on I_S / I_A at λ_{ex} = 514.5 nm. The dots represent the experimental values.

Fig. 3 shows the experimental values of the nc-Si temperature according to the Raman scattering data and the calculation values by Eq. (2). It can be seen that the experimental error is maximum in the low temperatures region, which corresponds to a very weak photoinduced heating of nc-Si, while the error decreases with increasing temperature. This is occurring due to the increase of the absolute the Raman signals intensities and the decrease of the measurement error of the I_S / I_A ratio. It should be noted that with the increase of the signal accumulation time, the measurement error of the latter value can be reduced to 1%, which will give an accuracy of the temperature determining of the order of 10–15% in the temperature range of 310–320 K.

The dependence of the Raman line shift on the photoinduced heating temperature obtained from the analysis of the spectra in Fig. 1 is shown in Fig. 4. The Raman line temperature shift to the lower frequencies region is in good agreement with the literature data for crystalline and nanocrystalline silicon [18, 19]. The observed linear temperature dependence is convenient to analyze the Si NPs photoinduced heating.

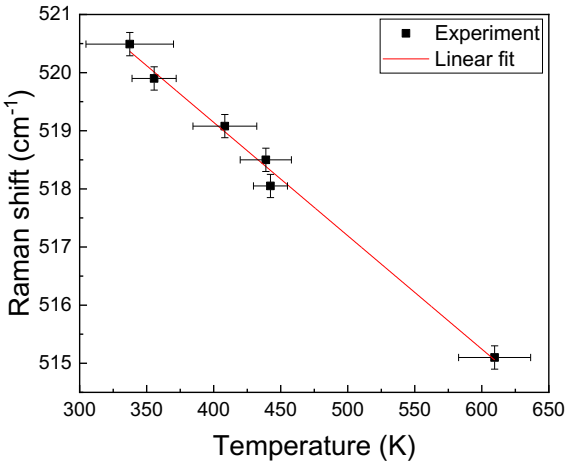


Fig. 4 Raman shift of the nc-Si sample as a function of its temperature at λ_{ex} = 514.5 nm.

The Stokes Raman spectra of mPSi samples at different powers are shown in Fig. 5. Fig. 6 shows the position of the Raman line maximum, taking into account the data in Fig. 4, as a function of the photoinduced heating temperature. It can be seen that, regardless of the type of nanostructures and the method of their preparation, an almost linear temperature dependence of the Raman peak position is observed. It should be noticed that the absolute positions of the Raman peak frequencies for nc-Si and PSi are 0.5–0.7 cm^{-1} less than those for the c-Si sample taken from the literature, which can be associated with both the accuracy of the Raman frequency determination and with the size effect for phonons in silicon nanocrystals [19].

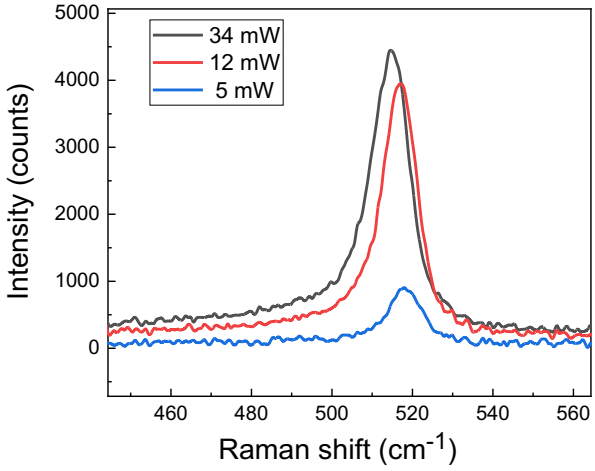


Fig. 5 Stokes Raman spectra of mPSi samples at λ_{ex} = 632.5 nm.

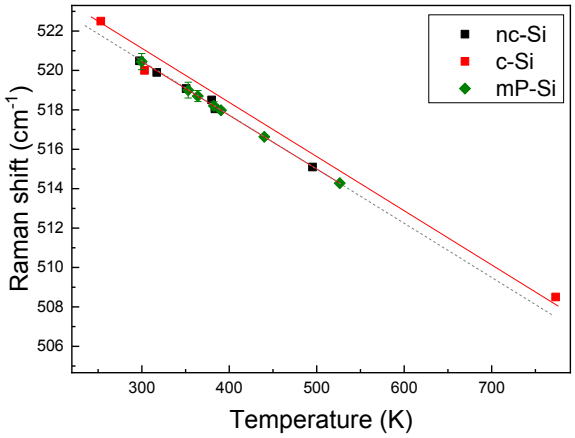


Fig. 6 Raman shifts of the nc-Si sample (black squares) and mPSi (green rhombuses) as a function of temperature, and their approximation (dotted line). The red squares correspond to c-Si [19].

4 Conclusions

The temperature effect of laser radiation on the Raman spectra of nc-Si and mPSi is studied. Measuring the ratio of the Stokes and anti-Stokes components intensities allows us to determine the temperature with a minimum error at temperatures above 350–400 K. It is found that with temperature increase during photoexcitation, the Raman line frequency decreases linearly, which makes it possible to use this dependence to accurately determine the temperature even at low heating.

The results obtained can be used to determine the optimal regimes of photo-hyperthermia upon sensitization with silicon nanocrystals in cancer therapy. The optimal regime of hyperthermia in general, and photo-hyperthermia in particular, is defined by the advisable local temperature, which must be achieved to obtain a therapeutic effect in the selected area, on the one hand, and not leading to irreversible changes in healthy tissues, on the other hand. The temperature shift of the Raman spectrum components observed in silicon nanocrystals allows us to determine the photoinduced heating value with high precision, thus selecting the required radiation power individually in each case.

Disclosures

All authors declare that there is no conflict of interests in this paper.

Acknowledgements

The authors thank Prof. A. A. Ishchenko for providing the samples of nanocrystalline silicon and Dr. A. Yu. Kharin for helpful discussions.

The reported study was funded by RFBR, project number 20-02-00861.

References

1. A. A. Ischenko, G. V. Fetisov, and L. A. Aslanov, Nanosilicon: Properties, Synthesis,Applications, Methods of Analysis and Control, CRC Press, Boca Raton, USA (2014). ISBN 978-1-4665-9423-4.
2. A. V. Kabashin, V. Yu. Timoshenko, "What theranostic applications could ultra-pure lasersynthesized Si nanoparticles have in cancer?" Nanomedicine 11(17), 2247–2250 (2016).
3. L. A. Osminkina, V. Yu. Timoshenko, "Porous Silicon as a Sensitizer for Biomedical Applications," Mesoporous Biomaterials 3, 39–48 (2016).
4. Yu. V. Kargina, A. M. Perepukhov, A. Yu. Kharin, E. A. Zvereva, A. V. Koshelev, S. V. Zinovyev, A. V. Maximychev, A. F. Alykova, N. V. Sharonova, V. P. Zubov, M. V. Gulyaev, Y. A. Pirogov, A. N. Vasiliev, A. A. Ischenko, and V. Yu. Timoshenko, "Silicon Nanoparticles prepared by plasma-assisted ablative synthesis: physical roperties and potential biomedical applications," Physica Status Solidi A 216(14), 1800897 (2019).
5. V. M. Petriev, V. K. Tischenko, A. A. Mikhailovskaya, A. A. Popov, G. Tselikov, I. Zelepukin, S. M. Deyev, A. D. Kaprin, S. Ivanov, V. Yu. Timoshenko, P. N. Prasad, I. N. Zavestovskaya, and A. V. Kabashin, "Nuclear nanomedicine using Si nanoparticles as safe and effective carriers of 188 Re radionuclide for cancer therapy", Scientific Reports 9(1), 1–10 (2019).
6. S. Kudryashov, A. Nastulyavichus, A. K. Ivanova, N. A. Smirnov, R. A. Khmelnitskiy, A. A. Rudenko, I. N. Saraeva, E. R. Tolordava, A. Yu. Kharin, I. N. Zavestovskaya, Y. M. Romanova, D. A. Zayarny, and A. A. Ionina, "High-throughput laser generation of Si-nanoparticle based surface coatings for antibacterial applications," Applied Surface Science 470, 825–831 (2019).
7. F. Erogbogbo, K. T. Yong, I. Roy, G. X. Xu, P. N. Prasad, and M. T. Swihart, "Biocompatible luminescent silicon quantum dots for imaging of cancer cells," ACS Nano 2(5), 873–878 (2008).
8. M. B. Gongalsky, L. A. Osminkina, A. Pereira, A. A. Manankov, A. A. Fedorenko, A. N. Vasiliev, V. V. Solovyev, A. A. Kudryavtsev, M. Sentis, A. V. Kabashin, and V. Yu. Timoshenko, "Laser-synthesized oxide-passivated bright Si quantum dots for bioimaging," Scientific Reports 6, 24732 (2016).
9. L. Gu, D. J. Hall, Z. Qin, E. Anglin, J. Joo, D. J. Mooney, S. B. Howell, and M. J. Sailor, "In vivo time-gated fluorescence imaging with biodegradable luminescent porous silicon nanoparticles," Nature Communications 4, 2326 (2013).

10. M. O. Morozov, A. V. Kabashin, V. Timoshenko, and I. N. Zavestovskaya, "Photoluminescence properties of silicon nanocrystals grown by nanosecond laser ablation of solid-state targets in an inert gas atmosphere," Bulletin of the Lebedev Physics Institute 44(12), 353–356 (2017).
11. A. F. Alykova, V. G. Yakunin, V. Yu. Timoshenko, and I. N. Zavestovskaya, "Optical methods of silicon nanoparticle diagnostics for applications in biomedicine," Journal of Biomedical Photonics & Engineering 5(2), 020304 (2019).
12. A. Yu. Kharin, V. Lysenko, A. Rogov, Y. V. Ryabchikov, A. Geloen, I. Tishchenko, O. Marty, P. G. Sennikov, R. A. Kornev, I. N. Zavestovskaya, A. V. Kabashin, and V. Yu. Timoshenko, "Bi-Modal Nonlinear Optical Contrast from Si Nanoparticles for Cancer Theranostics," Advanced Optical Materials 7(13), 1801728 (2019).
13. A. V. Kabashin, A. Singh, M. T. Swihart, I. N. Zavestovskaya, and P. N. Prasad, "Laser-Processed Nanosilicon: A Multifunctional nanomaterial for Energy and Healthcare," ACS nano 13(9), 9841–9867 (2019).
14. A. V. Kabashin, K. P. Tamarov, Yu. V. Ryabchikov, L. A. Osminkina, S. V. Zinovyev, J. V. Kargina, M. B. Gongalsky, A. Al-Kattan, V. G. Yakunin, M. Sentis, A. V. Ivanov, V. N. Nikiforov, A. P. Kanavin, I. N. Zavestovskaya, and V. Yu. Timoshenko, "Si nanoparticles as sensitizers for radio frequency-induced cancer hyperthermia," Proceedings of SPIE 9737, 97370A (2016).
15. C. Lee, H. Kim, C. Hong, M. Kim, S. S. Hong, D. H. Lee, and W. I. Lee, "Porous silicon as anagent for cancer thermotherapy based on near-infrared light irradiation," Journal of Materials Chemistry 18(40), 4790–4795 (2008).
16. A. Oleshchenko, A. Yu. Kharin, A. F. Alykova, O. V. Karpukhina, N. V. Karpov, A. A. Popov, V. V. Bezotosnyia, S. M. Klimentov, I. N. Zavestovskaya, A. V. Kabashin, and V. Yu. Timoshenko, "Localized infrared radiation-induced hyperthermia sensitized by laser-ablated silicon nanoparticles for phototherapy applications," Applied Surface Science 516, 145661 (2020).
17. M. Balkanski, R. F. Wallis, and E. Haro, "Anharmonic effects in light scattering due to optical phonons in silicon," Physical Review B 28(4), 1928–1934 (1983).
18. M. J. Konstantinovic, S. Bersier, X. Wang, M. Hayne, P. Lievens, R. E. Silverans, and V. V. Moshchalkov, "Raman scattering in cluster-deposited nanogranular silicon films," Physical Review B 66, 161311(R) (2002).
19. S. S. Périchon, V. Lysenko, B. Remaki, and D. Barbier, "Measurement of porous silicon thermal conductivity by micro-Raman scattering," Journal of Applied Physics 86(8), 4700 (1999).
20. I. H. Campbell, P. M. Fauchet, "The Effects of Microcrystal Size and Shape on the One Phonon Raman Spectra of Crystalline Semiconductors," Solid State Communications 58(10), 739–741 (1986).
21. L. A. Osminkina, K. A. Gonchar, V. S. Marshov, K. V. Bunkov, D. V. Petrov, L. A. Golovan, F. Talkenberg, V. A. Sivakov, and V. Yu. Timoshenko, "Growth, Structure and Optical Properties of Silicon Nanowires Formed by Metal-Assisted Chemical Etching," Nanoscale Research Letters 7(6), 602–606 (2012).

Flexible Computationally Efficient Platform for Simulating Scan Formation in Optical Coherence Tomography with Accounting for Arbitrary Motions of Scatterers

Alexey A. Zykov, Alexander L. Matveyev, Lev A. Matveev, Alexander A. Sovetsky, and Vladimir Y. Zaitsev*

Institute of Applied Physics Russian Academy of Sciences, 46 Ulyanova str., Nizhny Novgorod 603950, Russia

*** e-mail:** vyuzai@ipfran.ru

Abstract. A computationally efficient and fairly realistic model of OCT-scan formation in spectral-domain optical coherence tomography is described. The model is based on the approximation of discrete scatterers and ballistic character of scattering, these approximations being widely used in literature. An important feature of the model is its ability to easily account for arbitrary scatterer motions and computationally efficiently generate large sequences of OCT scans for gradually varying configurations of scatterers. This makes the proposed simulation platform very convenient for studies related to the development of angiographic processing of OCT scans for visualization of microcirculation of blood, as well as for studies of decorrelation of speckle patterns in OCT scans due to random (Brownian type) motions of scatterers. Examples demonstrating utilization of the proposed model for generation OCT scans imitating perfused vessels in biological tissues, as well as evolution of speckles in OCT scans due to random translational and rotational motions of localized (but not-point-like) scatterers are given. To the best of our knowledge, such numerical simulations of large series of OCT scans in the presence of various types of motion of scatterers have not been demonstrated before. © 2021 Journal of Biomedical Photonics & Engineering.

Keywords: OCT-scan formation; simulations of OCT scans; speckles in optical coherence tomography; optical coherence angiography; decorrelation of OCT scans.

Paper #3408 received 4 Mar 2021; revised manuscript received 19 Mar 2021; accepted for publication 20 Mar 2021; published online 31 Mar 2021. doi: 10.18287/JBPE21.07.010304.

1 Introduction

Optical coherence tomography (OCT) has proven to be a powerful tool for characterization biological tissue and diagnostics of various pathologies. In addition to utilization of conventional structural OCT images and solving problems related to enhancement of speed OCT visualization, improvement of resolution, etc., much attention has been paid in recent years to the development of various extensions/modalities of OCT to enable additional types of contrast, in particular, realization of polarization-sensitive OCT imaging [1, 2]. In recent years, some other OCT-modalities are emerging in biomedical research and clinical practice and have already proved their high utility for a broad range of various biomedical applications. In particular, one can mention OCT-based angiography [3–6] (already translated to some clinical applications, e.g., [7, 8]), mapping of viscous properties of biological liquids [9, 10], visualization of deformations (for elastographic and other applications) [11–14] including combined application of a few modalities [15, 16]. The principles of OCT-based elastography and angiography are essentially based on the analysis of motions of scatterers in acquired sequences of OCT scans.

Realization of such scatterer-motion-based modalities requires application of advanced signal-processing methods to extract signals related to

informative motions of scatterers and, in contrast, to filter out various kinds of distortions related to masking motions. For example, in OCT-angiography it is necessary to separate bulk motions of the "solid" tissue (due to breathing, heart-beat pulses, etc.) from the detected motion of scattering particles in the blood flow, which is not a trivial issue in living tissues [17]. For real biological tissues, performing experimental studies in highly controllable and reproducible conditions often is rather difficult or even impossible. By this reason, for validation and improvement of such OCT-based methods/algorithms for discrimination and quantitative assessment of motions of scatterers, researches often use phantom experiments with better controllable conditions [18, 19]. However, even in phantom experiments it is challenging to ensure the required properties of scatterers and parameters of their motions. Furthermore, for real physical experiments (even with phantoms), it is often impossible (or unacceptably complicated and expensive) to flexibly vary in sufficiently broad ranges various parameters/regimes of the used tissue samples, phantoms and OCT setup itself. In view of this, creating models of OCT-scan formation enabling realistic and flexible (in terms of properties of scatterers and OCT-system parameters) attracts high interest of researchers.

Among various approaches to such modeling it is reasonable to point out three main directions. An important group of such methods comprises various realizations of the Monte-Carlo approach, in which pseudo-random generation of trajectories for huge ensembles of photons is made to describe their propagation and scattering (such that multiple scattering can also be accounted for) [20–25]. Another group utilizes the concept of point-spread function [26, 27] and the third one comprises methods in which optical wave propagation, scattering and backward propagation and reception are consistently described. Such models can reasonably be called full-wave ones, although their realizations differ rather significantly and may comprise elements of analytical and numerical description in various combinations [28–36]. Their general feature is that in these methods the point-spread function and the entire speckle pattern are obtained by considering the illuminating-beam propagation first towards scatterers and then the wave scattering and subsequent propagation of the back-scattered field. Its collection over the receiving aperture is also considered. For example, in Ref. [28] wave-field propagation and collection is performed numerically or to a significant degree analytically as in works [32–34]. Quite a useful approximation in many models is the concept of discrete scatterers. However, the latter should not necessarily be sub-wavelength in size, so that even larger (but sub-resolution scatterers with sizes significantly smaller in comparison with the coherence length in the axial direction and the beam cross section laterally) can already be reasonably modeled as localized discrete elements.

For simulations of OCT scans related to the development of such extensions as the above-mentioned angiographic visualization, it is necessary to generate rather large volumes of OCT data scans imitating subsequent acquisition of large series of OCT scans. Therefore, unlike applications for which a single scan or a few scans may be sufficient, for generation of large blocks of OCT data, the ability of the model to perform simulations sufficiently rapidly becomes of key importance. Another requirement to the model is its ability to naturally account for arbitrary motion of scatterers. Such requirements are difficult to satisfy in models based on the Monte-Carlo approach or in computationally demanding essentially numerical variants of full-wave models. In what follows, we present a fast, simple and yet reasonably realistic model of OCT-scan formation based on the principles described in Refs. [32–34], in the framework of which arbitrary motions of scatterers can easily be introduced. Some examples demonstrating the usefulness of this model for simulations related to angiographic applications OCT will be presented.

2 Main features of the model

The approach used here is based on previous works [32–34], where the often-used approximation of ballistic single scattering was applied. This assumption is the basic principle of OCT-scan formation, for which effects of multiple scattering the illuminating beam and imperfectly ballistic forward propagation (because of fluctuations of the refractive index) play the role of distorting/degrading factors. Certainly, for some applications, such degrading factors may be also interesting to study (and they may be additionally introduced in modeling, like, e.g., in Ref. [36]). However, the very fact of successful realization of the OCT principle of imaging based on the ballistic approximation convincingly confirms that the ballistic scattering usually gives a strongly dominant contribution to the OCT-scan formation. Furthermore, even remaining within the ballistic approximation many important degrading factors can be efficiently studied, for example, strain-induced and displacement-induced decorrelation noises that are critically important for realization of OCT-based elastography [37–39]).

The next important note for the present study, is that in the majority of OCT setups the illuminating beams are intentionally weakly focused (with the focal plane located near the middle depth of scan). This allows one to obtain fairly invariable beam diameter enabling nearly uniform lateral resolution within the entire imaged depth (typically ~1–2 mm). Consequently, the illuminating beam in such setups remains close to cylindrical one with uniform diameter. Although the scattered field from localized scatterers, such as nuclei of cells in biological tissues, does not have pronounced directivity and may even be close spherically diverging, the same lens of the OCT setup that forms the highly directed illuminating beam also collects the scattered signal from the medium. As a result, even for isotropically scattering particles, the reception is highly directive, such that ballistically back-scattered components are mostly collected by the

received aperture. Consequently, the phase of the received signal is almost entirely determined by the forth-and-back propagation in the axial direction. For example, fairly small variations in the axial-distance by a quarter of wavelength causes the variation in the received-signal phase by π radians, such that constructive interference may become destructive and vice versa. In contrast, transversal coordinates of scatterers within the illuminating-beam cross section may experience even significantly greater variations with an insignificant effect on the received-signal phase (by this reason the transversal Doppler effect is known to be much smaller in comparison with the effect of axial motions with the same magnitude).

Bearing in mind the above-mentioned arguments, the proposed in Ref. [32] simple model of OCT-scan formation was based on the approximation of a cylindrical illuminating beam for which the transversal profile was supposed uniform for both phase and amplitude (see Fig. 1a). An additional simplification in Ref. [32] was that the amplitudes of the received signals were supposed to be independent of the depth. Despite the fact that the received amplitudes should actually demonstrate depth-dependence, for description of interferometric speckle formation, the absence of this dependence in modeling still is acceptable by the following reasons. Namely, for low-coherence OCT, the efficient mutual interference is possible only for small groups of scatterers located within sample volumes with the axial size limited by the rather small coherence length (typically ~5–10 μm). Consequently, in contrast to phases of scattered signals that may strongly vary for particles located within the sample volume, for the amplitudes of the received backscattered signals, the effect of the scatterer-depth variation within a particular sample volume is negligibly small. Therefore, for any particular depth, the speckle formation is fairly correctly described even neglecting the depth-dependence of amplitudes. However, if necessary, depth-dependent variations in the amplitude in the simulated OCT-scans on scales larger than the speckle size can readily simulated by introducing additional depth-dependent factors to imitate geometrical focusing/divergence of optical waves, their exponential decay due to both absorption and scattering (similarly to introducing these averaged factors in Monte-Carlo approaches). Also, if necessary, roll-off effects in spectral-domain OCT can also be accounted within the same basic assumptions (e.g., Ref. [35]).

Summation of individual spectral harmonics of the illuminating beam in such a model naturally describes the formation of the point-spread function in the axial direction. Such features of model [32] made it possible to efficiently use it for studying in detail the role of variation in the optical-spectrum width on the feasibility of correlational speckle tracking in OCT images of strained materials [37]. The intrinsic exceptional ease in accounting for displacements of scatterers in simple model [32] has also been very efficiently applied for studying important features of strain mapping in phase-resolved OCT [38–41]. The results of those simulations then have been successfully transferred for mapping strains and elasticity in numerous real situations, in which scatterers experienced predominantly axial interframe displacements [12, 42–44]. Sufficient correctness of elastographic simulations based on Ref. [32] has been later verified by comparison with more advanced realizations of this approach in works [33, 34], in which rigorous consideration of forward propagation of Gaussian illuminating beams with various degrees of focusing (see Figs. 1b and 1c), backward propagation of scattered signals and accurate description of their collection over the receiving aperture were performed.

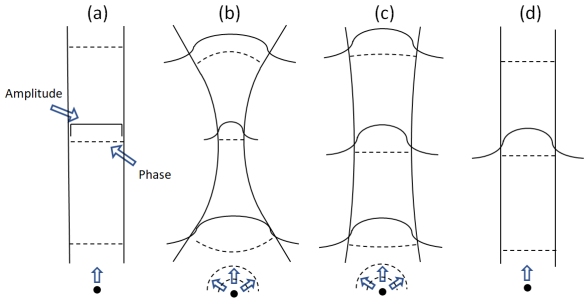


Fig. 1 Characteristic geometries of illuminating beams. (a) is a cylindrical beam with invariable width and uniform phase and amplitude distributions as used in model [32]; (b) pronouncedly focused Gaussian beam used in models [33, 34]; (c) a weakly focused Gaussian beam rigorously studied in Ref. [33] with accounting for the scattering-field divergence and high directivity of the signal reception; (d) the beam form, which is intermediate between the cases (a) and (c), such that the beam amplitude is approximated by a depth-independent Gaussian profile, whereas the phase is uniform in the cross section. This approximation is used in the following sections to reasonably well imitate weakly-focused beam in angiography-related simulations.

The result obtained in Ref. [33] demonstrated that, for a weakly focused beam, only a slight modification of the illuminating beam form in model [32] already gives OCT scans very similar to the results of rigorous consideration of a weakly diverging Gaussian beam with the same width in the focal region. Namely, instead of uniform amplitude distribution as in Fig. 1a, one may use a beam with a depth-independent Gaussian amplitude profile and uniform distribution of phase as in Fig. 1d. It is interesting that similarly to the assumption adopted in simplified model [32], for a rigorously simulated weakly focused Gaussian beam, the amplitude of the point-spread function demonstrates a very weak dependence on the depth (see examples of such a comparison in Ref. [33], Figs. 2a and 2b). The reason for this nearly depth-independent amplitude is due to interplay between the influence of divergence of scattered waves and their collection over the receiving-lens aperture, see details in Ref. [33]. Therefore, the modification of the beam as shown in Fig. 1d in model [32] gives results very close to

those for rigorous consideration of OCT-scan formation for weakly focused Gaussian beams. Bearing in mind that such beams are often used in realizations of OCT-angiography to enable nearly depth-independent lateral resolution, the so-modified model [32] can be efficiently applied for simulations of angiographic processing as demonstrated below.

As depicted in Fig. 1d, the illumination-beam intensity has a Gaussian profile $T(x,y)$:

$$T(x,y)=\exp\left(\frac{-(x^2+y^2)}{W^2}\right), \quad (1)$$

where characteristic radius W is assumed depth-independent and determines the lateral resolution. Next, the illuminating-beam spectrum in terms of wavenumbers in the axial direction is described by the amplitude profile $S(k_n)$ having $n=1...N$ spectral components k_n, summation of which forms an A-scan consisting of $q=1...N$ pixels with axial coordinates z_q. The distance $\delta k_n = | k_{n+1}-k_n |$ between the spectral components determines the total unambiguously imaged depth $H=\pi/\delta k$. If the characteristic spectral width of the spectral function $S(k_n)$ is Δk, the coherence length L_c determining the axial resolution in the resultant scans can be estimated as $L_c \sim \pi/\Delta k$ or equivalently in terms of the central wavelength λ_0 and spectral width $\Delta\lambda$, $L_c \sim \lambda_0^2/2\Delta\lambda$ (note that more accurate coefficient in the estimate for L_c depends on the exact form of the spectral function $S(k_n)$). Then for an A-scan corresponding to lateral coordinates (x_0,y_0) of the illuminating beam, the contribution of a scatterer with coordinates $\vec{r_s}=(x_s,y_s,z_s)$ to the received signal at the spectral component with the wavenumber k_n has the following form

$$B\left(\vec{r_s},x_0,y_0,k_n\right)=K_s\left(k_n\right)\times T(x_s-x_0,y_s-y_0)\times \\ \times\exp\left(-i\cdot 2k\cdot z_s\right), \quad (2)$$

where $K_s(k_n)$ is the scattering strength of the scatterer for the spectral component k_n, although often it may be sufficient to consider frequency-independent scattering strength. Now having the complex-valued amplitude of individual spectral components $B\left(\vec{r_s},k_n\right)$ from a single scatterer, the expression for the amplitude of q^{th} pixel corresponding to the depth $z=z_q$ in the A-scan with coordinates (x_0,y_0) can obtained by performing summation of contributions of all scatterers for all spectral components

$$A(x_0,y_0,z_q)=\sum_n\sum_s B\left(\vec{r_s},x_0,y_0,k_n\right)\exp(i\frac{2\pi n}{H}z_q). \quad (3)$$

The summation of spectral components on Eq. (3) is equivalent to performing the inverse discrete Fourier transform over the axial wave-vectors k_n, such that the expression for a pixelated A-scan can be represented as

$$A\left(x_0,y_0,z_q\right)=FFT^{-1}_{k_n}\left\{\sum_s B\left(\vec{r_s},x_0,y_0,k_n\right)\right\}. \quad (4)$$

Simulations of 2D B-scans and 3D volumes of OCT data is performed by scanning the illumination beam, which corresponds to variation in coordinates (x_0,y_0) of the illuminating beam in the model equations. It is clear from Eqs. (1) and (2) that the model readily describes how OCT-scan varies when scatterers gradually leave and enter the illuminating beam when its coordinates (x_0,y_0) or coordinates of $\vec{r_s}=(x_s,y_s,z_s)$ of the scatterers are varied. As mentioned above, if necessary, the depth dependence of the illuminating beam (for example exponential decay $\propto\exp(-\mu z)$ with the decay coefficient μ as in Ref. [39]) or acquisition noise at the receiving array can also be readily imitated by adding random complex-valued terms to spectral amplitudes (2) (as in Ref. [40]).

Expressions (1) – (4) can be evaluated very rapidly, because all signal amplitudes are given in a compact analytical form, so that only summation of contributions of all spectral harmonics and illuminated scatterers should be made numerically. Therefore, because of intrinsic ease of accounting for variations in coordinates of scatterers, the above presented Eqs. (1) – (4) represent a flexible and computationally very fast platform for simulations of evolution of OCT scans due to motion of scattering centers. In simulations related to OCT-based elastography (as in Refs. [38–41]), for which a couple of simulated B-scans usually was sufficient, the computational efficiency was useful, but not a critical condition. However, for modeling angiographic processing or diffusion phenomena, where large sequences of OCT-scans (in 2D and, moreover, 3D cases) are required, high computational efficiency of the used simulation method becomes critically important. In the following section we demonstrate how the above-presented model Eqs. (1) – (4) are applied for simulation of angiographic processing using the high-pass filtering principles suggested in Ref. [6, 17] and correlation processing discussed in Ref. [45].

3 Simulation of micro-vasculature visualization using the high-pass filtering principle

In this section we demonstrate the application of the above-formulated model for simulation of OCT-based visualization of microcirculation. There are somewhat different realizations of OCT-based label-free

angiography that are based on comparison of sequentially acquired OCT scans. The regions of "solid" tissue in the images correspond to (nearly) invariable parts of OCT scans, whereas the vessels with moving blood particles demonstrate local variability that can be singled out by special processing of the compared images. Different angiographic algorithms proposed during the last two decades use either phase information Doppler methods, or amplitude variability like in the speckle-variance-based methods (see, e.g., review Ref. [46]), or utilize mixed phase-amplitude processing. An important problem in all such method is the influence of masking living tissue motions (related to heart beats, breathing, etc.) that should be somehow eliminated using physical immobilization, special processing of the acquired images or combinations of hardware and software methods. In some methods a series of B-scans are acquired in one position and then a similar series is obtained in another position and so on, such that a 3D stack of OCT data is finally obtained [3].

There are also variants, in which the scanning is performed continuously, but with a significant overlap of neighboring scans. From the viewpoint of controlling the beam position, continuous scanning can be easier realized in comparison with step-wise jumps. This idea can be realized in somewhat different forms. One variant is acquiring dense B-scans with significantly overlapped A-scans (say, the inter-A-scan step is ~50 times smaller than the illuminating-beam diameter) as proposed in Ref. [17]. Then 3D volumetric data can be composed from a series of such dense B-scans. In another variant described in Ref. [6], B-scans have "normal" density of A-scans, but in the 3D-data volumes these B-scans are acquired with an appreciable overlap (say, the inter-B-scan step is 6–7 times smaller than the illuminating-beam diameter). Since the the inter-A-scan interval in the first variants is significantly smaller than inter-B-scan time interval in the second variant, the latter method can easier detect flows with lower velocity. However, by the same reason of higher sensitivity to displacements the inter-B-scan method is less tolerant to masking motions of living tissues. To reduce the magnitude of such motions, usually this method has to be used in contact mode [6].

Schematically this approach based on continuous scanning is shown in Fig. 2. It is clear that in the direction of overlapping, motionless scatterers in the "solid" tissue correspond to essentially elongated speckles with fairly slowly varying amplitude and phase, whereas the speckles corresponding to the places with moving scatterers (vessels with moving blood particles) demonstrate faster variability (and look as "short" speckles).

An example of a real OCT record illustrating these statements is shown in Fig. 3a for a single dense B-scan obtained with a horizontal step between subsequent positions of the illuminating beam ~1/50 of its diameter. It is clear that in the region of the vessel with moving blood particles, the horizontal size of speckles is much smaller than for the regions of "solid" tissue with almost motionless scatterers. As mentioned in Ref. [17], this difference manifests itself in the Fourier spectrum of such OCT-data obtained by applying Fourier transformation along the direction of A-scan overlapping. If the so-found spectrum is subjected to high-pass filtering, then in its inverse Fourier transform the regions of motionless scatterers can be eliminated, whereas the zones of vessels with moving blood particles can be retained (see detail in Ref. [17]). In a similar manner the microvasculature can be imaged for a series of B-scans that are overlapped along the direction orthogonal to the B-scan planes [6].

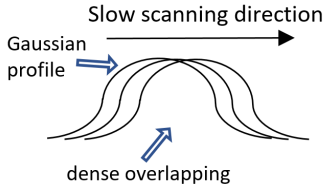


Fig. 2 Schematically shown slow scanning with partial self-overlapping of the illuminating beam.

Fig. 3 demonstrates that application of high-pass filtering to the initial dense structural scan the regions corresponding to the "solid" tissue with fairly slow horizontal variability of the speckles makes it possible to retain predominantly the zones corresponding to perfused vessels. It is important to point out that besides motions of particles in perfused vessels, for living tissues motions of other nature (related to heart beats, breathing, etc.) are typical, the velocities of particles due to these motions may be comparable or even exceed velocities of scatterers typical for microcirculation of blood. Fortunately, such motions are usually characterized by significantly larger scale of spatial inhomogeneity being closer to bulk translational motions, the axial component of which being strongly dominant in the masking signal. This axial component of masking bulk axial motions can be efficiently suppressed during the angiographic processing by determining and compensating the depth-averaged phase difference between neighboring A-scans caused large-scale bulk motions [17]. Such compensation weakly affects small-scale motions of blood particles in vessels and significantly improves the quality of microvasculature visualization. When obtaining the image of the vessel cross-section in Fig. 3a–2 (by filtering the initial structural scan in Fig. 3a–1), the above described procedures of bulk-motion compensation were applied.

The quality of microvasculature visualization using methods based on particle-motion contrast (not necessarily for high-pass filtering) strongly depends on the parameters used during obtaining the OCT scans, as well as during their processing. Optimization of these parameters is non-trivial and in a rather complex ways depends on the characteristics of the OCT system, regime of scanning, blood-flow velocities, vessel diameters, intensity of masking motions, noises, etc. Sufficiently precise control of such a broad variety of various parameters in real experimental conditions is challenging or may even be impossible. In this context the presented in the previous section method allows one to perform

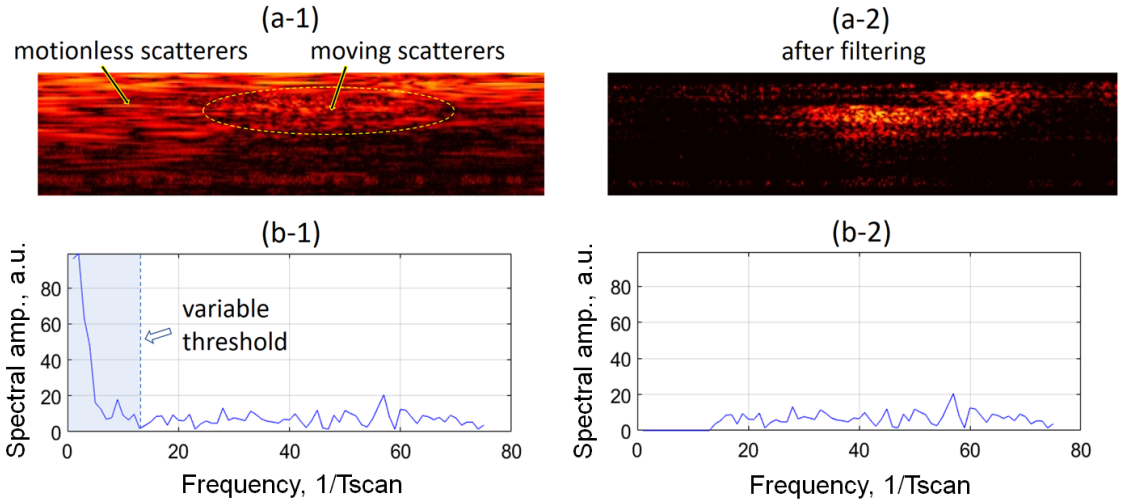


Fig. 3 Elucidation of the high-pass filtering principle of blood-flow visualization. Panel (a–1) is a real example of a dense B-scan with significant overlapping of A-scans along the B-scan plane. In this scan for the motionless tissue, speckles are pronouncedly elongated in the horizontal direction, whereas for the zones of blood flow, speckles are much shorter. This difference also manifests itself in the spatial spectrum found along the horizontal direction for this B-scan. The spectrum characterizing the variability of speckles in the direction of scanning for the middle depth of the scan (a–1) in presented in panel (b–1), where the most intense low-frequency components correspond to elongated speckles within the "solid" tissue. Panel (b–2) shows the spectrum after elimination of the low-frequency components and panel (a–2) shows the structural scan obtained by inverse Fourier transform applied to the spectrum after high-pass filtering. Total time T_{scan} of the analyzed scan determines the spectral resolution of the Fourier transform.

rapid, flexible and realistic numerical simulations of OCT scans with accounting for various types of motions and precise variation of a broad range of other parameters open unprecedented possibilities for testing and optimization of such processing methods.

Below we illustrate such possibilities of the described model by generating dense B-scans similar to real scans shown in Fig. 3a. In the simulated region a blood vessel with a Y-like bifurcation was modeled. It was possible to vary the vessel diameter, its orientation, velocity of scatterers inside the vessel, to change the velocity profile in the vessel cross section. Also masking bulk motions of various intensity were simulated by adding vertical displacements of entire vertical columns of scatters between subsequent A-scans (note that reception noises of arbitrary magnitude can readily be introduced as was demonstrated in Ref. [40] in the context of realization of mapping strains). This flexibility of the model allows one to estimate ultimate possibilities of the angiographic visualizations (minimal detectable diameter, minimal velocity) and to estimate maximal level of noise, and degree of A-scan overlapping, for which the visualization is feasible.

In Fig. 4 we illustrate the utilization of the models for assessing the role of masking bulk motions and efficiency of their compensation by correcting the depth-averaged phase shift between neighboring A-scans. In the simulation we imitated the parameters of OCT setup used in Ref. [17]. Namely, the optical wavelength in the tissue was $\lambda_0 = 1$ μm (corresponding to $\lambda_0 \sim 1.3$ μm in air), the spectral width of the illuminating beam was about 90 nm, the beam radius was 15 μm, the vertical size of the pixel was 8 μm in air (about 6 μm in the tissue with the refractive index ~1.3). The simulated image depth was 600 μm and horizontal size 150 μm with the horizontal step 1 μm between the subsequent A-scans. The signal-to-noise ratio was 23.5 dB in the upper part of the scans and depth decay similar to that for real scans shown in Fig. 3 was introduced. The vessel width before bifurcation was 15 μm and 7.5 μm after bifurcation. The velocity of blood flows was chosen to be 1 mm/s. The simulations were performed for three levels of bulk noises (indicated in the caption). For the upper row, the amplitudes of the inter-A-scan displacements are smaller than $\lambda_0/4$ for all A-scans, so that the phase shifts induced by the masking bulk motions are unambiguously related to displacements. Therefore, in this case the masking displacement-related noises well-visible for scans in the middle column in Fig. 4 can be nearly perfectly compensated. This is clear from panel (a–3) in which the motion-related noises are very well suppressed. For rows (b) and (c), the inter-A-scan bulk motions mostly have supra-wavelength amplitudes, so that the corresponding phase variations are wrapped and are not unambiguously related to the displacements. Nevertheless, even in these cases, the application of the compensation based on comparison of phases of neighboring A-scans significantly improves the quality of visualizations of the vessels (see the right column in Fig. 4).

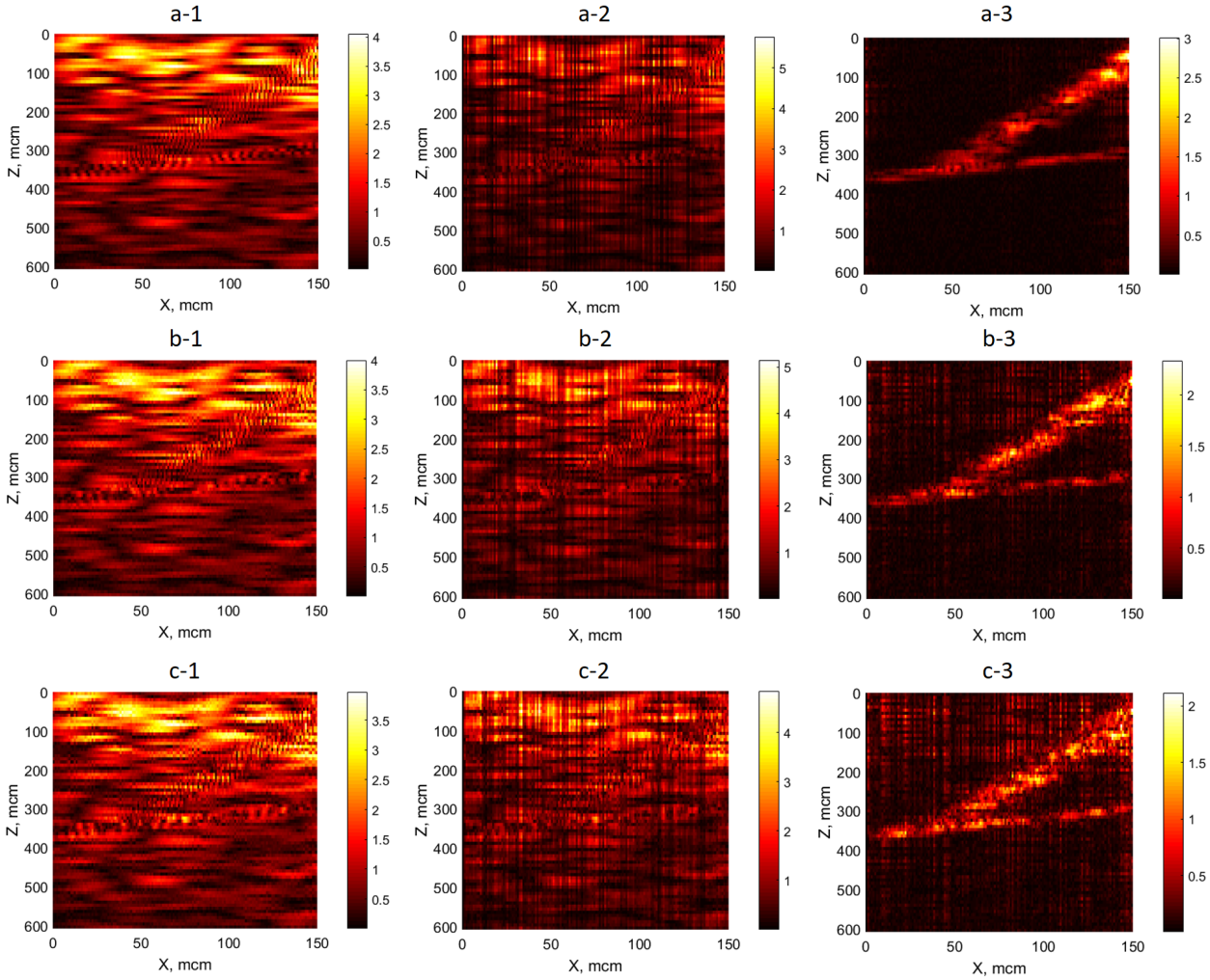


Fig. 4 Examples of simulations performed in the context of the development of OCT-based angiography. Left column shows initial densely recorded scans, middle column is for filtered scans without correction of the bulk motion, and (right column) with correction of the bulk motion. Rows (a) through (c) correspond to inter-A-scan bulk motions with a Gaussian distribution of the amplitude with various standard deviations (STD). Upper panels (a1–3) correspond to translational displacements with STD = $\lambda_0/10$, for which the amplitudes of the displacements are under $\lambda_0/4$ and the inter-A-scam phase difference can be found unambiguously. Panels (b1) – (b3) are for significantly greater displacements with STD = λ_0 and (c1) – (c3) are for STD = $1.5\lambda_0$.

4 Model application for simulations of OCT-signal decorrelation in the presence of regular and random scatterer motions

As mentioned above, for perfused vessels, the main contribution to the variability of received OCT signal and, correspondingly, to its temporal decorrelation belongs to motion of erythrocytes. Among other methods applied for detection of perfused microvasculature studies of temporal decorrelation of OCT signals attracts significant attention [47, 48]. Although erythrocytes are discrete scatterers that are not yet resolved in conventional OCT images, their size exceeds the optical wavelength. Consequently, even in the absence of translational flows, rotational motions of erythrocytes may give an appreciable contribution to the OCT-signal decorrelation. Real experiments do not allow one to selectively study contributions of transversal and rotational motion of finite-size scatteres, whereas in simulations such studies can readily be implemented. To this end, we made the following modification of the scatterer model as shown in Fig. 5a. Fig. 5a schematically shows the cross section of an erythrocyte with an approximately dumbbell shape. Thus a reasonable simplified approximation of scattering properties of such an object can be a dumbbell made of a pair of localized scattering centers with a distance D between the centers corresponding to the erythrocyte diameter. In the below presented simulations we chose $D = 6$ μm (which is close to the average diameter of human erythrocytes). The central wavelength is supposed to be $\lambda_0 = 1$ μm (which is close to the wavelength in the tissue for widely used OCT systems based on the sources with the wavelength 1.3 μm in vacuum). Using such a model for generation of 2D B-scans we characterize the position of the dumbbell center by coordinate $\vec{r}_c = (x_c, z_c)$, whereas

the rotation around this center is characterized by angle as shown in Fig. 5b.

Here, we consider three basic types of motions of erythrocytes in vessels: (i) regular translational flow, (ii) translational Brownian motion and (iii) rotational Brownian motion. Let us describe in more detail how these types of motions are characterized in the model. In real experiments it is impossible to realize these motion types in pure form, but can be readily made in simulation.

(i) For the translational flow-type motion, we assume that the erythrocytes move without changing their orientation ($\varphi = const.$) with an invariable-in-time velocity. Then for the neighboring A-scans with numbers n and $n+1$ the scatterer coordinates are related as $\vec{r}(n+1) = \vec{r}(n) + \vec{V} \cdot \Delta t$, where $\vec{V}$ is the flow velocity and Δt is the time interval between A-scans.

(ii) For the translational Brownian motion, the orientation angle for the scatterers is also constant ($\varphi = const.$), whereas the coordinates of the centers vary from one A-scan to another one in random steps, $\vec{r}(n+1) = \vec{r}(n) + \Delta\vec{r}_n$, where the components of the incremental vector $\Delta\vec{r}_n$ have a Gaussian probability distribution for displacements along coordinates x and z

$$\rho(\Delta x) = \frac{1}{\sigma_{\Delta x}\sqrt{2\pi}} \exp\left(-\frac{\Delta x^2}{2\sigma_{\Delta x}^2}\right); \quad \rho(\Delta z) = \frac{1}{\sigma_{\Delta z}\sqrt{2\pi}} \exp\left(-\frac{\Delta z^2}{2\sigma_{\Delta z}^2}\right), \tag{5}$$

where the standard deviations were supposed equal, $\sigma_{\Delta x} = \sigma_{\Delta z}$.

(iii) For the Brownian rotational motion, coordinates of the scattering-particle centers remain constant, whereas the orientation angle randomly varies $\varphi(n+1) = \varphi(n) + \Delta\varphi$, where the rotation-angle increment has a Gaussian distribution with a standard deviation $\sigma_{\Delta\varphi}$

$$\rho(\Delta\varphi) = \frac{1}{\sigma_{\Delta\varphi}\sqrt{2\pi}} \exp\left(-\frac{\Delta\varphi^2}{2\sigma_{\Delta\varphi}^2}\right). \tag{6}$$

In all cases the initial position and orientations of the scattering particles are random.

For studying decorrelation of OCT scans due to such motions of scatteres, it was sufficient to form sequences of B-scans (for the below presented examples, scans 255 × 80 pixels in size were used). The scatterers with random initial coordinates were distributed uniformly over the simulated scans and experienced either one of the above-described three types of motions. The cross-correlation coefficients were calculated for complex-valued amplitudes b_{ij} of pixels in the initial scan for $t = 0$ and subsequently simulated B-scans for $t = t_n$ using the following expression:

$$C(t_n) = \frac{\sum_{i,j} b_{ij}(0) b_{ij}^*(t_n)}{\left(\sum_{i,j} |b_{ij}(0)|^2 \sum_{i,j} |b_{ij}(t_n)|^2\right)^{1/2}} \tag{7}$$

According to previous studies, exponential dependences of the form $|C(t)| = \exp(-at^q)$ could be expected, where parameter q depends of the particular character of the scatterer motions [45]. It is clear that if we plot the logarithm $\ln|C(t)|$ against t^q, the assumed exponential dependence $|C(t)| = \exp(-at^q)$ should correspond to a straight line, which can be visually clearly seen for the correctly chosen parameter q.

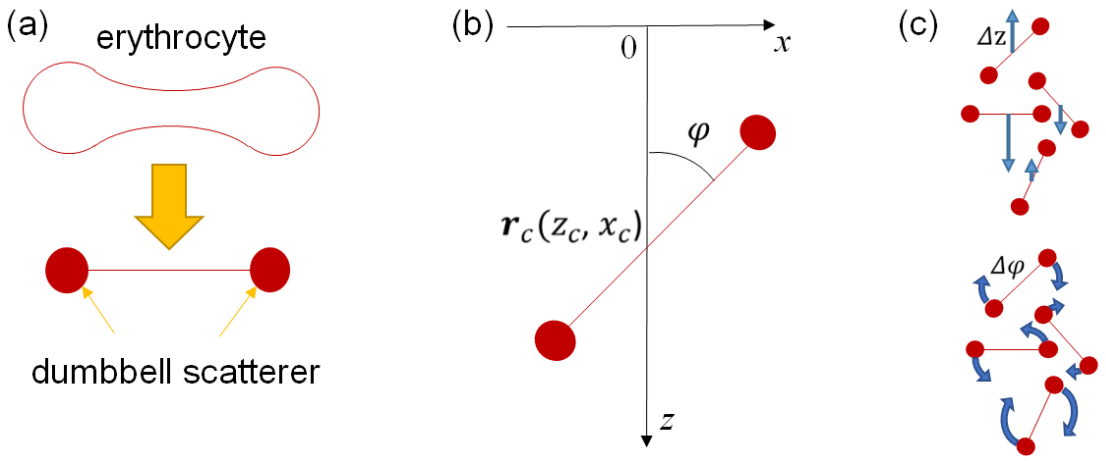


Fig. 5 The model of erythrocytes in the form of dumbbell scattering elements (a), elucidation of the parameters describing their positions and orientations (b) and schematically shown translational and rotational motions of dumbbell scatterers.

The results of the corresponding simulations for the above-mentioned three characteristic types of scatterer motions are presented in Fig. 6. The horizontal axes in Fig. 6 represent t^q rather than t, so that even if $\ln|C(t)|)$ varies nonlinearly with time for $q \neq 1$, the time is explicitly indicated in the time-axis labels. The dependences found in the performed simulations for regular translational flow demonstrated the exponent $q = 2$ (Fig. 6a) and $q = 1$ for translational Brownian motion (Fig. 6b), which agrees with the previously known results based on analytical considerations of these motion types [45, 49]. Concerning rotational Brownian motion, for which analytical consideration is more difficult, the performed simulations demonstrate different regimes for the cross-correlation decay in the beginning and at larger times. Fig. 6c shows that initially (within the interval below ~25 ms) the decay law corresponds to $q = 1$ like for translational Brownian motion, whereas for larger times, the transition to the scaling with $q = 1/2$ is seen within a fairly broad time interval (Fig. 6d). As far as we know, the decay law of the form $|C(t)| = \exp(-at^{1/2})$ earlier has been found for speckles when the contribution of multiple scattering was significant. However, our simulations demonstrate that such functional behavior can also occur for speckle decorrelation in the case of single scattering for Brownian rotation.

The fact of initial (for time below ~25 ms) functionally similar behavior $|\propto \exp(-at^{1/2})$ of speckle decorrelation due to Brownian rotation and translational Brownian motion may be qualitatively understood as follows. For randomly oriented dumbbell-like scatterers, there is a portion of approximately horizontally-oriented ones that produce in-phase scattered signals. This portion of initially in-phase scattering horizontally-oriented elements gives a dominant contribution to decorrelation. For this portion of dumbbell elements and sufficiently small deviation $\Delta\Phi << 1$ from the initial approximately horizontal orientation, the difference of optical paths for the signals scatterers by the left and right scatterers is linearly proportional to the rotation angle as $2D\sin(\Delta\Phi) \sim 2D\Delta\Phi$, where the factor 2 is due to forward-backward propagation for the incident and back-scattered waves. Quantity $<(2D\Delta\Phi)^2> \propto t$ accumulates in random steps obeying a Gaussian probability law Eq. (6). This is similar to translational Brownian motion, for which the differences in the optical paths ΔZ of interfering scattered fields also grows with a Gaussian probability, such that $<\Delta Z^2> \propto t$ (see Eq.(5)).

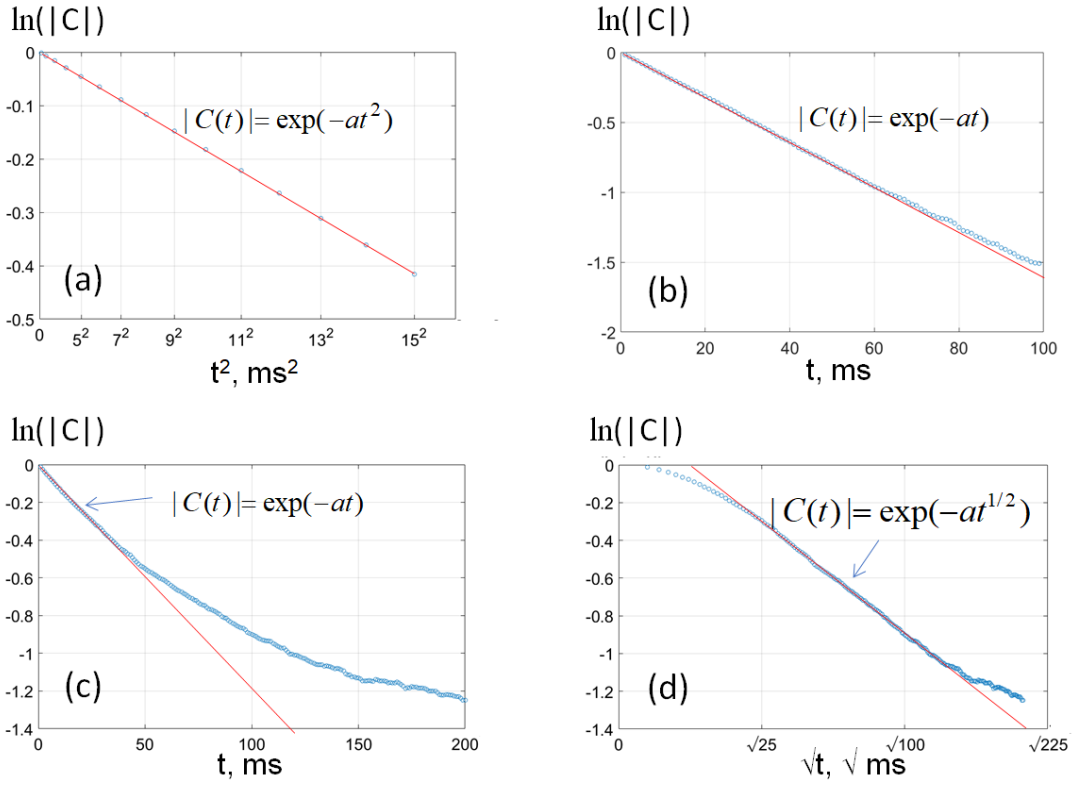


Fig. 6 Result of numerical simulation of the decorrelation laws for the translational flow (a), translational Brownian motion (b) and rotational Brownian motion (panel (c) shows the linearized representation for $|C(t)| = \exp(-at)$ corresponding to initial decorrelation at small times and linearized law $|C(t)| = \exp(-at^{1/2})$ for larger times). Dots are the simulation results and solid straight lines are guides for the eye showing the corresponding linearized representations of the decay laws.

However, such functional similarity for translational and rotational Brownian motions holds only for sufficiently small times, when the rotation-induced difference in the optical paths $\sqrt{(2D\Delta\Phi)^2}$ remains noticeably smaller than $\lambda_0/4$. Sufficiently below this value, the factor $\sin(2Dk_0\Delta\Phi)$ determining the interference result can be linearly approximated as $2Dk_0\Delta\Phi$. With accumulation of the rotation angle the factor $\sin(2Dk_0\Delta\Phi)$ grows slower than the initial linear approximation, so that the initial correlation-coefficient decrease $\propto \exp(-at)$ should demonstrate a slower decrease rate. The intermediate dependence $\propto \exp(-at^{1/2})$ visible in Fig. 6d agrees with this expected transition to a slower law, although for predicting its functional form, the above-presented arguments are not sufficient. However, they allow one to estimate the characteristic angle $\Delta\Phi_{char}$ of this transition as $\Delta\Phi_{char} = \lambda_0/8D \sim 0.02$. This simple estimate fairly well agrees with the mean-square rotation angle $\sqrt{<\Delta\Phi^2>} \propto \sigma_{\Delta\varphi}\sqrt{t} \approx 0.025$. This value was found in the simulations for the time point $t \sim 25$ ms, around which the transition from $\propto \exp(-at)$ to $\propto \exp(-at^{1/2})$ is observed in Fig. 6d. It has also been numerically verified that if parameters D, k_0 and $\sigma_{\Delta\varphi}$ are varied in such a way that the factor $Dk_0\sigma_{\Delta\varphi} = const$, the transition time visible in Fig. 6d also remains invariable. This numerical result confirms the expectation that the characteristic time of the transition is determined by the product $Dk_0\sigma_{\Delta\varphi} = const$.

Concluding this section it can be mentioned that the time dependence of the correlation function for translational regular flows and Brownian motion of spherical particles was studied analytically in Ref. [49]. Such analysis predicts the decay law for the absolute value of the correlation coefficient of the form

$$|C_s(t)| = \exp(-\frac{t}{\tau_b})\exp(-\frac{t^2}{\tau_t^2}), \quad (8)$$

where τ_b is the characteristic decorrelation time due to Brownian motion, and τ_t is the decorrelation time due to translational flow. It is clear that these known cases well agree with the above-presented numerical results, which confirms the correctness of the formulated numerical model. The influence of random rotations of erythrocytes on the decorrelation of speckles was touched in Ref. [50]. Analytical investigation was not performed in that works, and experimentally the decay law of the type $|C(t)| = \exp(-at)$ was observed. This observation agrees with the decay law for sufficiently small times revealed in our simulations as shown in Fig. 6c.

5 Conclusions

Here we presented a computationally very efficient and fairly realistic model of OCT-scan formation in spectral-domain optical coherence tomography. The described variant of the model is based on previously proposed variants [32–34]. The described variant represents a compromise between the simplest version [32] based on cylindrical illuminating beams with uniform profile and rigorous analysis of OCT systems with fairly focused Gaussian beams [33, 34]. The considered compromise variant uses beams with a Gaussian amplitude profile and uniform phase distribution over the cross section, which enables computationally efficient and reasonably realistic simulations of OCT-scan formation for weakly focused Gaussian beams, which is validated by comparison with the rigorously described Gaussian beam in study [33].

Similarly to the previous versions [32–34] and many other popular models (e.g. Ref. [30]), the present model is based on the approximation of discrete scatterers and ballistic character of scattering. An important advantage of this model demonstrated above is the intrinsic ease in accounting for arbitrary scatterer motions, which allows one to computationally efficiently generate large sequences of OCT scans for gradually varying configurations of scatterers. This makes the described simulation platform very convenient for studies related to the development of angiographic processing of OCT scans for visualization of microcirculation of blood, as well as for studies of decorrelation of speckle patterns in OCT scans due to random (Brownian type) motions of scatterers as was demonstrated in the previous sections. To the best of our knowledge, such numerical simulations of large series of OCT scans in the presence of various types of motion of scatterers have not been demonstrated before. The model is also very useful for simulating images of deformed tissues in the context of the development of Optical Coherence Elastography [37–40]. If necessary, accounting for non-ideally ballistic propagation of the optical waves can be added as discussed in Ref. [36].

Disclosures

All authors declare that there is no conflict of interests in this paper.

Acknowledgements

The development of the basic form of the OCT-signal formation model was supported by RFBR (grant No 19-02-00645) and the model adaptation and utilization for simulating OCT-based angiography was supported by RSF grant No 17-72-20249.

References

1. V. Yu. Zaitsev, V. M. Gelikonov, L. A. Matveev, G. V. Gelikonov, A. L. Matveyev, P. A. Shilyagin, and I. A. Vitkin, "Recent trends in multimodal optical coherence tomography. I. Polarization-sensitive OCT and conventional approaches to OCT elastography," Radiophysics and Quantum Electronics 57(1), 52–66 (2014).
2. J. F. De Boer, C. K. Hitzenberger, and Y. Yasuno, "Polarization sensitive optical coherence tomography–a review," Biomedical Optics Express 8(3), 1838–1873 (2017).
3. A. Mariampillai, B. A. Standish, E. H. Moriyama, M. Khurana, N. R. Munce, M. K. K. Leung, J. Jiang, A. Cable, B. C. Wilson, I. A. Vitkin, and V. X. D. Yang, "Speckle variance detection of microvasculature using swept-source optical coherence tomography," Optics Letters 33(13), 1530–1532 (2008).
4. E. Jonathan, J. Enfield, and M. J. Leahy, "Correlation mapping method for generating microcirculation morphology from optical coherence tomography (OCT) intensity images," Journal of biophotonics 4(9), 583–587 (2011).
5. C. L. Chen, R. K. Wang, "Optical coherence tomography based angiography," Biomedical Optics Express 8(2), 1056–1082 (2017).
6. A. Moiseev, S. Ksenofontov, M. Sirotkina, E. Kiseleva, M. Gorozhantseva, N. Shakhova, L. Matveev, V. Zaitsev, A. Matveyev, E. Zagaynova, V. Gelikonov, N. Gladkova, A. Vitkin, and G. Gelikonov, "Optical coherence tomography-based angiography device with real-time angiography B-scans visualization and hand-held probe for everyday clinical use," Journal of Biophotonics 11, e201700292 (2018).
7. A. V. Maslennikova, M. A. Sirotkina, A. A. Moiseev, E. S. Finagina, S. Y. Ksenofontov, G. V. Gelikonov, L. A. Matveev, E. B. Kiseleva, V. Y. Zaitsev, E. V. Zagaynova, F. I. Feldchtein, N. D. Gladkova, and A. Vitkin, "In-vivo longitudinal imaging of microvascular changes in irradiated oral mucosa of radiotherapy cancer patients using optical coherence tomography," Scientific Reports 7(1), 1–10 (2017).
8. E. V. Gubarkova, F. I. Feldchtein, E. V. Zagaynova, S. V. Gamayunov, M. A. Sirotkina, E. S. Sedova, S. S. Kuznetsov, A. A. Moiseev, L. A. Matveev, V. Y. Zaitsev, D. A. Karashtin, G. V. Gelikonov, L. Pires, A. Vitkin, and N. D. Gladkova, "Optical coherence angiography for pre-treatment assessment and treatment monitoring following photodynamic therapy: a basal cell carcinoma patient study," Scientific Reports 9(1), 1–13 (2019).
9. B. Blackburn, S. Gu, M. R. Ford, V. S. De Stefano, M. Jenkins, W. J. Dupps, and A. Rollins, "Phase-Decorrelation OCT for Noncontact Measurement of Biomechanical Effects of Corneal Crosslinking," Investigative Ophthalmology & Visual Science 59(9), 745 (2018).
10. G. L. Monroy, P. Pande, R. L. Shelton, R. M. Nolan, D. R. Spillman Jr., R. G. Porter, M. A. Novak, and S. A. Boppart, "Non-invasive optical assessment of viscosity of middle ear effusions in otitis media," Journal of Biophotonics 10(3), 394403 (2017).
11. K. V. Larin, D. D. Sampson, "Optical coherence elastography–OCT at work in tissue biomechanics," Biomedical Optics Express 8(2), 1172–1202 (2017).
12. V. Y. Zaitsev, A. L. Matveyev, L. A. Matveev, A. A. Sovetsky, M. S. Hepburn, A. Mowla, and B. F. Kennedy, "Strain and elasticity imaging in compression optical coherence elastography: The two-decade perspective and recent advances," Journal of Biophotonics 14(2), e202000257 (2021).
13. A. A. Plekhanov, M. A. Sirotkina, A. A. Sovetsky, E. V. Gubarkova, S. S. Kuznetsov, A. L. Matveyev, L. A. Matveev, E. V. Zagaynova, N. D. Gladkova, and V. Y. Zaitsev, "Histological validation of in vivo assessment of cancer tissue inhomogeneity and automated morphological segmentation enabled by Optical Coherence Elastography," Scientific Reports 10(1), 1–16 (2020).
14. E. V. Gubarkova, A. A. Sovetsky, V. Yu. Zaitsev, A. L. Matveyev, D. A. Vorontsov, M. A. Sirotkina, L. A. Matveev, A. A. Plekhanov, N. P. Pavlova, S. S. Kuznetsov, A. Yu. Vorontsov, E. V. Zagaynova, and N. D. Gladkova, "OCT-elastography-based optical biopsy for breast cancer delineation and express assessment of morphological/molecular subtypes," Biomedical Optics Express 10(5), 2244–2263 (2019).
15. M. A. Sirotkina, E. V. Gubarkova, A. A. Plekhanov, A. A. Sovetsky, V. V. Elagin, A. L. Matveyev, L. A. Matveev, S. S. Kuznetsov, E. V. Zagaynova, N. D. Gladkova, and V. Y. Zaitsev, "In vivo assessment of functional and morphological alterations in tumors under treatment using OCT-angiography combined with OCT-elastography," Biomedical Optics Express 11(3), 1365–1382 (2020).
16. E. V. Gubarkova, E. B. Kiseleva, M. A. Sirotkina, D. A. Vorontsov, K. A. Achkasova, S. S. Kuznetsov, K. S. Yashin, A. L. Matveyev, A. A. Sovetsky, L. A. Matveev, A. A. Plekhanov, A. Y. Vorontsov, V. Y. Zaitsev, and N. D. Gladkova, "Diagnostic Accuracy of Cross-Polarization OCT and OCT-Elastography for Differentiation of Breast Cancer Subtypes: Comparative Study," Diagnostics 10(12), 994 (2020).
17. L. A. Matveev, V. Yu. Zaitsev, G. V. Gelikonov, A. L. Matveyev, A. A. Moiseev, S. Yu. Ksenofontov, V. M. Gelikonov, M. A. Sirotkina, N. D. Gladkova, V. Demidov, and A. Vitkin, "Hybrid M-mode-like OCT imaging of three-dimensional microvasculature in vivo using reference-free processing of complex valued B-scans," Optics Letters 40(7), 1472–1475 (2015).
18. A. Weatherbee, M. Sugita, K. Bizheva, I. Popov, and A. Vitkin, "Probability density function formalism for optical coherence tomography signal analysis: a controlled phantom study," Optics Letters 41(12), 2727–2730 (2016).

19. H.-J. Lee, N. M. Samiudin, T. G. Lee, I. Doh, and S.-W. Lee, "Retina phantom for the evaluation of optical coherence tomography angiography based on microfluidic channels," Biomedical Optics Express 10(11), 5535–5548 (2019).
20. G. Yao, L. V. Wang, "Monte Carlo simulation of an optical coherence tomography signal in homogeneous turbid media," Physics in Medicine & Biology 44(9), 2307 (1999).
21. M. Kirillin, I. Meglinski, V. Kuzmin, E. Sergeeva, and R. Myllylä, "Simulation of optical coherence tomography images by Monte Carlo modeling based on polarization vector approach," Optics Express 18(21), 21714–21724 (2010).
22. A. Doronin, I. Meglinski, "Online object oriented Monte Carlo computational tool for the needs of biomedical optics," Biomedical Optics Express 2(9), 2461–2469 (2011).
23. A. D. Buligin, Y. V. Kistenev, I. Meglinski, E. A. Danilkin, and D. A. Vrazhnov, "Imitation of ultra-sharp light focusing within turbid tissue-like scattering medium by using time-independent Helmholtz equation and method Monte Carlo," SPIE Proceedings 11582, 115821N (2020).
24. A. D. Bulygin, D. A. Vrazhnov, E. S. Sim, I. Meglinski, and Y. V. Kistenev, "Imitation of optical coherence tomography images by wave Monte Carlo-based approach implemented with the Leontovich–Fock equation," Optical Engineering 59(6), 061626 (2020).
25. A. Y. Potlov, S. V. Frolov, and S. G. Proskurin, "Numerical Simulation of Photon Migration in Homogeneous and Inhomogeneous Cylindrical Phantoms," Optics and Spectroscopy 128(6), 835–842 (2020).
26. J.M. Schmitt, A. Knüttel, "Model of optical coherence tomography of heterogeneous tissue," Journal of the Optical Society of America A 14(6), 1231–1242 (1997).
27. L. Chin, A. Curatolo, B. F. Kennedy, B. J. Doyle, P. R. T. Munro, R. A. McLaughlin, and D. D. Sampson, "Analysis of image formation in optical coherence elastography using a multiphysics approach," Biomedical Optics Express 5(9), 2913–2930 (2014).
28. P. R. Munro, "Three-dimensional full wave model of image formation in optical coherence tomography," Optics Express 24(23), 27016–27031 (2016).
29. P. R. Munro, A. Curatolo and D. D. Sampson, "Full wave model of image formation in optical coherence tomography applicable to general samples," Optics Express 23(3), 2541–2556 (2015).
30. M. Almasian, T. G. van Leeuwen, and D. J. Faber, "OCT Amplitude and Speckle Statistics of Discrete Random Media," Scientific Reports 7, 14873 (2017).
31. J. Kalkman, "Fourier-Domain Optical Coherence Tomography Signal Analysis and Numerical Modeling," International Journal of Optics 2017, 9586067 (2017).
32. V. Y. Zaitsev, L. A. Matveev, A. L. Matveyev, G. V. Gelikonov, and V. M. Gelikonov, "A model for simulating speckle-pattern evolution based on close to reality procedures used in spectral-domain OCT," Laser Physics Letters 11(10), 105601 (2014).
33. A. L. Matveyev, L. A. Matveev, A. A. Moiseev, A. A. Sovetsky, G. V. Gelikonov, and V. Y. Zaitsev, "Semianalytical full-wave model for simulations of scans in optical coherence tomography with accounting for beam focusing and the motion of scatterers," Laser Physics Letters 16(8), 085601 (2019).
34. A. L. Matveyev, L. A Matveev, A. A. Moiseev, A. A. Sovetsky, G. V. Gelikonov, and V. Y. Zaitsev, "Computationally efficient model of OCT scan formation by focused beams and its usage to demonstrate a novel principle of OCT-angiography," Laser Physics Letters 17(11), 115604 (2020).
35. A. Abdurashitov, V. Tuchin, "A robust model of an OCT signal in a spectral domain," Laser Physics Letters 15(8), 086201 (2018).
36. X. Cheng, Y. Li, J. Mertz, S. Sakadžić, A. Devor, D. A. Boas, and L. Tian, "Development of a beam propagation method to simulate the point spread function degradation in scattering media," Optics Letters 44(20), 4989–4992 (2019).
37. V. Y. Zaitsev, A. L. Matveyev, L. A. Matveev, G. V. Gelikonov, V. M. Gelikonov, and A. Vitkin, "Deformation induced speckle-pattern evolution and feasibility of correlational speckle tracking in optical coherence elastography," Journal of Biomedical Optics 20(7), 075006 (2015).
38. V. Y. Zaitsev, A. L. Matveyev, L. A. Matveev, G. V. Gelikonov, E. V. Gubarkova, N. D. Gladkova, and A. Vitkin, "Hybrid method of strain estimation in optical coherence elastography using combined sub-wavelength phase measurements and supra-pixel displacement tracking," Journal of Biophotonics 9(5), 499–509 (2016).
39. V. Y. Zaitsev, A. L. Matveyev, L. A. Matveev, G. V. Gelikonov, A. A. Sovetsky, and A. Vitkin, "Optimized phase gradient measurements and phase-amplitude interplay in optical coherence elastography," Journal of Biomedical Optics 21(11), 116005 (2016).
40. A. L. Matveyev, L. A. Matveev, A. A. Sovetsky, G. V. Gelikonov, A. A. Moiseev, and V. Y. Zaitsev, "Vector method for strain estimation in phase-sensitive optical coherence elastography," Laser Physics Letters 15(6), 065603 (2018).
41. V. Y. Zaitsev, A. L. Matveyev, L. A. Matveev, E. V. Gubarkova, A. A. Sovetsky, M. A. Sirotkina, G. V. Gelikonov, E. V. Zagaynova, N. D. Gladkova, and A. Vitkin, "Practical obstacles and their mitigation strategies in compressional optical coherence elastography of biological tissues," Journal of Innovative Optical Health Sciences 10(06), 1742006 (2017).

42. V. Y. Zaitsev, A. L. Matveyev, L. A. Matveev, G. V. Gelikonov, A. I. Omelchenko, D. V. Shabanov, O. I. Baum, V. M. Svistushkin, and E. N. Sobol, "Optical coherence tomography for visualizing transient strains and measuring large deformations in laser-induced tissue reshaping," Laser Physics Letters 13(11), 115603 (2016).
43. V. Y. Zaitsev, A. L. Matveyev, L. A. Matveev, G. V. Gelikonov, A. I. Omelchenko, O. I. Baum, S. E. Avetisov, A. V. Bolshunov, V. I. Siplivy, D. V. Shabanov, A. Vitkin, and E. N. Sobol, "Optical coherence elastography for strain dynamics measurements in laser correction of cornea shape," Journal of Biophotonics 10(11), 1450–1463 (2017).
44. V. Y. Zaitsev, A. L. Matveyev, L. A. Matveev, G. V. Gelikonov, O. I. Baum, A. I. Omelchenko, D. V. Shabanov, A. A. Sovetsky, A. V. Yuzhakov, A. A. Fedorov, V. I. Siplivy, A. V. Bolshunov, and E. N. Sobol, "Revealing structural modifications in thermomechanical reshaping of collagenous tissues using optical coherence elastography," Journal of Biophotonics 12(3), e201800250 (2019).
45. D. D. Postnov, J. Tang, S. E. Erdener, K. Kılıç, and D. A. Boas, "Dynamic light scattering imaging," Science Advances 6(45), eabc4628 (2020).
46. V. Y. Zaitsev, I. A. Vitkin, L. A. Matveev, V. M. Gelikonov, A. L. Matveyev, and G. V. Gelikonov, "Recent trends in multimodal optical coherence tomography. II. The correlation-stability approach in OCT elastography and methods for visualization of microcirculation," Radiophysics and Quantum Electronics 57(3), 210–225 (2014).
47. N. Uribe-Patarroyo, M. Villiger, and B. E. Bouma, "Quantitative technique for robust and noise-tolerant speed measurements based on speckle decorrelation in optical coherence tomography," Optics Express 22(20), 24411–24429 (2014).
48. Y. Jia, O. Tan, J. Tokayer, B. Potsaid, Y. Wang, J. J. Liu, M. F. Kraus, H. Subhash, J. G. Fujimoto, J. Hornegger, and D. Huang, "Split-spectrum amplitude-decorrelation angiography with optical coherence tomography," Optics Express 20(4), 4710–4725 (2012).
49. I. Popov, A. S. Weatherbee, and I. A. Vitkin, "Dynamic light scattering arising from flowing Brownian particles: analytical model in optical coherence tomography conditions," Journal of Biomedical Optics 19(12), 127004 (2014).
50. H. Ullah, A. Mariampillai, M. Ikram, and I. A. Vitkin, "Can temporal analysis of optical coherence tomography statistics report on dextrorotatory-glucose levels in blood?" Laser Physics 21(11), 1962–1971 (2011).

Changes in the Structure of the Benzylpenicillin Sodium Salt Molecule under the Pulsed Magnetic Field

Natalia A. Rodenko[1,2*], Valentina A. Zhukova[1], Tatyana I. Vasilyeva[1], Vladimir A. Glushchenkov[1,2], and Irina A. Belyaeva[1,2]

[1] Samara National Research University, 34 Moskovskoe shosse, Samara 443086, Russia

[2] Samara Federal Research Centre of the Russian Academy of Sciences, 3A Studencheskiy pereulok, Samara 443001, Russia

*** e-mail:** t.rodenko@mail.ru

Abstract. The study aims at the Fourier spectra of an antibiotic exposed to a high-intensity pulsed magnetic field. The applied frequency was f = 40 kHz, with a number of pulses n = 1, at intensities of the pulsed magnetic field H = 0.09 × 10^6 A/m, H = 0.50 × 10^6 A/m, H = 0.82 × 10^6 A/m. It was assumed that under the conditions of the pulsed magnetic field there might be a change in the structure of the drug molecule. The research has revealed that an increase in the pulsed magnetic field power leads first to a decrease in the intensity of the band in the Fourier spectrum, and then to its increase. In addition, changes were recorded in the amide group of benzylpenicillin sodium salt molecules depending on the intensity of the pulsed magnetic field applied to the antibiotic. © 2021 Journal of Biomedical Photonics & Engineering.

Keywords: antibiotic; Fourier spectroscopy; magnetic field intensity; biological activity.

Paper #3387 received 15 Dec 2020; revised manuscript received 31 Jan 2021; accepted for publication 18 Mar 2021; published online 31 Mar 2021. doi: 10.18287/JBPE21.07.010305.

1 Introduction

Currently, the question of the effectiveness of antibiotics has become a matter of great urgency. As a rule, antibiotics are used in the form of solutions, which results in a complex water-antibiotic-biosystem. Here, the problem of the interaction of a water molecule with a solid (powdered) antibiotic comes to the fore. In Ref. [1], it was noted that antibiotics in the form of solid samples (powders) are stable during storage, while those in the form of aqueous solutions quickly lose their biological activity. Therefore, it is important to find out the reason for the increase in the antibacterial activity of the benzylpenicillin sodium salt after being exposed to the pulsed magnetic field (PMF). The structure of a benzylpenicillin molecule (Fig. 1) demonstrates such characteristic features of penicillin antibiotics as the presence of a β–lactam ring, an amide group, and a thiazole cycle.

In Ref. [2], the potential of benzylpenicillin was calculated as an index of the reactivity of the antibiotic. It was shown that during the transition from a neutral penicillin molecule to its anion, the dipole moment increases from 4.7 D to 18.2 D, and the benzylpenicillin anion molecule takes on a complex semispherical spatial structure. The authors showed that in this case, the carbonyl groups are located on the outer side.

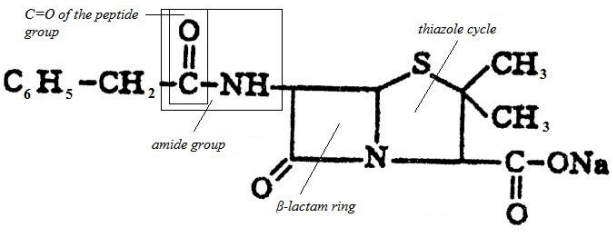


Fig. 1 Structural formula of benzylpenicillin sodium salt.

The authors of study [3] used quantum-chemical calculations to study the interaction of solid samples of benzylpenicillin with water and determined the location of water molecules during the formation of hydrate structures of the antibiotic. In this case, a three-dimensional grid of hydrogen bonds is formed, which includes all the functional groups of the antibiotic.

Jason Potticary et. al. [4] crystallized coronene (polyaromatic hydrocarbon) into another polymorph using the method of growing crystals under the conditions of the magnetic field action. Crystals, grown in a magnetic field with an induction of 1 T, differ in their appearance from crystals grown in a zero field, and retain their structure under environmental conditions. The researchers found the new form to be the most stable at low temperatures. As a result of the new supramolecular configuration, significant changes in the electronic, optical and mechanical properties were noted.

In another similar work, polymorphism during the crystallization of drugs by a magnetic field was investigated (Project №736899, UK, the Netherlands, Ireland). The European researchers have already established that it is possible to synthesize specific polymorphs of pharmaceutical substances, such as carbamazepine, indomethacin, and paracetamol. They found out [5] that concretive crystalline forms could exhibit unique properties that may not be shown by other forms of the same substance.

The researchers of the Kalinin Medical Institute [6] made an attempt to trace the action of the constant magnetic field on barbamil (sleeping substance). Three times, at different times of the year, the experimental batch of mice received a sleeping substance that had been previously exposed to a constant magnetic field. It was observed that under the influence of the "magnetized" sleeping pill the mice slept longer than the animals from the control group that received the same dose of the "non-magnetized" drug.

Thus, the effect of drugs on the organism may depend on the characteristics of drugs: physical properties, chemical structure, dose (concentration), as well as on the medicinal form of the drug. The influence of physical factors on the drug can enhance its biological effect in the organism [7].

In our previous work [8], we found a 12–24% increase in the antibacterial effect of benzylpenicillin sodium salt processed by a pulsed magnetic field with the field intensity ranging from 0.09×10^6 A/m to 1.23×10^6 A/m at the frequency f = 40 kHz (single-turn inductor) and a number of pulses n = 1. The pulsed magnetic field action was carried out on a powdered pharmaceutical preparation. Fig. 2 presents the scheme of the PMF action on the drug: inductor 1, pulse current generator 2, PMF sensor 3, and oscilloscope 4. The PMF sensor is connected to the oscilloscope 4. A vial 5 filled with about 4 mm of benzylpenicillin is placed in the middle of inductor 1, after which the pulsed magnetic field treatment is performed.

To determine sensitivity of the bacterium *Escherichia coli* (*E. coli.*) to benzylpenicillin, antibacterial discs were used. The standard disc-diffusion method with sterile dilutions was developed in late 1960s to early 1970s [9] and since then has not undergone any significant changes from a methodological point of view. This method can be used for individual antibacterial therapy to treat the concretive infection in patients, to monitor the spread of antibiotic resistance in a certain area, as well as to study new chemical compounds for the presence of antibacterial activity [10].

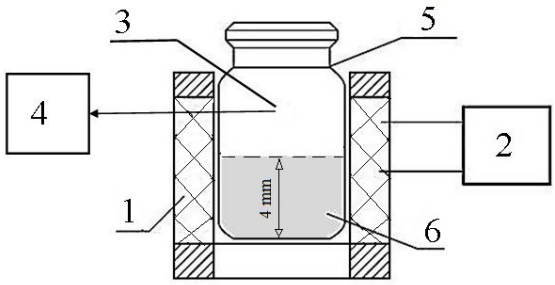


Fig. 2 Scheme of the pulsed magnetic field action on benzylpenicillin.

The study [11] of benzylpenicillin sodium salt in the powdered form (1 g) revealed that after the exposure of benzylpenicillin sodium salt to the pulsed magnetic field, the antibiotic obtained the concentration of 0.01 g/ml. The action of benzylpenicillin was performed on *E. coli* cells with the bacterial culture *E. coli* seeded on the meat-peptone agar. The discs were distributed on the surface of the sown agar by tweezers and then soaked in a solution of benzylpenicillin of 10 µl per disc. The cups were then incubated in a thermostat at 37 °C for 18 h.

The antibacterial activity was evaluated by measuring the average diameter of the lysis zone. The measurement was carried out as follows: the cups were placed upside down on a dark matte surface so that the light fell on them at an angle of 45° (accounting for the reflected light), after which the diameter of growth retardation zones was measured using calipers (the measurement error is ±0.1 mm). The results obtained during the experiment were checked for reliability using the Student's criterion (the level of statistical significance <0.05). The diameter of each lysis zone was measured at least 10 times, after which the average diameter was calculated. To increase the reliability of the results, independent series of repeated experiments were conducted.

The increase in antibacterial activity of benzylpenicillin sodium salt after PMF processing discovered in of this study can be explained by the transition of the PMF-processed molecule to an excited state when its conformation changes slightly. It was also found that the biological effect of the PMF action on drugs decreases with time, being maximally manifested within the day. PMF treatment of benzylpenicillin sodium was not accompanied by an increase in its acute toxicity or emergence of free radicals.

The aim of the work is to study the structural changes in a molecule of benzylpenicillin sodium salt after exposure to a pulsed magnetic field.

2 Experimental Procedure

The study of benzylpenicillin sodium salt was carried out at the PMF parameters (Table 1) with the frequency of f = 40 kHz. The exposure time of the test drug to the PMF was 0.0002–0.005 s [12, 13].

Table 1 Parameters of the PMF action on benzylpenicillin sodium salt.

W (energy), kJ	0.45	2.49	4.11
H (intensity), 10^6 A/m	0.09	0.50	0.82
f (frequency), kHz		40	

Control samples of the drug were not exposed to the PMF. To register the spectra, the powder was thoroughly ground with KBr in an agate mortar at the ratio of 1:100. The test mixture was placed in a cuvette in a special holder, after which the diffuse reflection spectra were recorded.

As is well-known, the most informative regions of the Fourier spectra are the medium-frequency (1000–1970 cm^{-1}) and high-frequency (3200–3800 cm^{-1}) regions. The spectra were recorded using a *FSM-2201* Fourier spectrophotometer (*Infaspec*, Russia) in the wavenumber range from 470 cm^{-1} to 5000 cm^{-1}. The studied spectra were recorded with a spectral resolution *Fspec* software (*Monitoring*, Russia). The limit of the permissible absolute error of the wavenumber scale on the device is ±0.05 cm^{-1}, the error of measuring the absorption intensity is 0.05%.

3 Results and Discussion

Figs. 3 and 4 present spectra of benzylpenicillin as a result of the PMF action for two regions of the spectrum. In the region of N–H valence oscillations, the following bands are observed: 3320 cm^{-1}, 3355 cm^{-1}, 3369 cm^{-1} (Fig. 3).

Table 2 presents the changes recorded in the Fourier spectrum when the antibiotic was exposed to the PMF. The intensities of the bands 3320 cm^{-1} and 3369 cm^{-1} decrease in proportion to the magnetic field intensity. The intensity of the 3355 cm^{-1} band first decreases slightly (by about 3%) and then returns to its original state.

Fig. 4 presents the bands of absorption of the pharmacy antibiotic in the carbonyl region.

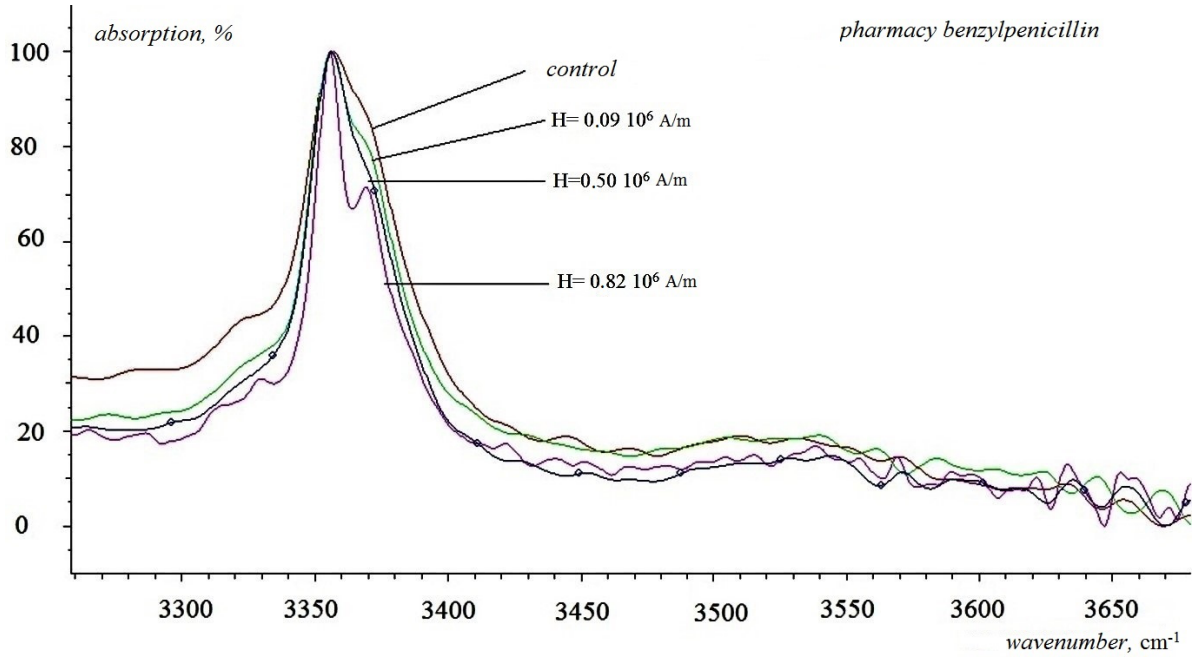


Fig. 3 Fourier spectra of the antibiotic after the PMF processing.

Table 2 Changes in the Fourier spectrum under the PMF action on benzylpenicillin.

Band, cm^{-1}	Control	Processing at intensity H = 0.09 × 10^6 A/m	Processing at intensity H =0.50 × 10^6 A/m	Processing at intensity H = 0.82 × 10^6 A/m
3355	100	96.7	96.7	100
3369	85.6	80.6	73.8	70.4
3320	42.6	33.5	29.6	27

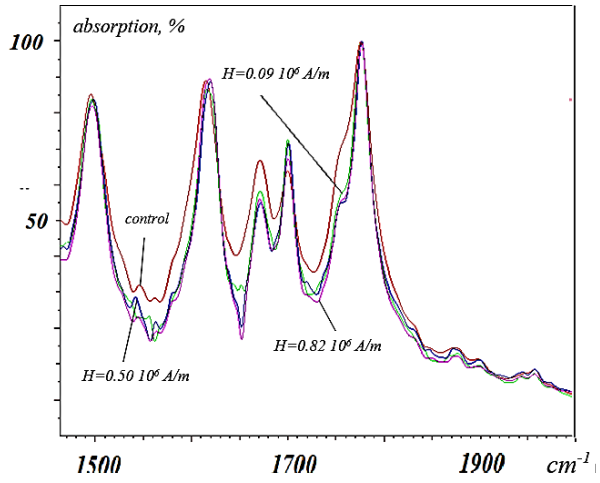


Fig. 4 Absorption bands in the carbonyl region of the Fourier spectrum of pharmacy antibiotic.

The 1700 cm^{-1} region displays the bands that correspond to valence oscillations C = O of the peptide group (1698 cm^{-1}), oscillations C = O of the group attached to the β-lactam ring (the 1773 cm^{-1} band), the 1672 cm^{-1} band belongs to the complex oscillation of the amide group.

The following conclusions can be drawn from the given spectra:

1. Intensity of the 1773 cm^{-1} band does not depend on the PMF processing of the drug.
2. Intensities of the 1672 cm^{-1} and the 1699 cm^{-1} are redistributed depending on the power of the PMF action: the intensity of the high-frequency band increases, and the intensity of the low-frequency band decreases.

In our previous work [14], we found that the enhancement of the biological effect from the PMF action on the antibiotic disappears after about 24 hours. The Fourier spectra were studied for the effect of the repeated exposure to the PMF.

The spectra of the powdered benzylpenicillin in potassium bromide were studied under the following experimental conditions:

– sample 1 was exposed to the PMF once, i.e. the spectra were recorded after 24 hours;

– sample 2 was exposed to the PMF twice with a 24 h interval, i.e. the spectra were recorded after 48 h;

– sample 3 was exposed to the PMF three times with an interval of 24 h, i.e. the spectra were recorded after 72 h.

When processing the powdered antibiotic by the pulsed magnetic field with the intensity $H = 0.09 \times 10^6$ A/m, it was noticed that in the region of N–H valence oscillations, the band intensity in the 3400 cm^{-1} region decreases 24 and 48 h after the PMF action on the same drug compared to the unprocessed drug, and the maxima become more distinct. In this case, the band of 3470 cm^{-1} decreases in intensity more substantially at PMF intensities $H = 0.09 \times 10^6$ A/m and $H = 0.50 \times 10^6$ A/m. Apparently, there is a break in the hydrogen bonds with the water molecules contained in KBr. In the low-frequency region of the spectrum, no changes are observed. At intensity $H = 0.82 \times 10^6$ A/m, a decrease in intensity of bands of 3335 cm^{-1} and 3370 cm^{-1} was observed in the region of oscillations of the carbonyl group [15, 16].

When the drug was re-processed with the PMF on the second day, a change in the intensity of the bands of the Fourier spectra was observed, and when the PMF was applied to the antibiotic twice for a period less than 48 hours, the band intensity also decreased. Thus it can be assumed that the repeated PMF treatment of the same drug has an effect on the intensity of oscillations. For example, when comparing the 3335 cm^{-1} band without the PMF action to a two-time exposure, the intensity decreases by about 13%. It is assumed that after the high-intensity PMF action, the charge accumulates in the drug, and after the elimination of the magnetic field, the effect gradually disappears since, as mentioned above, the time of retention of the PMF effect is about 24 h.

According to the results obtained, the changes in the spectra of benzylpenicillin sodium salt suggest that the hydrogen bonds play a decisive role in the change in biological activity. The recorded changes in the functional groupings of the antibiotic may be due to the fact that when the drug molecule is placed in the pulsed magnetic field, the orientation of the molecule changes relative to the direction of the applied PMF.

It is well-known that penicillins cause the death of microorganisms by blocking the inclusion of acetylmuram peptides in the growing cell walls of bacteria acting mainly on the enzyme D–D–transpeptidase, which cleaves the terminal D–alanine from N–phcetilmuramylpentapeptide and catalyzes the formation of cross-links. Therefore, the antibacterial activity of β–lactam antibiotics is primarily associated with the suppression of the activity of transpeptidase. D–alanyl–D–alanine plays the role of an identification mark for the enzyme. Another factor is acylation of transpeptidase by peptidoglycan, accompanied by the loss of one D–alanine molecule:

Enzyme + R–D–Ala–D–Ala → R–D–Ala–enzyme + D–Ala

Then transpeptidase is regenerated binding the terminal residue of D–alanine of the peptidoglycan molecule to a chain of four glycine molecules (connected to the lysine residue), the second molecule of peptidoglycan. Penicillins having groupings similar to D–alanyl–D–Alanine in the region of the β–lactam ring (Fig. 5) irreversibly inhibit transpeptidase, which causes the death of *E. coli.* cells.

Therefore, changes in the valence angles of the amide grouping near the β–lactam ring after exposure to the pulsed magnetic field can cause minor changes in the structural conformation of the benzylpenicillin molecule and contribute to an increase in the affinity to the active centre of the enzyme, thereby increasing the antibacterial activity of the drug.

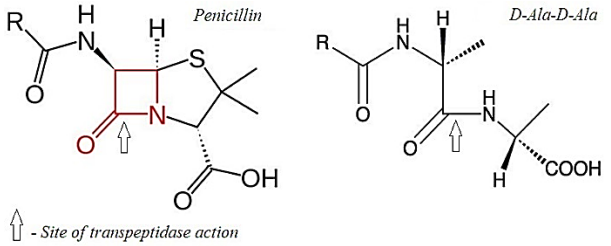


Fig. 5 Comparison of the molecular structure of penicillin and D–alanyl–D–alanine.

4 Conclusion

An increase in power of the magnetic field action on benzylpenicillin sodium salt leads to a decrease in the intensity of the 3320 cm^{-1} and the 3369 cm^{-1} bands. Changes in the amide group were recorded depending on the application of the PMF to the antibiotic. Perhaps, the changes are produced by the geometry of the molecule.

Changes in the structural conformation of the benzylpenicillin sodium salt molecule, processed by the pulsed magnetic field, could contribute to an increase in the affinity to the active centre of the enzyme of transpeptidase, thereby possibly increasing the antibacterial activity of the drug. The observed changes in the spectra of benzylpenicillin sodium salt after PMF processing are small, so further studies are required to study the PMF action on the structure of the antibiotic and its antibacterial activity.

Disclosures

All authors declare that there is no conflict of interests in this paper.

Acknowledgements

This research was supported by the UMNIK program of the Innovation Promotion Fund.

References

1. B. Olivares, F. Martínez, L. Rivas, C. Calderón, J. M. Munita, and P. R. Campodonico, "A natural deep eutectic solvent formulated to stabilize β-lactam antibiotics," Scientific Reports 8(1), 14900 (2018).
2. A. I. Varakin, Y. V. Seryanov, and N. V. Arkhipova, "Quantum-chemical modeling of antibiotic molecules and anions and the nature of their transport in biological membranes," Bashkir Chemical Journal 16(3), 116–121 (2009) [in Russian].
3. T. A. Krysanova, D. L. Kotova, and E.G. Davydova, "Interactions in the system water-solid samples of sodium salt of benzylpenicillin," Bulletin of Voronezh State University. Series: Chemistry, Biology, Pharmacy 2, 37–41 (2012) [in Russian].
4. J. Potticary, L. R. Terry, C. Bell, A. N. Papanikolopoulos, P. C. M. Christianen, H. Engelkamp, A. M. Collins, C. Fontanesi, G. Kociok-Köhn, S. Crampin, E. D. Como, and S. R. Hall, "An unforeseen polymorph of coronene by the application of magnetic fields during crystal growth," Nature Communications 7(1), 11555 (2016).
5. J. G. Brandenburg, J. Potticary, H. A. Sparkes, S. L. Price, and S. R. Hall, "Thermal Expansion of Carbamazepine: Systematic Crystallographic Measurements Challenge Quantum Chemical Calculations," The Journal of Physical Chemistry Letters 8 (17), 4319–4324 (2017).
6. V. Shaporov, "The effect of magnetic field on the action of medicinal substances," Medchitalka (accessed 17 March 2021). [https://www.medchitalka.ru/medicina_segodnya/medicinskaya_orbita/3398.html] [in Russian].
7. N. L. Shimanovsky, M. A. Epinetov, and M. Y. Melnikov, Molecular and Nanopharmacology, Fizmatlit, Moscow, (2009) [in Russian]. ISBN 978-5-9221-1208-6.
8. V.A. Glushchenkov, T. I. Vasilyeva, P. P. Purigin, I. A. Belyaeva, N. A. Rodenko, A. K. Madyarova, and R. Ju. Jusupov, "Changes in the Antibacterial Activity of Benzylpenicillin Exposed to a Pulsed High-Intensity Magnetic Field," Biophysics 64 (2), 214–223 (2019).
9. L. T. Musina, Physiology of bacteria: Instructional guidelines for teachers and students of medical universities, KSMU, Kazan, Russia (2001) [in Russian].
10. A. S. Labinskaya, Guide to Medical Microbiology. Private medical microbiology and etiological diagnosis of infections: Manual for postgraduate professional education of Physicians, Binom, Moscow (2010) [in Russian].
11. N. A. Klenova, Laboratory Workshop on Microbiology, Samara University, Samara (2012) [in Russian].
12. V. A. Glushchenkov, V. F. Karpukhin, Magnetic-Impulse Materials Processing Technlogy, Fedorov, Samara, Russia (2014) [in Russian].
13. R. Yu. Yusupov, V.A. Glushchenkov, Power Units for Magnetic-Impulse Materials Processing, Fedorov, Samara, Russia (2013) [in Russian].
14. N. A. Rodenko, T. I. Vasilieva, I. A. Belyaeva, V. A. Gluschenkov, P. P. Purygin, A. V. Samorodov, and L. I. Bashirova, "Research on the safety of benzylpenicillin sodium salt after exposure to a pulsed magnetic field," Butlerov Communications 58(6), 123-129 (2019).
15. Ch. N. Rao, Electronic Spectra in Chemistry, Mir, Moscow, Russia (1964) [in Russian].
16. O. V. Sverdlova, Electronic Spectra in Organic Chemistry, Chemistry, Leningrad, Russia (1973) [in Russian].

Research into Silicon Nanoparticles as Agents for UHF Hyperthermia *In Vitro*

Angelina V. Kosheleva* and Egor A. Bobkov
National Research Nuclear University «Moscow Engineering Physics Institute», 31 Kashirskoe shosse, Moscow, Russian Federation

*** e-mail:** anjelickos-2013@yandex.ru

Abstract. The current approaches to cancer treatment, including surgery and high-energy beam irradiation, do not always give satisfactory results for a number of oncological neoplasms. One of the promising areas in oncology is the use of nanoparticles selectively heated by external action as agents for hyperthermia of some types of tumors. In this work, we performed selective heating of suspensions of silicon nanoparticles using a device for electromagnetic high-frequency therapy (UHF-60). © 2021 Journal of Biomedical Photonics & Engineering.

Keywords: microporous silicon nanoparticles; cancer therapy; high-frequency hyperthermia.

Paper #3385 received 25 Nov 2020; revised manuscript received 2 Mar 2021; accepted for publication 23 Mar 2021; published online 31 Mar 2021. doi: 10.18287/JBPE21.07.010306.

1 Introduction

In the modern world, the problem of an increase in the number of patients with various types of oncological diseases is quite acute. According to statistics, physicians register about 10 million new cases of the disease annually in the world. Current approaches to cancer treatment, including surgery, high-energy beam irradiation and chemotherapy, do not always give satisfactory results for a number of cancers. That is why the search for new directions and methods of cancer therapy is now a trending topic. One of the promising areas in oncology is the use of nanoparticles as a means of both diagnostics and cancer therapy [1].

It is assumed that with the help of nanoparticles (NPs), the problems of early diagnosis of malignant neoplasms, determination of their localization, targeted delivery of drugs into the tumor can be solved, and new methods of therapy can also be developed [2]. It has been shown that some types of inorganic particles are able to selectively accumulate in tumor tissues due to the enhanced permeation and retention effect (EPR) [3] associated with the particle size. At the same time, NPs for biomedical applications should be non-toxic, biocompatible, and naturally excreted from the body [4].

Hyperthermia is one of the methods of treating oncological diseases. The essence of this method is to heat the human body to a temperature over 41 °C. At this temperature, cancer cell can die [5]. However, the selectivity of this method needs to be increased to minimize the accompanying damage to healthy tissues. Therefore, despite its apparent simplicity, this method is fraught with a lot of risks and complexity in execution. When using hyperthermia, the method of local hyperthermia brings the least harm to the body. This is heating only a narrowly localized area affected by cancer cells. Since tissue heating is supposed to be carried out by means of high-frequency or laser radiation, it is necessary to use such NPs, which, in addition to their low toxicity, will be heated under the influence of these types of electromagnetic radiation. In this work, we used silicon (Si) based NPs. The properties of this type of NP have been studied by many scientists and researchers for quite a long time [6]. The article by L. Osminkina and V. Timoshenko “Porous Silicon as a Sensitizer for Biomedical Applications” implies that silicon particles can be used as sensitizers for UHF hyperthermia [7].

It is assumed that microporous silicon NPs (μPsi) accumulated in cancer cells will heat up more than healthy tissues of the body. Thus, the plan is to carry out the destruction of cancer cells without affecting the adjacent healthy ones. This method will make the therapy of cancer safe and effective. Therefore, the aim of this work is to study the rate and maximum temperature of heating of aqueous suspensions of NPs μPsi under RF excitation.

High-frequency radiation has a large penetration depth, which makes it possible to treat deeply located tumors. Physical experiments show that heating of aqueous suspensions of PSi NPs by tens of centigrade can

be achieved by irradiation at a frequency of 27 MHz and a relatively low intensity (1–5 W/cm^2) [8].

Thus, it is possible to reach the solution temperature above 41 °C. The purpose of the experiments is to select the most convenient heating method, as well as to select the correct concentration of nanoparticles. The higher the concentration of PSi NPs, the stronger the heating of its solution. However, silicon still has a slight toxicity, and therefore it is necessary to select the most effective and least harmful concentration of the PSi NP solution for the body.

2 Synthesis and Characterization of Porous Silicon Nanoparticles

Porous silicon (PSi) is a non-toxic, biocompatible and biodegradable material (Fig. 1). It is able to activate (sensitize) biochemical reactions and physical processes of energy dissipation when excited (irritated) by light and high-frequency radiation [7].

Microporous silicon (micro-PSi) samples were formed by the standard method of electrochemical etching [9] of bulk cSi wafers (p-type, doped with boron to a resistivity of 1–10 Ohm-cm, (100)-oriented) in a mixture of hydrofluoric acid (48%) and ethanol (1:1).

The etching time was 40 min with the current density of 60 mA/cm^2. Free standing PSi films were obtained by removing from the substrate after applying a short pulse of etching current of 500 mA/cm^2. In previous studies, PS films were dried in air for 1 week. Mesoporous silicon (meso-PSi) samples were obtained from p-type c-Si wafers heavily doped with boron (the resistivity is 1–5 Ohm-cm, the orientation is (100)) using the same electrochemical etching procedure.

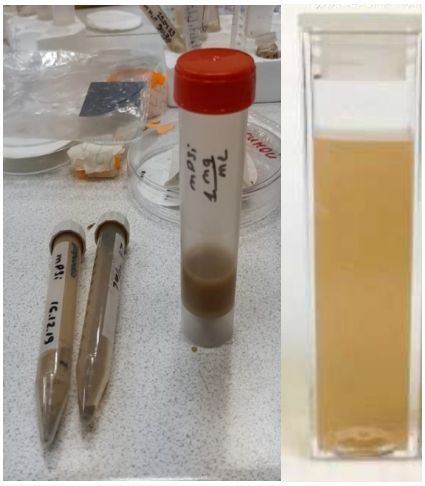


Fig. 1 Microporous silicon nanoparticles.

To study the stability of Si nanoparticles in water, the respective powders were suspended in water. 200 mg of meso-PSi and micro-PSi powders were ground in 2 ml of water for 2 min in a planetary mill (PULVERISETTE 7, “FRITSCH”, Germany), ZrO_2 balls 5 mm, 2 min, 900 rpm) or in an aqueous solution of dextran (30–40 kDa), 10 wt%). The suspensions were dried on cover slips immediately after grinding, 48 and 120 h after grinding.

The phase purity of the compounds was checked by powder X-ray diffraction (XRD) recorded on a RADIAN-DR2 (ZAO “STC Expert Center”, Moscow) diffractometer (CuKa1 radiation, image resolution is 0.05 for panoramic scanning, 0.01 for scanning the peak shape, the exposure time is 1 s for panoramic scanning, 20 s for scanning the peak shape).

Fig. 2 shows a µPsi image obtained using a LEO912 AB OMEGA transmission electron microscope located at Moscow State University [10].

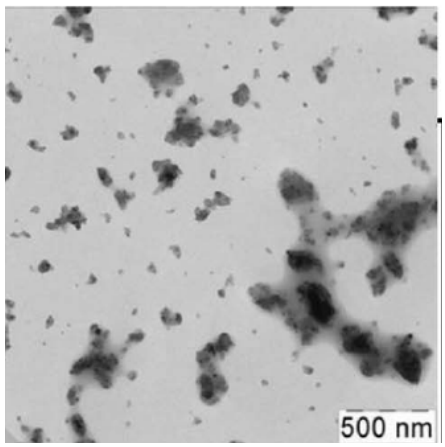


Fig. 2 µPsi Nanoparticles under LEO912 AB OMEGA (“Carl Zeiss”, Germany) transmission electron microscope.

3 Study into Heating Colloids under UHF Excitation

HF heating in each experiment was carried out by means of the UHF-60-MedTeKo (“MedTeKo LLC”, Russia) UHF-therapy apparatus operating at a frequency of 27.12 ± 0.16 MHz with a maximum power of 60 W. The temperature was controlled by means of a Flir C3 (“Flir”, USA) thermal imager. The heating power was 60 W with the thermal imager measured temperature in the range from –10 °C to +150 °C. The measurement error was 1 degree or 1% depending on the value.

To measure heating, three 4.5 ml polystyrene cuvettes were filled with aqueous solutions with nanoparticle concentrations of 3 g/l, 6 g/l, and distilled water in the third cuvette. The volume of each solution was 1.5 ml. Once the solutions had been prepared, the flask was positioned in the center between the RF electrodes, spaced 42 mm apart, providing an air gap of approximately 6 mm on both sides of the cuvette (Fig. 3).

200 µl of the solution of silicon nanoparticles with the concentration of 15 mg/ml was prepared for subsequent introduction into beef liver. The liver was placed between the electrodes of the UHF-therapy apparatus on a plastic Petri dish.

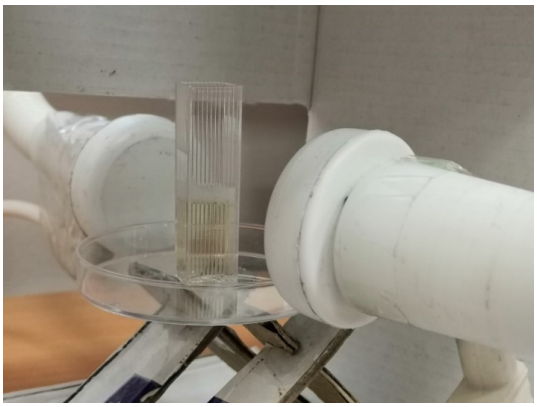


Fig. 3 Installation of a cuvette between the electrodes of the UHF-therapy apparatus.

4.1 Determination of heating value of microporous silicon aqueous suspension when exposed to HF radiation (27 MHz)

In this experiment we used solutions of microporous silicon (μPSi) with a concentration of 6 g/l and 3 g/l, as well as distilled water. Each sample was heated for 5 min. The purpose of the experiment was to establish the relationship between the sample temperature growth rate and the time for several concentrations of microporous silicon particles. This is enough to take solutions with the concentration of low-frequency PE, which will differ by a factor of two, for the clarity of the experiment. These figures are not related to the effective dose for the human body. The initial conditions were at room temperature of 19 °C. Fig. 4 shows the results of the experiment.

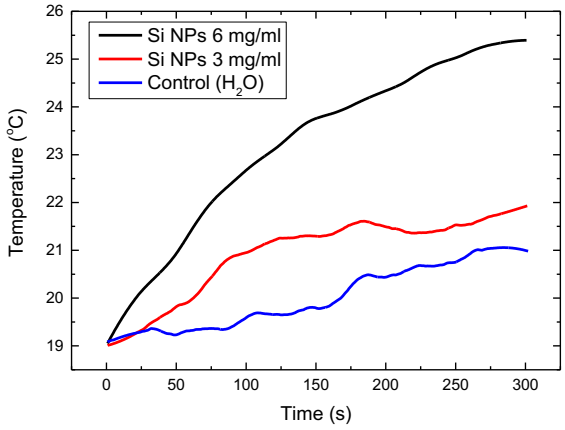


Fig. 4 Temperature relationship between the aqueous suspensions of microporous silicon with concentration of 6 g/l, 3 g/l and distilled water and the time of 27 MHz HF irradiation.

Conclusion: the final heating temperature grows with the μPSi particle concentration. Heating aqueous suspension of porous silicon nanoparticles of 3 g/l concentration for 5 min leads to a 4 °C growth of the initial temperature, and to 7 °C growth at concentration of 6 g/l. The HF field radiation was used at 27 MHz and 60 W power.

4.2 Determination of the heating value of microporous silicon injected into beef liver under the influence of HF radiation (27 MHz)

The previous experiment has shown that as the concentration of microporous silicon increases, the temperature reached after 5 min of heating also increases. Now it is necessary to conduct an experiment with the concentration of micropore silicon HA, which will be effective in cancer therapy and yet low-toxic. This concentration was already calculated in Ref. [11] for the experiment with laboratory mice. The authors evaluated the physical parameters of mice, such as lethargy, weight loss, mortality, etc., when administering concentrations of HF solution from 150 mg/ml to 500 mg/ml. As a result, only when a concentration of 150 mg/ml was administered, no side effects were seen, which allows us to assume that this concentration is the maximum possible concentration. However, in order to further reduce the risk of intoxication and to understand which concentration would allow sufficient heating to be achieved, we chose a concentration 10 times lower, 15 mg/ml, for the experiment. It goes without saying that at higher concentrations, even greater heating will be achieved, as was established in the previous experiment.

Therefore, in this experiment, 15 grams of fresh beef liver were placed on a 6 mm plastic Petri dish. Two injection solutions were prepared for comparison. The first one was a 200 μl aqueous solution of silicon nanoparticles with a concentration of 15 mg/ml. The second was a 200 μl solution of distilled water. The 5 min heating was carried out by the UHF-60-MedTeKo UHF-therapy apparatus with the power of 60 W. The results of the experiment are presented in Figs. 5 and 6.

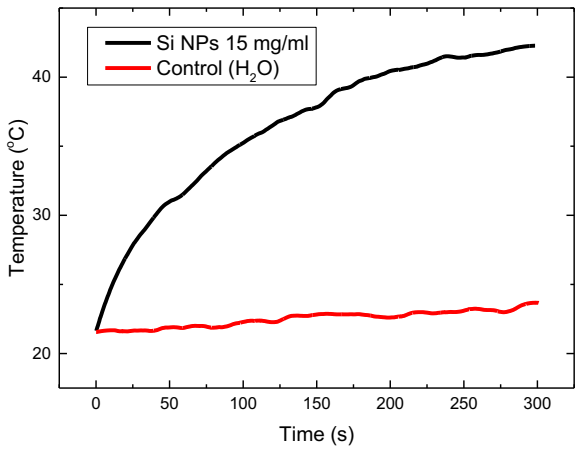


Fig. 5 Determination of the heating value under the influence of HF radiation (27 MHz) of microporous silicon injected into beef liver. The graph of the temperature relationship between beef liver injected with nanoparticles of microporous silicon with a concentration of 15 mg/ml and distilled water and the time of exposure to 27 MHz RF radiation.

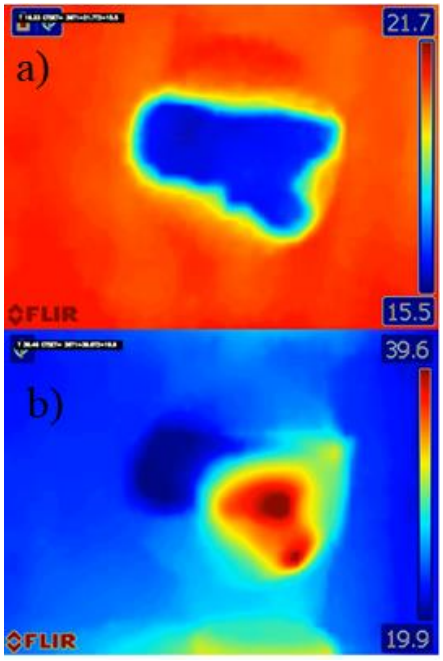


Fig. 6 Determination of the heating value under the influence of HF radiation (27 MHz) of microporous silicon injected into beef liver. Images are taken from the thermal imaging camera. (a) Image of beef liver (blue area) before heating, its average temperature is about 20 °C. (b) Image of the beef liver during the heating with the UHF machine for 4 min. The temperature has already reached 39.6 °C.

The figures show that at the injection site of microporous silicon nanoparticles, the temperature is much higher than in other areas and the difference is about 20 °C. This allows us to say that heating occurs only in the locations where microporous silicon nanoparticles are injected, while the adjacent zones are not affected. That is the main task of local hyperthermia: to heat only a narrow area of the affected tissues, without affecting the surrounding healthy ones.

Conclusion: as a result of experiments with silicon nanoparticles for 5 minutes of heating by the UHF-60-MedTeKo device with a power of 60 W, the temperature of 42 °C was reached, which is necessary for hyperthermia (the lower hyperthermia threshold of is 41 °C). At the same time, in the areas where the nanoparticles were not injected, the temperature was below 40 °C (which is the boundary temperature for healthy tissues, above which irreversible changes can occur).

4 Conclusion

In this work, the study of silicon nanoparticles as agents for UHF hyperthermia *in vitro* was carried out. On the basis of the experiments a number of conclusions were made:

1) Heating an aqueous suspension of porous silicon nanoparticles for 5 minutes with concentrations of 3 g/L was 4 °C from the initial temperature and with concentrations of 6 g/L was 7 °C in the 27 MHz and 60 W RF field. As can be seen from the *in vitro* experiment, a µPsi nanoparticle solution with a concentration of 6 g/l heated an average of 4 degrees more than the distilled water.

2) It was demonstrated that silicon particles could be used as sensitizers for local high-frequency hyperthermia. In an experiment with beef liver, the hyperthermia temperature of 42 °C was achieved in the accumulation zone of microporous silicon nanoparticles, while the adjacent around reached only a safe 20–25 °C temperature.

The experiments conducted show a great potential this research for cancer therapy. The next step in this direction will be to find the optimal concentration of nanoparticles, which will increase the effectiveness of therapy and yet reduce the toxicity. The second direction will be constructing a device for thermographic heating control during high-frequency hyperthermia. This device could bring the method of hyperthermia to a new level, allowing for high-quality and safe procedures *in vivo*.

Disclosures

All authors declare that there is no conflict of interests in this paper.

Acknowledgements

This research was supported by the UMNIK program of the Innovation Promotion Fund.

References

1. Y. V. Kargina, A. M. Perepukhov, A. Yu. Kharin, E. A. Zvereva, A. V. Koshelev, S. V. Zinovyev, A. V. Maximychev, A. F. Alykova, N. V. Sharonova, V. P. Zubov, M. V. Gulyaev, Y. A. Pirogov, A. N. Vasiliev, A. A. Ischenko, and V. Yu. Timoshenko, "Silicon Nanoparticles Prepared by Plasma-Assisted Ablative Synthesis: Physical Properties and Potential Biomedical Applications," Physica Status Solidi (A) 216(14), 1800897 (2019).
2. Y. Zhang, M. Li, X. Gao, Y. Chen, and T. Liu, "Nanotechnology in cancer diagnosis: progress, challenges and opportunities," Journal of Hematology & Oncology 12(1), 137 (2019).
3. K. Greish, "Enhanced Permeability and Retention (EPR) Effect for Anticancer Nanomedicine Drug Targeting," in Cancer Nanotechnology. Methods in Molecular Biology (Methods and Protocols), S. Grobnyer, B. Moudgil (Eds.), Humana Press, New Jersey, USA, 25–37 (2010).

4. D. I. Bilenko, O. Y. Belobrovaya, V. V. Galushka, E. A. Zharkova, D. O. Kochnev, I. B. Mysenko, V. P. Polyanskaya, and D. V. Terin, "Porous silicon with AGI nanoparticles is a promising material for biomedical applications," Methods of computer diagnostics in biology and medicine, 201–203 (2015) [in Russian].
5. Hyperthermia (accessed 13 November 2020). [https://nmicr.ru/meditsina/vysokotekhnologichnaya-meditsinskaya-pomoshch/gipertermiya/].
6. L. A. Osminkina, V. Yu. Timoshenko, "Porous Silicon as a Sensitizer for Biomedical Applications," Mesoporous Biomaterials 3, 39–48 (2016).
7. K. P. Tamarov, L. A. Osminkina, S. V. Zinovyev, K. A. Maximova, J. V. Kargina, M. B. Gongalsky, Y. Ryabchikov, A. Al-Kattan, A. P. Sviridov, M. Sentis, A. V. Ivanov, V. N. Nikiforov, A. V. Kabashin, and V. Y. Timoshenko, "Radio frequency radiation-induced hyperthermia using Si nanoparticle-based sensitizers for mild cancer therapy," Scientific reports 4, 7034 (2014).
8. L. T. Canham, "Silicon quantum wire array fabrication by electrochemical and chemical dissolution of wafers," Applied Physics Letters 57(10), 1046–1048 (1990).
9. Transmission electron microscope LEO 912 ab omega (accessed 18 December 2020). [https://istina.msu.ru/equipment/card/29156772].
10. L. Sancey, S. Kotb, C. Truillet, F. Appaix, A. Marais, E. Thomas, B. van der Sanden, J.-P. Klein, B. Laurent, M. Cottier, R. Antoine, P. Dugourd, G. Panczer, F. Lux, P. Perriat, V. Motto-Ros, and O. Tillement, "Long-Term exvo Clearance of Gadolinium-Based AGuIX Nanoparticles and Their Biocompatibility after Systemic Injection," ACS Nano 9(3), 2477–2488 (2015).